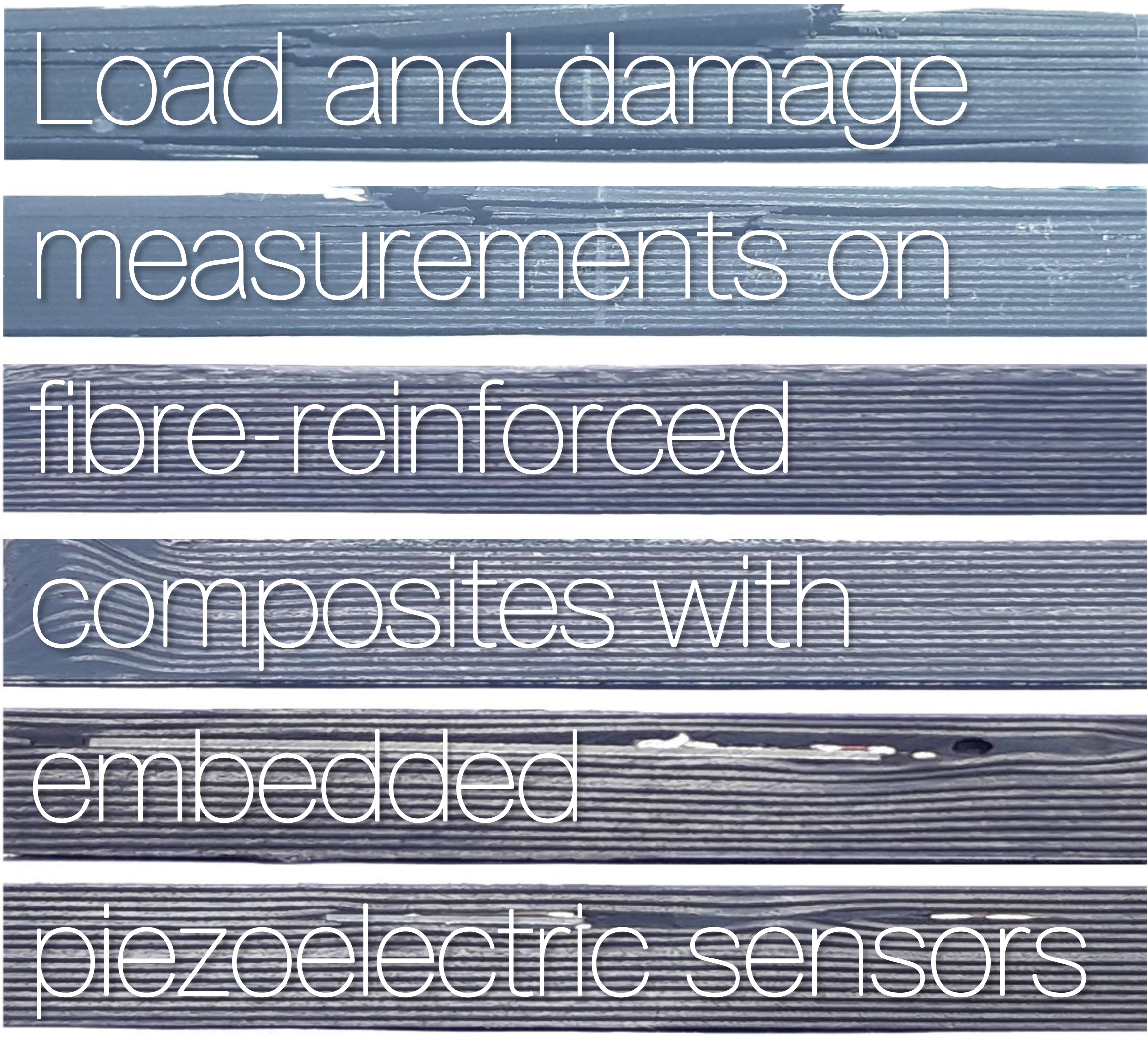

# Load and damage measurements on fibre-reinforced composites with embedded piezoelectric sensors

## A feasibility study

A. J. Huijer

# Load and damage measurements on fibre-reinforced composites with embedded piezoelectric sensors

## A feasibility study

by

A. J. Huijer

to obtain the degree of Master of Science
at the Delft University of Technology,
to be defended publicly on Monday November 11, 2019 at 10:30 AM.

| | | |
|---|---|---|
| Student number: | 4268725 | |
| Project duration: | December 1, 2018 – November 11, 2019 | |
| Thesis committee: | Prof. Dr. Ir. M. L. Kaminski, | TU Delft, chair |
| | Dr. MSc. L. Pahlavan, | TU Delft, supervisor |
| | Prof. Dr. MSc. C. Kassapoglou, | TU Delft, supervisor |
| | Prof. Ir. J. J. Hopman, | TU Delft |
| | Dr. MSc. C. L. Walters, | TU Delft |
| | Ir. B. Scheeren, | TU Delft |
| | Ir. A. Vaders, | Defensie Materieel Organisatie |

An electronic version of this thesis is available at `http://repository.tudelft.nl/`.

# Abstract

Fibre-reinforced composites are increasingly being used in maritime structures. Piezoelectric sensors can be used to monitor both loads acting on a fibre-reinforced composite structure and elastic waves emitted from damage initiation within the structure. In certain marine applications, due to a harsh environment or for hydrodynamic reasons, piezoelectric sensors cannot be placed on the surfaces of the structure. Fortunately fibre-reinforced composite materials allow piezoelectric sensors to be embedded inside the structure.

The focus in this research is on embedded piezoelectric sensor design, performance and behaviour. Carbon fibre beam specimens with embedded piezoelectric sensors have been manufactured and subject to low-frequency bending, high-frequency elastic wave emission, electrical excitation and monotonic bending to failure.

The low-frequency bending test has given insight in the effects of sensor discharge, that is, decreasing and distorting the sensor response. Also it has been used to check consistency between different specimens. The effect of electrical discharge is practically absent around 1.8Hz but becomes apparent at lower frequencies. The test was simulated numerically. The simulation captures the effects of electrical discharge but underestimated sensor response amplitude by 40% to 65% for the small and large sensor respectively.

High-frequency elastic wave emissions, originating from fibre-reinforced composite failure during monotonic bending, have been measured by an embedded piezoelectric sensor. The signals measured by the embedded piezoelectric sensor have a median signal-to-noise-ratio of 17dB. Using the spectral element method, a parameter study has been performed for a similar, two-dimensional setup. Embedded piezoelectric sensor length and embedment location in the plate thickness has been varied. Both a symmetric and antisymmetric elastic wave have been excited. It has been found that increasing sensor size has a negative effect on the sensitivity of the sensor. The antisymmetric elastic wave is better captured by the sensor response than the symmetric elastic wave. Effects of electromechanical resonance were not noticeable.

Monotonic four-point bending failure tests were performed to compare structural integrity of a carbon fibre-reinforced beam specimen with an embedded piezoelectric sensor to a specimen without sensor. With embedded specimens, an average stiffness drop from 3 to 8% is noted. Specimens with small sensors on the tension side of the composite had a decrease lower than 4% in ultimate strain and at maximum 8% reduction in ultimate load and failure toughness. For specimens with embedded sensors on the compression side, the decline was larger, with the larger sensor outperforming the smaller sensor.

# Preface

Dear reader,

This thesis is the product of a 11-month long adventure of diving into the mysterious fields of piezoelectricity, experiment design and guided waves.

First of all I would like to thank Pooria Pahlavan for introducing me into this topic, as well as for the discussions we had and for his very positive and supportive mindset. Likewise I would like to thank Christos Kassapoglou, especially for his support in the design of the experiments.

I would like to aknowledge Bart Scheeren for his critical way of thinking during the discussions we have had regarding the topics involved in this thesis as well as for sharing his experience in understanding the AMSY-6 data aqcuisition system and related post-processing.

Also I am indebted to Xiaobo Zhang, who helped me during specimen manufacture and created a finite element model of the specimen with embedded sensor.

Furthermore Mirek Kaminski, Hans Hopman, Carey Walters and Andre Vaders deserve a spot on this page for their effort of being part in the thesis committee.

The help from the employees and PhD's from the towing tank, measurement shop, DEMO, EWI, ImPhys and of course DASML was indispensable. Therefore, I would like to thank them as well.

Lastly, I would like to thank my parents, my sister and my friends for their encouragement, friendship and helping me out when needed.

*A. J. Huijer*
*Delft, October 2019*

# Contents

**Abstract** iii

**Preface** v

**List of Figures** ix

**List of Tables** xiii

**1 Introduction** 1
- 1.1 Background 1
  - 1.1.1 Embedment design and host material structural integrity 1
  - 1.1.2 Modelling sensor behaviour 3
  - 1.1.3 Structural health monitoring 3
- 1.2 Research question 3
- 1.3 Research subquestions 4
  - 1.3.1 Theoretical working principle 4
  - 1.3.2 Sensor design and performance 4
  - 1.3.3 Host material mechanical properties 4
  - 1.3.4 Comparison between experimental results and modelling 5
- 1.4 Report structure 5

**2 Theory and modelling** 7
- 2.1 Introduction 7
- 2.2 The piezoelectric effect 7
  - 2.2.1 Piezoelectric material 7
  - 2.2.2 Constitutive equations 7
- 2.3 Piezoelectric piezoelectric sensor response 9
  - 2.3.1 Low frequency piezoelectric sensor response 9
  - 2.3.2 Verification of $C$ region 11
  - 2.3.3 Low frequency limit 11
  - 2.3.4 Electromechanical resonance 11
- 2.4 Elastic waves in a composite beam 13
- 2.5 Conclusions 13

**3 Experiments** 15
- 3.1 Introduction 15
- 3.2 Specimen design 15
  - 3.2.1 Design overview 15
  - 3.2.2 piezoelectric sensor type 15
  - 3.2.3 Wiring 16
  - 3.2.4 Insulation 16
  - 3.2.5 Host material 17
- 3.3 Nondestructive elastic wave emissions 17
- 3.4 Electrical impedance 19
- 3.5 Bending tests setup 20
  - 3.5.1 Low-frequency excitation 21
  - 3.5.2 Specimen flexural properties 22
  - 3.5.3 Specimen failure and elastic wave emissions 22

**4 Experimental results and discussion** 25
- 4.1 Introduction 25
- 4.2 Sensor survival 25

4.3 Electrical impedance . . . . . 26
4.4 Low-frequency excitation. . . . . 26
4.4.1 Conclusion . . . . . 30
4.5 Specimen flexural properties. . . . . 31
4.5.1 Failure mechanisms . . . . . 31
4.5.2 Force-displacement . . . . . 32
4.5.3 Flexural Stiffness . . . . . 33
4.5.4 Ultimate strain . . . . . 34
4.5.5 Maximum corrected load . . . . . 35
4.5.6 Toughness . . . . . 35
4.5.7 Conclusions. . . . . 35
4.6 Specimen failure and elastic waves . . . . . 36
4.6.1 Conclusion . . . . . 39

**5 Simulation 43**
5.1 Introduction . . . . . 43
5.2 Validation of electromechanical transfer function . . . . . 43
5.2.1 Introduction . . . . . 43
5.2.2 Retrieving sensor strain field. . . . . 43
5.2.3 Strain to voltage transfer . . . . . 44
5.2.4 Results . . . . . 44
5.2.5 Conclusions. . . . . 45
5.3 Modelling of guided elastic waves and related sensor response. . . . . 46
5.3.1 Introduction . . . . . 46
5.3.2 Model description. . . . . 46
5.3.3 Mesh convergence . . . . . 47
5.3.4 Parametric study . . . . . 47
5.3.5 Conclusion . . . . . 48

**6 Conclusion 53**
6.1 Theoretical working principle. . . . . 53
6.2 Sensor design and accuracy. . . . . 53
6.3 Host material mechanical properties . . . . . 54
6.4 Comparison between experimental results and modelling . . . . . 54

**7 Recommendations 55**
7.1 Experiment data . . . . . 55
7.2 Modelling . . . . . 55
7.3 Application . . . . . 55

**8 Acknowledgement 57**

**Bibliography 59**

**A Appendix Nondestructive elastic wave emissions 65**

# List of Figures

1.1 Loads and damages in marine structures. (a) Dynamic loads on marine structures can be temperamental. In such a situation, assessment of damage is of key importance. Painting by Théodore Gudin [9]. (b) Strains in lengthwise direction experienced by a glass fibre-reinforced composite marine propeller blade. The figure is a continuation of the work of Maljaars [42]. . . . . . . . . . 2
1.2 Generalised structure of the research performed. . . . . . . . . . 5

2.1 Schematic piezoelectric sensor response. . . . . . . . . . 9
2.2 Simple piezoelectric sensor measurement circuit. . . . . . . . . . 9
2.3 Piezoelectric disc sensor orientation. . . . . . . . . . 10
2.4 Simple piezoelectric sensor measurement for low frequency applications. . . . . . . . . . 11
2.5 A visual explanation of electromechanical resonance. Blue and black colours represent the mechanical and electrical system respectively. . . . . . . . . . 12
2.6 Legendre-Gauss-Lobatto-Lagrange polynomials of order 8. The local coordinate is represented by $x^*$. . . . . . . . . . 14

3.1 Cut-through visualisation of the specimen design showing its different components. . . 16
3.2 Wiring. (a) Small piezoelectric sensor after soldering, prior to glass insulation. (b) SMC connectors, milled to shape. This proved to be a sturdy method for communication with the embedded piezoelectric sensor. . . . . . . . . . 17
3.3 Specimen manufacture. Depicted is the 22th layer, showing the piezoelectric sensors. (a) A full plate containing small piezoelectric sensors. (b) piezoelectric sensor 4S during embedding. Note the glass insulation and the cut-out in the carbon fibre-reinforced plastic lay up. . . . . . . . . . 18
3.4 Through-thickness cuts of specimens 1S and 1L. (a) Small piezoelectric sensor 1S. Fibre waviness is visible near the cut-out region. (b) Large piezoelectric sensor 1L. Also here, fibre waviness is visible. The darker dot close to piezoelectric sensor is either an air pocket or an inclusion that was released after cutting. . . . . . . . . . 18
3.5 Guided wave experimental set-up. Black, white and blue represent composite host material, embedded piezoelectric sensor and locations of pencil breaks. . . . . . . . . . 19
3.6 Performing pencil lead breaks, second phase. (a) gives the general arrangement, with the AEP5H preamplifier in red and the AMSY6 data acquisition system in grey. (b) shows the specimen set up, with the mechanical pencil with Nielsen shoe on the top, commercial R15I-AST sensor in the middle and the SMC connector for the embedded piezoelectric sensor on the bottom of the figure. . . . . . . . . . 19
3.7 Impedance measurements. (a) Virtually freely vibrating sensors. (b) Agilent 4292A network analyzer measuring embedded sensor impedance. . . . . . . . . . 20
3.8 Bending test experimental set-up. The colours black, white and blue relate to the host material, piezoelectric sensor and strain gauge placement. . . . . . . . . . 20
3.9 Low-frequency bending. (a) gives the general arrangement. (b) shows the real-life placement of the specimen. . . . . . . . . . 21

4.1 Electrical impedance absolute value $|Z|$ over excitation frequency. . . . . . . . . . 27
4.2 Electrical impedance phase angle $\theta$ over excitation frequency. . . . . . . . . . 27
4.3 Load cell force $F_{LC}$, strain gauge strain $S_{SG}$ and piezoelectric sensor voltage $U_{PZT}$ of specimen 3L at $v_m = \{10, 1.0, 0.1\}$mm/min for (a), (b), (c), over time $t$. The black strain gauge output corresponds to the top strain gauge. The red strain gauge strain coincides with the bottom strain gauge. . . . . . . . . . 29

4.4 Box plot of $\frac{U_{PZT,a}}{F_{LC,a}}$ for all functional small ('S') and large ('L') sensors. $n$ stands for the number of data points for each sensor, and is slightly different per sensor. . . . . . . . . 31
4.5 Thickness view of specimen 4N. On the top side of the specimen, superficial compressive failure is visible. Tensile rupture can be seen on the bottom of the specimen. The centreline of the specimen is indicated by the light-coloured vertical line. . . . . . . . . . 32
4.6 Thickness view of specimen 2L. On the top side of the specimen, extensive compressive failure is visible. . . . . . . . . . . . . . . . . . . . . . . . . . . . . . . . . . . . . . . 32
4.7 Thickness view of specimen 5S. On the top of the specimen, superficial compressive failure is visible. Tensile rupture can be seen on the bottom of the specimen. . . . . . . 33
4.8 Force-displacement graph of tested specimens. Markers indicate the maximum applied force per specimen. . . . . . . . . . . . . . . . . . . . . . . . . . . . . . . . . . . . . 33
4.9 Signal captured by all three sensors at time $t$= 509s. . . . . . . . . . . . . . . . . . . . 37
4.10 Signal captured by all three sensors at time $t$= 596s. . . . . . . . . . . . . . . . . . . . 37
4.11 Signal captured by all three sensors at time $t$= 622s. . . . . . . . . . . . . . . . . . . . 37
4.12 Signal captured by all three sensors at time $t$= 655s. Note the different scale on the vertical axis. . . . . . . . . . . . . . . . . . . . . . . . . . . . . . . . . . . . . . . . . 37
4.13 Maximum amplitude in dB of a signal captured by both the embedded sensor (3L) and either one of the commercial sensors (R15I-AST). Triangular data represent the signal captured by the embedded sensor, whereas dots refer to the corresponding signal of either one of the commercial sensors. Machine load $F_{LC}$ over time is given for reference. 38
4.14 Maximum amplitude of a signal captured by both of the commercial sensors (R15I-AST). Machine load $F_{LC}$ over time is given for reference. . . . . . . . . . . . . . . . . . . . . . 38
4.15 Hit rate over time for signals that were captured by both the embedded sensor (3L) and one of the commercial sensors (R15I-AST). Machine load $F_{LC}$ over time is given for reference. . . . . . . . . . . . . . . . . . . . . . . . . . . . . . . . . . . . . . . . . 39
4.16 Hit rate over time for signals that were captured by both commercial sensors (R15I-AST). Machine load $F_{LC}$ over time is given for reference. . . . . . . . . . . . . . . . . . . . . . 39
4.17 Signal to noise ratio SNR over time for signals that were captured by both the embedded sensor (3L, triangles) and one of the commercial sensors (R15I-AST, dots). Machine load $F_{LC}$ over time is given for reference. . . . . . . . . . . . . . . . . . . . . . . . . 40
4.18 Signal to noise ratio SNR over time for signals that were captured by both commercial sensors (R15I-AST). Machine load $F_{LC}$ over time is given for reference. . . . . . . . . . 40
4.19 Boxplot of SNR in dB. Measurements are compared between embedded sensor 3L and commercial sensors R15I-AST 1 and R15I-AST 2. . . . . . . . . . . . . . . . . . . . . 41

5.1 Sensor strain distribution $S_{11}$ as determined through finite element modelling during low-frequency bending. (a) and (b) give the result for the small and large sensor respectively. 44
5.2 Response of sensor 11S on excitation with a $v_m$ =10mm/min. The simulated response is given in red. . . . . . . . . . . . . . . . . . . . . . . . . . . . . . . . . . . . . . . . 45
5.3 Response of sensor 11S on excitation with a $v_m$ =0.1mm/min. The simulated response is given in red. . . . . . . . . . . . . . . . . . . . . . . . . . . . . . . . . . . . . . . . 45
5.4 Box plot of measured $\frac{U_{PZT,a}}{F_{LC,a}}$ for small sensors in combination with the simulated results at $R_m$=$10^8\Omega$and $10^{10}\Omega$. . . . . . . . . . . . . . . . . . . . . . . . . . . . . . 45
5.5 Box plot of measured $\frac{U_{PZT,a}}{F_{LC,a}}$ for large sensors in combination with the simulated results at $R_m$=$10^8\Omega$and $10^{10}\Omega$. . . . . . . . . . . . . . . . . . . . . . . . . . . . . . 45
5.6 Discretisation of the composite plate through thickness. Colours indicate different material. Note the figure is not to scale for improved visibility. . . . . . . . . . . . . . . . . . 47
5.7 Convergence study with longitudinal element size $dx$ and shape function order $N_i$ as variables. The cross-correlation values are rounded to the fourth decimal. . . . . . . . . 47
5.8 The response of a symmetric guided elastic wave for sensors with different lengths at different locations in the plate height. . . . . . . . . . . . . . . . . . . . . . . . . . . . 49
5.9 The response of an antisymmetric guided elastic wave for sensors with different lengths at different locations in the plate height. . . . . . . . . . . . . . . . . . . . . . . . . . 50

5.10 Fourier transform of the sensor response based on and overlaid with the Fourier transform of the excited symmetric guided elastic wave. The impedance is given for the a freely vibrating and constrained 1D sensor. . . . . . . . . . . . . . . . . . . . . . . . . . 51
5.11 Fourier transform of the sensor response based on and overlaid with the Fourier transform of the excited antisymmetric guided elastic wave. The impedance is given for the a freely vibrating and constrained 1D sensor. . . . . . . . . . . . . . . . . . . . . . . . . . 52

A.1 Response $U_{PZT}$ of pencil breaks at distance $d$ over time of sensor 3L. $n$ denotes the number of pencil breaks in the plot. The lines have been made semi-transparent, to enhance visibility of overlapping responses. . . . . . . . . . . . . . . . . . . . . . . . . . 66
A.2 B-scan visualisation of $U_{PZT}$ at distance $d$ over time. $n$ denotes the number of pencil breaks in the plot. . . . . . . . . . . . . . . . . . . . . . . . . . . . . . . . . . . . . . . 67

# List of Tables

2.1 Comparison of voltage with Lin and Giurgiutiu [39]. . . . . . . . . . . . . . . . . . . . . . . . 11
2.2 Comparison of voltage with Shin et al. [69]. . . . . . . . . . . . . . . . . . . . . . . . . . . . 12

3.1 Number and types of specimens tested for stiffness and failure. . . . . . . . . . . . . . . . 22

4.1 Functioning sensors per test. a x represents malfunctioning, v properly functioning. . . . 25
4.2 Mean $\mu$ and standard deviation $\sigma$ of corrected flexural stiffness $E_{CH}$ and $E_{SG}$, from the method described in [10] and the strain gauge response respectively. . . . . . . . . . . 34
4.3 Mean $\mu$ and standard deviation $\sigma$ of maximum strain $S_{CH}$ and $S_{SG}$, from the method described in [10] and the strain gauge response respectively. . . . . . . . . . . . . . . . . 34
4.4 Mean $\mu$ and standard deviation $\sigma$ of maximum corrected load $T_{LC}$. . . . . . . . . . . . . 35
4.5 Mean $\mu$ and standard deviation $\sigma$ of $W_{LC}$. . . . . . . . . . . . . . . . . . . . . . . . . . . 36
4.6 Stiffness, ultimate strain, ultimate load and toughness results per specimen. . . . . . . . 36

5.1 Averaged strain in longitudinal direction $S_{11,AV}$, measured in the experiments and calculated through beam theory and FE. . . . . . . . . . . . . . . . . . . . . . . . . . . . . . . 44
5.2 Resistances encountered in the experiments. . . . . . . . . . . . . . . . . . . . . . . . . . . 45
5.3 Material parameters used in the analysis. . . . . . . . . . . . . . . . . . . . . . . . . . . . . 46

# 1

# Introduction

In maritime applications, there is a rising interest in the use of fibre-reinforced composites for structural purposes [27, 42]. Such structures typically are subject to capricious dynamic loads and subsequently, damages can occur. Results of loads and damages in marine structures are given in fig. 1.1. It is of significance to have online insight in the applied loads and any related damage that is generated. Piezoelectric sensors can be used to monitor both dynamic loads acting on a composite structure as well as the structural health. Composites, due to their layered shape, have the ability to accommodate sensors inside the structure. This embedding would allow sensors to be used in areas where the environment is harsh or where hydrodynamics are sensitive and should not be disturbed by surface-mounted sensors.

First a background on the general themes involved in measuring with piezoelectric sensors embedded in composites is given. Based on the background, the primary research question is formed. This is followed by the subdivision of the research question into a variety of research subquestions. Subsequently, the setup of the research is elaborated upon.

## 1.1. Background

Research in embedding piezoelectric sensors and similar objects into fibre-reinforced composites commenced in the 1990's in the field of aerospace structures. Initially the objective of these investigations laid in active vibration control but gradually it spread out, including towards structural health monitoring [38].

### 1.1.1. Embedment design and host material structural integrity

There have been a number of investigations regarding the method of embedding a piezoelectric sensor into a composite material. In general two approaches exist: either by placing the piezoelectric sensor and attachments between host plies [3, 7, 14, 20, 43, 44, 46, 59, 63, 68, 71, 74], or by cutting an aperture that can accommodate the piezoelectric sensor in one or more plies [7, 20, 34, 43]. In a glass-fibre host material, the piezoelectric sensor can be directly embedded. In the case of conductive fibres, such as in carbon fibre-reinforced plastics, electrical insulation between the piezoelectric sensor electrodes and the host material is needed. Typical solutions are by means of a layer of Kapton or polyimide [3, 20, 40, 43, 44, 58, 59], a layer of glass-fibre [3, 20, 67], or through a thermoplastic foil [38]. It is acknowledged by Lin and Chang [40] and Andreades et al. [3] and Liew and Veidt [38] that a polyimide layer insulation requires surface preprocessing to prevent delamination between the host material plies. Lin and Chang [40] stated embedding glass fibre insulation inside a carbon-fibre host results in strength deterioration. The results of Andreades et al. [3] do not confirm this statement.

Prior investigations feature a multitude of methods to obtain tensile, compressive and flexural properties of both graphite fibre and glass fibre composite structures with sensors or similar objects embedded.

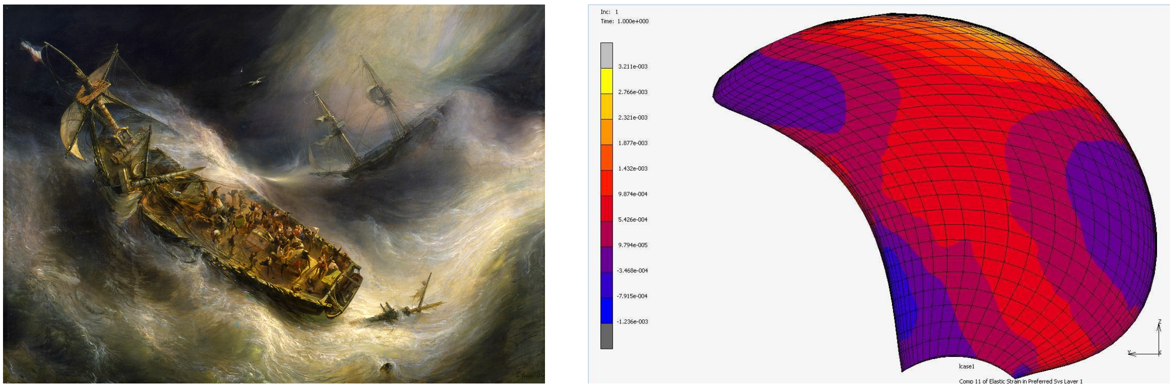

(a) (b)

Figure 1.1: Loads and damages in marine structures. (a) Dynamic loads on marine structures can be temperamental. In such a situation, assessment of damage is of key importance. Painting by Théodore Gudin [9]. (b) Strains in lengthwise direction experienced by a glass fibre-reinforced composite marine propeller blade. The figure is a continuation of the work of Maljaars [42].

Tensile failure tests were executed by Shukla and Vizzini [70], comparing different types of embedding glass plates in a carbon fibre-reinforced plastic composite. It was concluded a cut out with intermitted ply cutting (interlacing) had a beneficial effect on its strength compared to a conventional cut out. The ultimate strength however was notably lower than a specimen without sensor. Both tensile and compressive failure testing of carbon fibre-reinforced plastic specimens with embedded specimens were done by Christophe A. Paget [8]. No degradation due to the sensor was observed. In 2002, Mall [43] experimentally tested carbon fibre-reinforced plastic specimens with embedded sensors under monotonic tension and fatigue and compared stiffness and strength between pristine specimens, specimens with a cut out for the embedded sensors and those without cut out but with embedded sensors. As a result, it was reported there was no difference in stiffness and ultimate strength values were within 5% of each other for monotonic loading. In the case of fatigue, no deterioration due to the sensor was experienced. Shear, compression and out of plane tensional tests were performed by Lin and Chang [40] for graphite fibre-reinforced composites with a SMART layer embedded. From these tests, it is concluded structural integrity is not inherently impeded by the additional layer. Andreades et al. [3] compared carbon fibre-reinforced plastic specimens with either a glass fibre-reinforced plastic insulation or a kapton foil insulation. Structural integrity was assessed by means of shear, compressive and flexural tests. In the results, glass insulated embedded specimens were statistically indistinguishable from pristine specimens. Kapton insulated embedded specimens generally were not. A finite element model was developed by Butler et al. [6] to study the effect of embedded piezoelectric sensors with Kapton insulation on delamination in a carbon fibre-reinforced plastic composite rotor blade part. It was concluded embedding has a limited impact on delamination damage propagation and is dependent on the sensor location with respect to critical locations.

In a woven glass fibre-reinforced plastic composite with embedded sensors placed without cut out, Tang et al. [71] experienced tensional fatigue failure at the electrical leads of the sensor. It was stated the sensors increased local stresses and caused the formation of resin pockets. Chilles et al. [7] performed monotonic four-point bending tests with glass fiber epoxy composite beams. Sensors with induction coil for wireless data acquisition, to counter the effect reported by Tang et al. [71], were embedded with cut-out and without cut-out at different heights in the laminate stack. A finite element model for the beam bending was created. The conclusion was made that embedding such a sensor reduced flexural strength insignificantly. Four point bending was also described in Lampani et al. [34], for glass fibre-reinforced plastic embedded specimens. The sensor was embedded by means of a cut-out. Stiffness and maximum force of the embedded specimen was slightly higher than the reference specimens. Maximum strain was lower. Failure was near the sensor due to a stress concentration, visualised using the finite element method. Masmoudi et al. [47], in three point bending of glass fibre-reinforced plastic specimens, did not find a change in stiffness when embedding sensors. Maximum strain and stress however were lower, with the effect increasing with a larger sensor. The effect of host material (glass fibre-reinforced plastic) strength with different materials for embedded (with cut out) piezoelectric sensors were compared by Konka et al. [31]. Ultimate tensile strength was decreased by 3 to 6% depending on sensor type, and 7 to 15% in interlaminar shear. Yang et al. [74] did a study on strength drop due to embedded sensors and wiring inside a glass fibre-reinforced plastic composite. Ultimate strength drops were 13.8 and 12.3% respectively.

### 1.1.2. Modelling sensor behaviour

Piezoelectric materials provide a linear[1] coupling between the mechanical field to the electrical field and vice versa [26]. Typically of interest is the sensor voltage due to a certain imposed strain field of the structure or the induced strain field of the structure as a function of an imposed sensor voltage. In these cases either one-way coupling, translating a predetermined strain field or voltage to a resulting voltage or deformation, or two-way coupling, which includes reciprocal interaction between the electric and mechanical fields, are used. Depending on external conditions, the former may be calculated analytically or numerically whereas the latter usually involves coupled-field finite element analysis.

One-way coupling was used by Lin and Giurgiutiu [39] and Shin et al. [69] to explain an experimental sensor voltage of a vibrating beam. A method was provided by Erturk and Inman [16] that includes resistance in the electrical system. Gopalakrishnan et al. [22] described a solution for simulating elastic wave measurements with one-way coupling.

A two-way coupling method for piezoelectric sensor layers embedded in a composite was explained by Lam et al. [33] and Reddy [64] by means of the finite element method and classical laminate theory. Similarly, Ha et al. [23] used three-dimensional coupled field elements to simulate composite beam vibration with piezoelectric actuators and sensors attached.

### 1.1.3. Structural health monitoring

The aim of structural health monitoring is to identify and characterize damages in a structure [1]. Piezoelectric sensors can be instrumental in both damage detection and characterisation[2]. As a damage event occurs, such as a delamination, fibre or matrix breakage in fibre-reinforced composites, a distinct elastic wave is emitted throughout the structure [2]. Piezoelectric sensors can measure these emissions directly and by utilising multiple sensors, a localisation of the damage may be performed as demonstrated by Dziendzikowski et al. [14], Yang et al. [74], Zamorano-Senderos and Elvin [76] and Osmont et al. [58].

In the case of Masmoudi et al. [46, 47] a beam specimen with embedded sensors was subjected to a fatigue load. At increasing cycles, elastic wave emissions were recorded, which could later be assigned to different types of failure mechanisms. Andreades et al. [3] succesfully detected elastic waves characteristic for a delamination[3] using embedded piezoelectric sensors. To mimic damage-related elastic emissions, leads from a mechanical pencil can be broken against the host structure, as is done by Masmoudi et al. [46]. Kirkby et al. [29] used pencil lead breaks at varying locations as excitation for damage localisation on a carbon fibre-reinforced plastic plate by means of surface bonded piezoelectric sensors (and fibre bragg gratings).

## 1.2. Research question

From the context above, the following observations are made:

- the effect of embedding a piezoelectric sensor into a fibre-reinforced composite on the structural integrity of that composite is strongly case-dependent;
- a number of models describing general sensor behaviour have been established;

---

[1] That is, at a low electric field intensity [64].

[2] Other methods, such as by using the piezoelectric material as active transducers or by reading out the sensors' electrical impedance, are not discussed here but may be found in the work of Giurgiutiu [21].

[3] Based on the excitation of a transducer.

- embedded piezoelectric sensors have been demonstrated to capture certain vibrations and damage-related elastic waves.

It is of interest to place these separate observations into a single coherent framework, leading to the following research question:

> *Under what conditions is it feasible to measure loads and damage growth in composites using embedded piezoelectric sensors without compromising the structural performance?*

## 1.3. Research subquestions

With regard to the feasibility and the conditions required by the research question, three topics are defined in which related research subquestions are clustered:

### 1.3.1. Theoretical working principle

To accurately reconstruct loads acting on a structure from sensor measurements, understanding in the working principle of the piezoelectric sensor and the behaviour of the host material is essential. Hence the following subquestions are posed:

> *What are the governing physics of piezoelectricity and how can they be modelled in sensor applications?*
>
> *What are elastic waves and how can they be modelled in composites for analysis of elastic wave emissions?*

### 1.3.2. Sensor design and performance

A suitable design of the sensor and its embedding is needed to answer the research question. The performance of an embedded piezoelectric sensor under certain conditions is of interest as well. Related subquestions are formed accordingly:

> *How can a piezoelectric sensor be embedded in a composite structure?*
>
> *To what extent does the embedded piezoelectric sensor design survive the manufacturing process?*
>
> *How does embedding a sensor affect its electromechanical resonant behaviour compared to a non-embedded sensor?*
>
> *What is the variation of responses between measurements and between piezoelectric sensors?*
>
> *To what extent in terms of signal quality and maximum strain is the embedded piezoelectric sensor able to measure damage-related elastic wave emission?*
>
> *Given the measurement set-up, what is the minimum frequency the piezoelectric sensor can measure strain accurately?*
>
> *How does the location and size of the sensor influence elastic wave sensor responses?*

### 1.3.3. Host material mechanical properties

The applicability, and feasibility, of embedding piezoelectric sensors into a fibre-reinforced composite is limited by the sensors' influence on the mechanical properties of the host material. Therefore a related subquestion is presented:

> *To what extent are flexural mechanical properties of the composite host material influenced by embedding a piezoelectric sensor?*

### 1.3.4. Comparison between experimental results and modelling

Accurate modelling is required to translate loads acting on the structure to the voltage captured by the embedded piezoelectric sensors. This statement can be reshaped into the subsequent subquestion:

> *How is the agreement between modelled and measured sensor responses?*

## 1.4. Report structure

The research performed follows the general structure given in fig. 1.2. Theory regarding piezoelectricity and elastic waves is discussed in chapter 2. The design for the specimens and descriptions of the experiments are given in chapter 3. Results with respect to the experiments are presented and discussed in chapter 4. In chapter 5 simulations are performed and compared to experimental results in the case of low-frequency excitations and a parameter study is displayed for elastic wave emissions. On the basis of the results of the above chapters, conclusions are drawn and research subquestions are answered. These are summarised in chapter 6. Recommendations with respect to experiments, modelling and applications are presented in chapter 7. The thesis is ended in chapter 8, containing the acknowledgements.

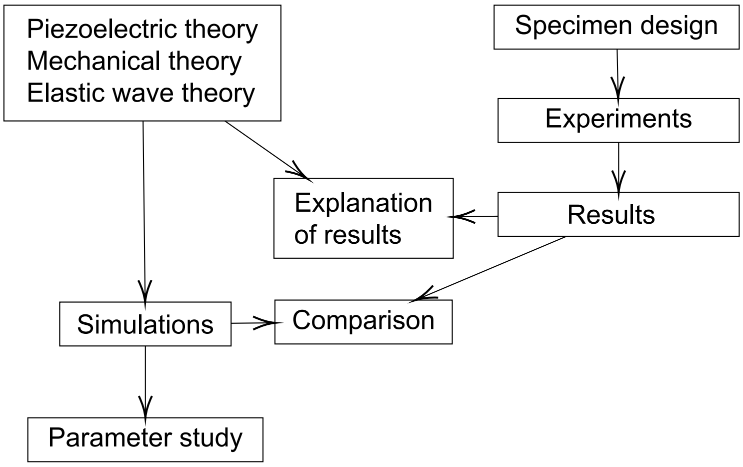
Piezoelectric theory
Mechanical theory
Elastic wave theory
Specimen design
Experiments
Explanation of results
Results
Simulations
Comparison
Parameter study

Figure 1.2: Generalised structure of the research performed.

# 2

# Theory and modelling

## 2.1. Introduction

This chapter is focused on implementing a model for the voltage response of piezoelectric sensors when excited under strain. Also a method is given for modelling guided waves. The chapter aims at evaluating research sub questions:

> *What are the basic physics of piezoelectricity and how can they be modeled in piezoelectric sensor applications?*
>
> *What are guided waves and how can they be modeled in composites for analysis of acoustic emissions?*

First a short background on the piezoelectric effect is given. The background includes a description of piezoelectric materials and the introduction of piezoelectric equations. Second, an analytical model for the strain-voltage response is presented. This model is verified with literature.

Third general phenomena of guided waves are described. This is followed by an explication of the numerical method used to simulate guided wave propagation.

## 2.2. The piezoelectric effect

### 2.2.1. Piezoelectric material

Piezoelectric materials are materials whose microstructure, under mechanical deformation, becomes polarised. The mechanical deformation distorts the crystal structure such that positive nuclei come closer to one side of the crystal and negative electrons come closer to another. In the used piezoelectric sensor material, PZT (lead-zirconite-titanate mixed ceramics), the crystal structure is aligned such that the deformation-induced polarisation results in a macroscopic electric field ([19], [21], [66], [11], [52]).

### 2.2.2. Constitutive equations

The phenomenom decribed above adheres to the principle of conservation of energy. This principle leads to a set of constitutive equations that relate strains and electric displacements $S_{ij}$ to stresses $T_{kl}$, electric field intensity $E_k$ and temperature $\vartheta$. For small variations in above parameters, these constitutive equations are considered linear [66]. A set of linear constitutive equations is given below.

$$S_{ij} = s^{E}_{ijkl} T_{kl} + d_{kij} E_k + \alpha^{E}_{ij} \vartheta \tag{2.1}$$

$$D_j = d_{jkl} T_{kl} + \varepsilon^{T}_{jk} E_k + \rho^{T}_{j} \vartheta \tag{2.2}$$

The terms in eq. (2.1) and eq. (2.2) will be individually addressed by setting other terms to zero (see subscripts).

$$S_{ij,E=0,\vartheta=0} = s^E_{ijkl} T_{kl} \tag{2.3}$$

$$D_{j,T=0,\vartheta=0} = \varepsilon^T_{jk} E_k \tag{2.4}$$

In eq. (2.3), strain tensor $S_{ij}$ is linked to stress tensor $T_{kl}$ by means of elastic compliance $s^E_{ijkl}$ at constant electric field intensity $E$. This is equivalent to Hooke's law for linear elastic material. eq. (2.4) states electric permittivity $\varepsilon^T_{ij}$ at constant stress $T$ translates electric displacement $D_j$, which can be seen as measure of polarization of a material[1], to electric field intensity $E_k$. eq. (2.4) is used as a general constitutive equation in dielectric material.

$$S_{ij,T=0,\vartheta=0} = d_{kij} E_k \tag{2.5}$$

$$D_{j,E=0,\vartheta=0} = d_{jkl} T_{kl} \tag{2.6}$$

eq. (2.5) and eq. (2.6) are characteristic for piezoelectric material. Here, mechanical strain $S_{ij}$ is a function of electric field intensity $E_k$ and electric displacement $D_j$ is a function of mechanical stress $T_{kl}$. $d_{kij}$ and $d_{jkl}$ are the piezoelectric coupling terms.

$$S_{ij,T=0,E=0} = \alpha^E_{ij} \vartheta \tag{2.7}$$

$$D_{j,T=0,E=0} = \rho^T_j \vartheta \tag{2.8}$$

In eq. (2.7), temperature $\vartheta$ leads to strain $S_{ij}$. $\alpha^E_{ij}$ is the linear thermal expansion coefficient. eq. (2.8) describes the pyroelectric effect; temperature $\vartheta$ gives an electric displacement $D_j$ by means of pyroelectric coupling coefficient $\rho^T_j$ at constant strain.

Voigt notation can be used to reduce the tensor ranks. For modeling, this results in a simplified set of constitutive equations, given in eq. (2.9) and eq. (2.10). A version in tensor notation is given in eq. (2.11) and eq. (2.12).

$$S_i = s^E_{ij} T_j + d_{ki} E_k + \alpha^E_{ij} \vartheta \tag{2.9}$$

$$D_l = d_{lj} T_j + \varepsilon^T_{lk} E_k + \rho^T_j \vartheta \tag{2.10}$$

$$\{\mathrm{S}\} = [\mathrm{s}^E]\{\mathrm{T}\} + [\mathrm{d}]\{\mathrm{E}\} + [\alpha^{\mathrm{E}}]\vartheta \tag{2.11}$$

$$\{\mathrm{D}\} = [\mathrm{d}]^t\{\mathrm{T}\} + [\varepsilon^T]\{\mathrm{E}\} + [\rho^{\mathrm{T}}]\vartheta \tag{2.12}$$

The tensors given in eq. (2.9) and eq. (2.10) are not full for the materials discussed here. A certain amount of entries are zero due to symmetry in the crystal structure [15, 21, 66]. Manufacturers typically provide values for the contributing tensor entries of their material.

---

[1] Electric displacement $D_j$ can be written as $D_j = \varepsilon_0 E_k + P_j$, where $P_j$ is electric polarization and $\varepsilon_0$ is the permittivity of vacuum [66].

## 2.3. Piezoelectric piezoelectric sensor response

The constitutive equations described above play a crucial part in the determination of a strain to voltage relationship. While it is mathematically possible from the constitutive equations alone to retrieve a strain to voltage relationship, this disregards other phenomena. In this regard, it is possible to distinguish three regions, see fig. 2.1.

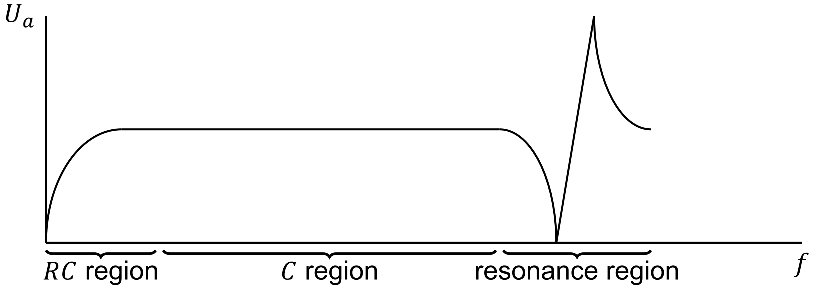

Figure 2.1: Schematic piezoelectric sensor response.

Here, $U_a$ and $f$ represent voltage amplitude at constant strain amplitude and frequency respectively. The $RC$ region response is governed by the resistance. The piezoelectric sensor itself, and additionally the measurement system and wiring have a finite resistance. This resistance allows discharge of the sensor, thereby decreasing voltage amplitude with decreasing frequency [19]. At sufficiently high frequencies, piezoelectric sensor discharge becomes negligible, resulting in the $C$ region. This means response is only compromised by possible external capacitance, resulting from wiring and measurement system. At a certain frequency, electromechanical resonance and antiresonance will occur, which is not desired in measurements [57]. First, a method is presented for the low frequency response. This is followed by a method to define resonance and anti-resonance frequencies.

### 2.3.1. Low frequency piezoelectric sensor response

The method described here is based on Lin and Giurgiutiu [39], Giurgiutiu [21], Shin et al. [69] and Erturk and Inman [16], who have used this in context of vibration measurement and vibration-based energy harvesting. As described in section 1.1.2 the method is a one-way coupling, utilising a predefined strain field.

Both effects from resistance and capacitance can be captured by assuming resistance $R_m$ and capacitance $C_m$ parallel to the piezoelectric sensor. Using lumped elements, this results in the diagram in fig. 2.2 [39], [66], [16]. Here the data acquisition system measures voltage $U$ generated by the charge $Q_s$ of the piezoelectric sensor.

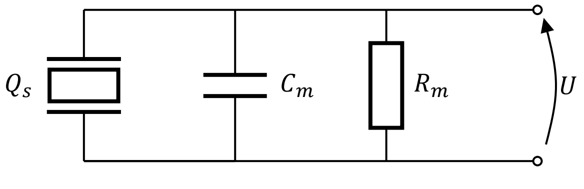

Figure 2.2: Simple piezoelectric sensor measurement circuit.

The governing equation of above circuit is Kirchhoff's current law, given in eq. (2.13). For this particular circuit, it eq. (2.13) can be rewritten to eq. (2.14), where $I_s$ is the current based on the charge $Q_s$ of the piezoelectric sensor and $I_m$ is the current through the external elements.

$$\sum I = 0 \tag{2.13}$$

$$I_s + I_m = 0 \tag{2.14}$$

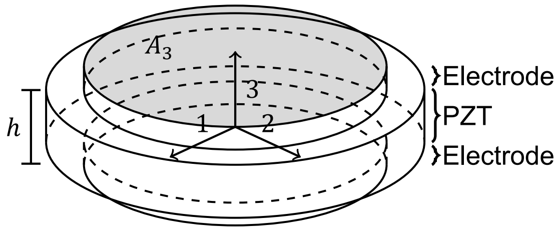

Figure 2.3: Piezoelectric disc sensor orientation.

First, let us zoom in on the piezoelectric sensor. It is known that the current $I_s$ is the rate of charge $Q_s$, eq. (2.15). Given that the charge is the surface integral of the local electric displacement over piezoelectric sensor electrode area $\mathrm{A}$ (fig. 2.3), eq. (2.16) emerges [21].

$$I_s = \frac{d}{dt} Q_s \tag{2.15}$$

$$I_s = \frac{d}{dt} \int \{\mathrm{D}\} \cdot d\mathrm{A} \tag{2.16}$$

Constitutive equation eq. (2.12) can be substituted into eq. (2.16). Note that for this eq. (2.11) should be substituted first into eq. (2.12). The result is given in eq. (2.17). Note that electric field is assumed constant over the electrode area in the evaluation of the integral in eq. (2.16), whereas strain and temperature is not. eq. (2.17) can be simplified to eq. (2.18).

$$I_s = \int [\mathrm{d}]^t [\mathrm{s}^{\mathrm{E}}]^{-1} \left\{ \frac{d\mathrm{S}}{dt} \right\} \cdot d\mathrm{A} + \{\mathrm{A}\} \cdot \left( [\varepsilon^{\mathrm{T}}] - [\mathrm{d}]^t [\mathrm{s}^{\mathrm{E}}]^{-1} [\mathrm{d}] \right) \cdot \left\{ \frac{d\mathrm{E}}{dt} \right\} + \int \left( [\rho^{\mathrm{T}}] - [\mathrm{d}]^t [\mathrm{s}^{\mathrm{E}}]^{-1} [\alpha_{\mathrm{E}}] \right) \frac{d\vartheta}{dt} d\mathrm{A} \tag{2.17}$$

$$I_s = F_S + \{\mathrm{A}\} \cdot \left( [\varepsilon^{\mathrm{T}}] - [\mathrm{d}]^t [\mathrm{s}^{\mathrm{E}}]^{-1} [\mathrm{d}] \right) \cdot \left\{ \frac{d\mathrm{E}}{dt} \right\} + F_\vartheta \tag{2.18}$$

Additionally, assuming electric field constant over thickness $h$, given in fig. 2.3,

$$\left\{ \frac{d\mathrm{E}}{dt} \right\} = \frac{d}{dt} [E_1 \quad E_2 \quad E_3]^t = \left[ E_1 \quad E_2 \quad \frac{1}{h} \frac{dU}{dt} \right]^t .$$

For piezoelectric discs, $E_3$ is the only electric field intensity that contributes to voltage $U$. This is due to electrode geometry $\mathrm{A}$, that is:

$$\{\mathrm{A}\} = [0 \quad 0 \quad A_3].$$

Next to the piezoelectric sensor, current is running through the resistor and capacitor as well. Their combined current $I_m$ can be calculated through Ohm's law:

$$I_m = \frac{U}{R_m} + C_m \frac{dU}{dt} \tag{2.19}$$

Getting back at eq. (2.14), the following nonhomogeneous differential equation is obtained[2]:

$$F_S + F_\vartheta + C_s \frac{dU}{dt} + C_m \frac{dU}{dt} + \frac{1}{R_m} U = 0 \tag{2.20}$$

In this case, $F_S$ and $F_\vartheta$ are current source terms whereas $C_s$ is representative for the capacitive behaviour of the piezoelectric sensor itself. Differential equation eq. (2.20) reveals the underlying circuit of the piezoelectric element and the full system for low frequency (fig. 2.4).

To analytically solve eq. (2.20), generally strains are assumed harmonic[3]. Neglecting $I_m$ simplifies the solution to the one given by Gopalakrishnan et al. [22]. The method is verified using two sources.

---

[2] Similar to eq. (6b) of (Shin).

[3] In most applications, temperature effects are neglected.

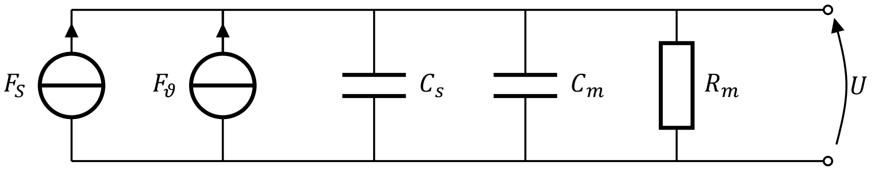

Figure 2.4: Simple piezoelectric sensor measurement for low frequency applications.

| property | unit | [39] | this research |
|---|---|---|---|
| strains measured | $\mu$m/m | 338 | - |
| voltages measured | V | 30.8 | - |
| voltages calculated | V | 30 | 30 |

Table 2.1: Comparison of voltage with Lin and Giurgiutiu [39].

### 2.3.2. Verification of $C$ region

Lin and Giurgiutiu [39] did free vibration tests on an aluminium beam with a piezoelectric sensor mounted on the top surface. Shin et al. [69] performed forced vibration tests on a glass-epoxy composite with sensors embedded. In both cases, the environment was considered isothermal and there were comparisons with strain gauges.

In the case of Lin and Giurgiutiu [39], piezoelectric sensor behaviour was regarded as one-dimensional, whereas experimental measurements were performed with square sensors. Also, an external capacitance was assumed. Values calculated in Lin and Giurgiutiu [39] should correspond perfectly with those determined in this verification, since both values for measured strain and measured and calculated voltage are given. Indeed this is the case, as can be seen in table 2.1.

Sensor response in Shin et al. [69] was based on three-dimensional strains and electromechanical properties. As a result a voltage to strain ratio was given. It was assumed that strain measured by the strain gauge is equal to the weighted average strain in the embedded sensor. In their geometry, this was valid for lower modes while the embedded piezoelectric sensor is close to the surface near the strain gauge [69]. While no direct strains are given in the comparison, a figure[4] gives a range of strains. In table 2.2 estimations of the strains are given, together with voltages based on these estimations. It can be clearly seen the voltage to strain ratio presented in Shin et al. [69] falls in the range of estimated voltages.

### 2.3.3. Low frequency limit

Getting back at eq. (2.20), all terms except for the resistance term are dependent on time derivatives. For low frequencies, terms with a time derivative decrease, including the strain source term, whereas resistance remains unaltered. The result is a decreasing voltage when frequency is decreasing. Physically this effect can be regarded as electrical discharge. For low frequency measurements, it is of key importance to have insight in the parallel resistance of the system. As mentioned in the introduction of this subsection, the sensor, the wiring system and the measurement device are sources of finite resistance. Furthermore, for embedded sensors, the material surrounding the electrodes are a source as well.

### 2.3.4. Electromechanical resonance

In order to assess whether elastic wave emission signals are affected by electromechanical resonance it is needed to get a grasp on the frequencies associated with electromechanical resonance.

Implications of electromechanical resonance are that amplitudes of certain frequencies within signals are reduced whereas, due to subsequent antiresonance, others are strengthened. The potential loss and deformation of information can be a reason to avoid having sensors with resonance in the frequency

---

[4] Figure 12 of Shin et al. [69].

| property | unit | [69] | this research |
|---|---|---|---|
| average strain estimated | $\mu$m/m | - | 140, 200, 260 |
| voltage/strain measured | Vm/$\mu$m | 0.086 | - |
| voltage/strain calculated | Vm/$\mu$m | 0.081 | 0.1262, 0.0883, 0.0679 |

Table 2.2: Comparison of voltage with Shin et al. [69].

band of interest [57]. On the other hand the increased sensitivity provided by antiresonance might allow acoustic wave detection at a relatively large distance.

Although it might not be expected from the circuitry given in eq. (2.20) and fig. 2.4, piezoelectric equations are prone to electromechanical resonance. During electromechanical resonance, there is an increase in strain to voltage ratio. Physically, the phenomenon is linked to mode shapes having strain distributions which are akin to the distribution of the electric field over the electrodes of the piezoelectric sensor [21]. In the electrical system, electromechanical resonance is followed by electromechanical antiresonance, sporting the opposite effect [14].

To provide a link to fig. 2.4 and eq. (2.20), electromechanical resonance can be modelled by expanding current source term $F_S$ to include a motion equation. Whilst omitting temperature dependency $F_\theta$ and system particulars $C_m$ and $R_m$, this leads to fig. 2.5[5]. Inherently, the motion equation introduces mechanical resonance through inertia $M$ and stiffness $K$. In electromechanical antiresonance, inertia $M$, an inductor in electrical analogy, interacts with the capacitance of the electrical system $C_s$ [5, 28, 56].

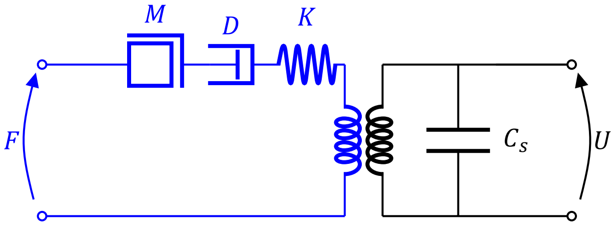

Figure 2.5: A visual explanation of electromechanical resonance. Blue and black colours represent the mechanical and electrical system respectively.

Undescribed elements in the system include external mechanical forcing $F$ and displacement velocity $\frac{du}{dt}$, which in electrical analogy is equal to potential difference and current. $D$ is damping in the equation of motion. The two coils, a transformer, couple between the mechanical and electrical system.

It is expected that the embedding procedure results in changes of the resonance behavior of the piezoelectric sensor when compared to a freely vibrating sensor. On the mechanical side, this is due to the host material constraining the piezoelectric sensor in both normal and shear strains, altering its stiffness term. Also damping and mass terms are considered to be affected.

On the electrical side, embedding can result in an altered capacitance due to excessive pressure and temperature disturbing the crystal alignment [19]. The latter effect is expected to be limited due to the piezoelectric sensor material having a maximum working temperature and a Curie temperature significantly higher than the experienced maximum temperature, 250 °C and 350 °C versus 180 °C [50].

To characterise electromechanical resonance behavior, typically impedance measurements are performed [14, 21, 26, 63, 66]. Electromechanical resonance is associated, next to an increase in deformation, with an increase in current. Through $Z = \frac{V}{I}$, impedance $Z$ is affected. Coupled field FEM can be employed and for simple geometries, such as freely and constrained vibrating discs or rods, analytical models exist [21].

---

[5] The system drawn may be seen as a Butterworth-Van Dyke circuit, and contains simplifications that render it invalid away from the electromechanical resonance of the modelled mode. A more complete system is provided by [48].

## 2.4. Elastic waves in a composite beam

As described in section 1.1.3 damage growth is accompanied with a sudden emission of mechanical energy. Depending on the frequency content in this emission and the dimensions of the structure, either vibrations, elastic bulk waves, guided waves[6] or surface-guided waves[7] are formed within the structure [21]. Each are formed due to a specific interaction with the structure's boundaries. In the case of fibre-reinforced composite plate-like structures, typically damage-related elastic wave emission propagates as a guided wave.

Fundamental guided waves exist in three types of propagating modes. Symmetric modes are related to axial motion while antisymmetric modes relate to flexural motion [21]. Shear horizontal modes exist as well, but are not relevant in this research and are therefore disregarded. Their propagation is parallel to the plate surface. The direction of the particle motion is for either mode a combination of in-plane and out-of plane motion [37]. The interaction with the plate boundary gives that both modes show dispersive behaviour. This means the propagation velocity of the excitation is frequency-dependent. Detailed descriptions can be found in Giurgiutiu [21], Nayfeh [55] and Lempriere [37].

Guided plate waves adhere to the general theory of linear elasticity[8], meaning

$$\rho\,\{\ddot{\mathrm{u}}\} + \nabla\cdot\{\mathrm{T}\} = \{\mathrm{f_v}\} \tag{2.21}$$

is evaluated to retrieve deformations $\{\mathrm{u}\}$. Here $\nabla\cdot$ and $\{\mathrm{T}\}$ represent the divergence operator and the stress tensor whereas $\rho$ and $\{\mathrm{f_v}\}$ define specific mass and external body force. Finite element methods can be used to solve the equations. To accurately model guided waves in composites, relatively small elements or higher order shape functions are used [36] or both. The spectral element method[9] is a finite element method where high-order shape functions are employed. In this research the used shape functions are Legendre-Gauss-Lobatto-Lagrange polynomials, making the simulation efficient with regard to the computational power[60]. A visualisation of the shape functions in use is given in fig. 2.6. For time integration, an explicit method using the central difference approximation, given in eq. (2.22), is applied [60]. Here $i$ represents the time step. For a more detailed description of the spectral element method Komatitsch and Tromp [30] and Pahlavan [60] may be consulted.

$$\begin{gathered}[\mathrm{M}]\,\{\ddot{\mathrm{u}}_i\} + [\mathrm{K}]\,\{\mathrm{u_i}\} = \{\mathrm{f_{v,i}}\}\\ \text{with:}\\ \{\ddot{\mathrm{u}}_i\} = \frac{\{\mathrm{u_{i+1}}\} - 2\{\mathrm{u_i}\} + \{\mathrm{u_{i-1}}\}}{dt^2}\end{gathered} \tag{2.22}$$

## 2.5. Conclusions

Referring to the introduction chapter 1, the research subquestions can be answered:

> *What are the governing physics of piezoelectricity and how can they be modelled in piezoelectric sensor applications?*

The piezoelectric effect is a small scale crystal deformation, altering electric polarity. This is captured in electromechanical constitutive equations. In piezoelectric sensor measurements, additional effects regarding parallel resistance and reactance are to be accounted for. Assuming one-way coupling, piezoelectric sensor response is retrieved by solving differential equation eq. (2.20).

> *What are elastic waves and how can they be modelled in composites for analysis of elastic wave emissions?*

Guided elastic waves are high-frequency elastic deformations that propagate across a plate due to the interaction with a boundary of the material. The phenomenon adheres to the theory of linear elasticity. For computational efficiency, a spectral element method is used in this thesis.

---

[6] Lamb waves and shear horizontal waves.

[7] Rayleigh waves.

[8] In this description, damping is not taken into account.

[9] In time-domain, not to be confused with the spectral element method in frequency domain.

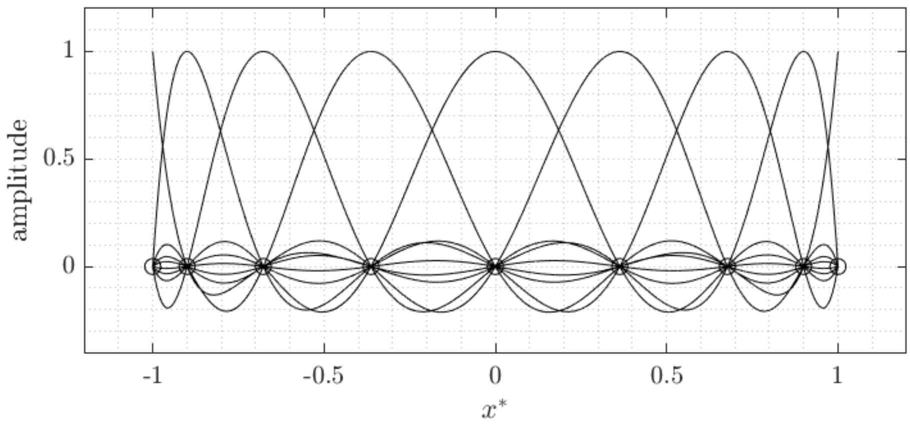

Figure 2.6: Legendre-Gauss-Lobatto-Lagrange polynomials of order 8. The local coordinate is represented by $x^*$.

# 3

# Experiments

## 3.1. Introduction

As part of the feasibility study, experiments were performed involving measurements with embedded piezoelectric sensors. Furthermore insight is provided in the mechanical properties of the host material.

The design of the specimen is given and clarified first. Subsequently, for each experiment the underlying motivation is explained, followed by a description of the conduct of the experiment.

## 3.2. Specimen design

The development of a composite structure with embedded piezoelectric sensors relates to research subquestion:

> *How can a piezoelectric sensor be embedded in a composite structure?*

This question is answered by first giving an overview of the resulting design, followed by an elaboration with regard to the piezoelectric sensor, wiring, electrical insulation and the host material.

### 3.2.1. Design overview

A general overview of the design is given in fig. 3.1, showing the different components involved. Each of the components is elaborated upon in sections 3.2.2 to 3.2.5.

### 3.2.2. piezoelectric sensor type

In general applications of piezoelectric sensors, such as strain measurement and damage localisation, in-plane directional sensitivity requires extra attention. Disc shaped piezoelectric sensors provide omnidirectional sensitivity [22]. Therefore, in this research disc shaped piezoelectric material, with the electrodes on the faces of the disc, was used.

The dimensions of the disc were a based on what was readily available by the manufacturer. A thin disc is opted to ease accommodation into the layered host material. To gain insight into the effect of piezoelectric sensor radius on measurements, two radii were used. In total, six piezoelectric sensors with a radius of 10mm and a thickness of 0.29mm (called large piezoelectric sensors or L) and twelve piezoelectric sensors with a radius and thickness of 3.5mm and 0.24mm (small piezoelectric sensors or S) were embedded.

The piezoelectric material chosen is PZ27, a product of Ferroperm TM Piezoceramics. This is a PZT

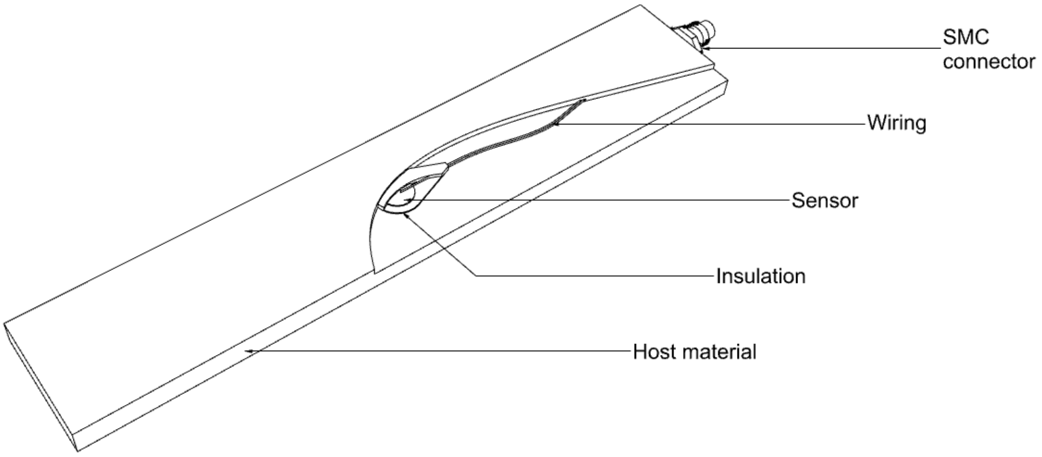

Figure 3.1: Cut-through visualisation of the specimen design showing its different components.

composite material with a depolarisation temperature[1] and recommended maximum working temperature of 350°C and 250°C [50], both which were higher than the host material curing temperature of 180°C [24]. Electrodes were made of silver.

### 3.2.3. Wiring

To connect the piezoelectric sensor to the data acquisition system, it is opted to lead wiring in-plane through the host material. This is a convenient choice since little extra preparation of the host material is needed. Known alternatives are leading wiring perpendicular to the ply stack [20, 47, 71], embedding inductive coils [7] or embedding an analog-to-digital converter and wireless transmitter [35][2]. It is known thick wiring can impede host material structural integrity for both glass and carbon fibre-reinforced plastic host material [45, 71, 74][3]. Enamelled[4] copper wiring with a diameter of 0.15mm was used[5]. The wiring was bifilar, to ease manufacturing. To prevent breakage of the wiring at the interface between the host material and the outside world, at the edge of the host material, a SMC type connector was embedded. To join the piezoelectric sensor to wiring, S-Sn95Ag4Cu1 solder was used, since the silver electrodes of the piezoelectric sensor were incompatible with lead-containing solder. The wiring and connectors are depicted in fig. 3.2.

### 3.2.4. Insulation

As experienced during manufacture, the carbon fibre-reinforced plastic host material used is electrically conductive. The piezoelectric sensor electrodes are conductive as well, creating a need for insulation. Based on the works of Andreades et al. (2018) and Sala et al. (2004) [3, 67], before embedding the piezoelectric sensor in the host material, first the piezoelectric sensor is embedded manually between two layers of woven glass fibre-reinforced plastic (HexForce 00106 and Araldite LY 5052), by means of a wet lay-up method. Polyimid/Kapton insulation is not opted for due to the relatively complex nature of processing the surface whilst retaining the risk of premature delamination. A thermoplastic layer, during host material curing, might flow away from certain locations on the piezoelectric sensor, exposing the

---

[1] Generally known as Curie temperature. At higher temperature the crystal structure changes, which allows misalignment of the crystals when cooling down [11, 19, 21, 52, 66].

[2] It was deemed the former alternative is cumbersome during manufacture whereas developing the latter alternatives was not feasible.

[3] The first source describes optical fibres. In this context, the effect of wiring and optical fibres on host material structural strength is considered equivalent.

[4] Urethane lacquer.

[5] In an earlier prototype, 0.05mm diameter wiring was used, but this proved to be very sensitive to breakage during manufacturing. Also, coaxial wiring with an outer diameter of 0.15mm was considered, but connecting this to the piezoelectric sensor and connector was prohibitively complicated.

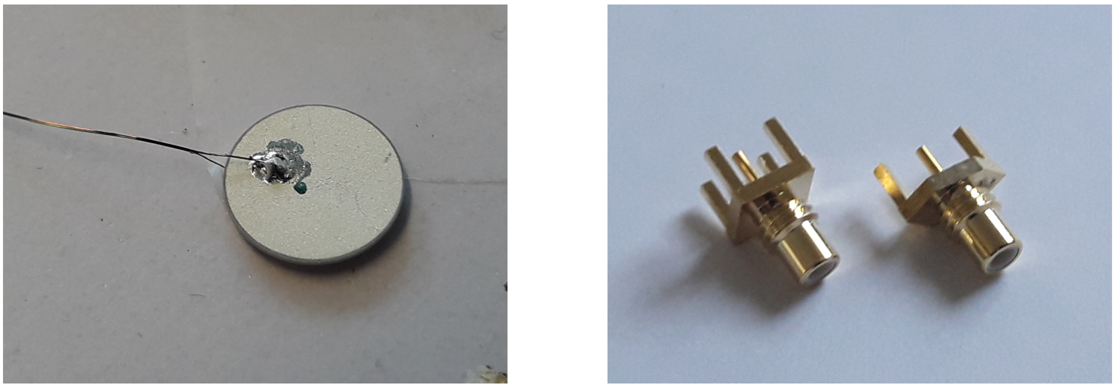
(a) (b)

Figure 3.2: Wiring. (a) Small piezoelectric sensor after soldering, prior to glass insulation. (b) SMC connectors, milled to shape. This proved to be a sturdy method for communication with the embedded piezoelectric sensor.

electrodes to conductive fibres. After curing the insulation is trimmed around the piezoelectric sensor and wiring, leaving a drop-like shape. No processing of the glass surface is performed afterwards to ensure an intact insulation. The total thickness of the insulated piezoelectric sensor ranges from 0.7mm to 1.2mm. For manufacturing convenience and since the connector is in a remote area with respect to mechanical loading during the failure experiment, the connector is insulated using Kapton tape.

### 3.2.5. Host material

From the faculty of aerospace a batch of Hexcel AS4/8552 unidirectional carbon fibre-reinforced plastic prepreg material[6] was accessible. Material properties were retrieved from the manufacturer [24]. This material came in rolls with a width of 150mm and a ply thickness of 0.18mm. To simplify manufacturing procedure, the lay-up of the host material was in a symmetric cross-ply fashion in the sequence $[[0, 90]_7, 0]_s$, resulting in a thickness of 5.4mm. From the 20th to the 25th layer, cut-outs were made to accommodate the piezoelectric sensor and the connector. Initial trials of embedding the piezoelectric sensor without cut-out failed due to the relative height of the piezoelectric sensor in combination with the stiffness of the prepreg. The specimens were made from plates with a length and width of 150mm. These plates contain at maximum 5 piezoelectric sensors, as given in fig. 3.3. The manufacturing procedure was performed in accordance with the guidelines [24], setting the autoclave at a pressure[7] of 7bar and a temperature of sequentially 120°C and 180°C. A smooth surface finish was obtained by means of a backing plate.

After curing and performing measurements on nondestructive elastic wave emissions, explained in section 3.3 the plates were cut into strips with a width of 27mm, using a Proth diamond saw. In total 25 specimens were made; 12 with a small piezoelectric sensor embedded, 6 with a large piezoelectric sensor embedded and 7 specimens without piezoelectric sensor. After performing the experiments, spare specimens 1S and 1L were cut open (fig. 3.4) to check both the general placement of the piezoelectric sensor, as well as the condition of the fibres. It can be seen the cut-out introduces distortion of surrounding fibres. Also the glass insulation has a varying thickness over the piezoelectric sensors and seems to show a void, or remnants of an inclusion, in the large piezoelectric sensor.

## 3.3. Nondestructive elastic wave emissions

Pencil leads were broken to excite guided elastic waves in the specimens that are analogous to damage related elastic waves. The guided waves were captured by both an embedded piezoelectric sensor as well as by a surface-mounted commercial piezoelectric sensor. The experiment gives insight in the functioning of the sensor as well as in its signal quality.

---

[6] At the date of manufacture, the material was over the formal date of expiration.

[7] Relative to ambient pressure.

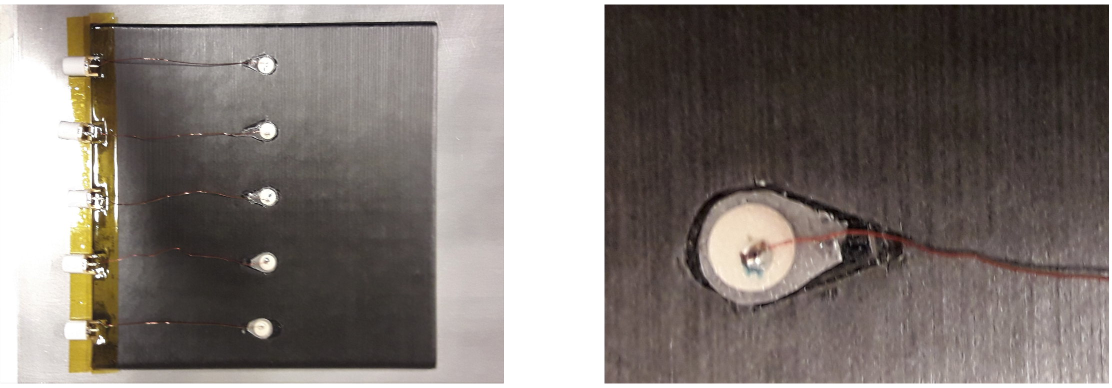

(a) (b)

Figure 3.3: Specimen manufacture. Depicted is the 22th layer, showing the piezoelectric sensors. (a) A full plate containing small piezoelectric sensors. (b) piezoelectric sensor 4S during embedding. Note the glass insulation and the cut-out in the carbon fibre-reinforced plastic lay up.

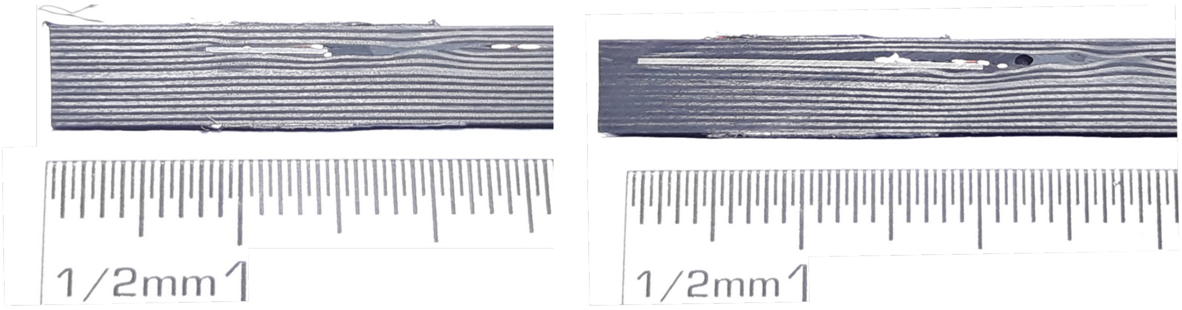

(a) (b)

Figure 3.4: Through-thickness cuts of specimens 1S and 1L. (a) Small piezoelectric sensor 1S. Fibre waviness is visible near the cut-out region. (b) Large piezoelectric sensor 1L. Also here, fibre waviness is visible. The darker dot close to piezoelectric sensor is either an air pocket or an inclusion that was released after cutting.

*To what extent do piezoelectric sensors survive embedding procedure?*

During testing, pencil leads (2H 0.5mm) from a mechanical pencil with a Nielsen shoe [4] were broken at predefined locations, being 20mm, 40mm or 60mm away from the piezoelectric sensor centre, parallel to 0° fibres. The specific setup is given in fig. 3.5. The testing contains two phases. In the first phase, at least 10 leads per piezoelectric sensor were broken in order to separate functioning piezoelectric sensors from malfunctioning ones, using the full 150×150mm plates. In the second phase, specimen beams with a width of 27mm were subject to the same pencil lead breaks. The commercial sensor is used as a reference. Results are given in appendix A.

A commercial piezoelectric sensor (Mistras R15I-AST) was placed on the specimen surface at the location and side of the embedded piezoelectric sensor. The commercial piezoelectric sensor was secured to the specimen by means of a gummy coupling agent (Pritt poster buddies) and hot glue in the first and second phases. To increase the signal to noise ratio, the embedded piezoelectric sensor response was amplified with 40dB using a Vallen AEP-5H charge amplifier. The commercial piezoelectric sensor has an amplifier of 40dB build-in. Both the embedded and commercial piezoelectric sensor were connected to a Vallen AMSY-6 data acquisition system. Thresholds for the data acquisition were set to 70dB and 35dB in the first and second phase for both the embedded and commercial piezoelectric sensors. A band pass filter was applied, filtering anything outside 90 to 300 and 20 to 960kHz in the first and second phase. Pretrigger time was 200$\mu$s. The total length of the measurement varied depending on the signal. The AMSY-6 system has an upper limit of 94dB. Higher responses were clipped. A visual overview of the measurement systems is given in fig. 3.6.

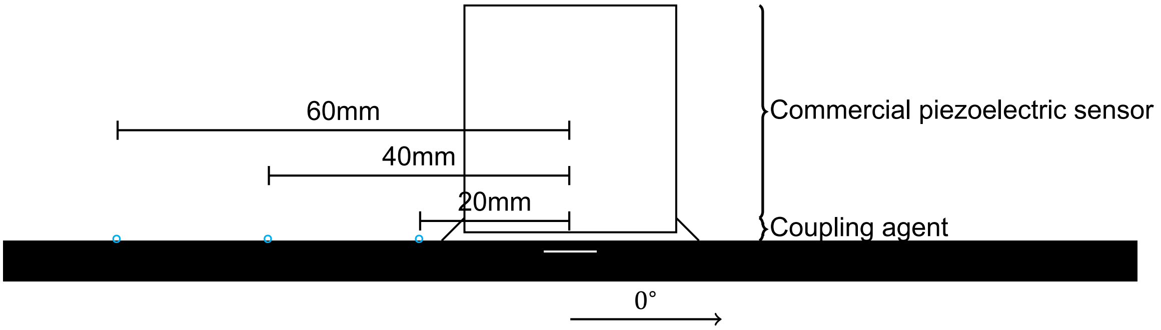

Figure 3.5: Guided wave experimental set-up. Black, white and blue represent composite host material, embedded piezoelectric sensor and locations of pencil breaks.

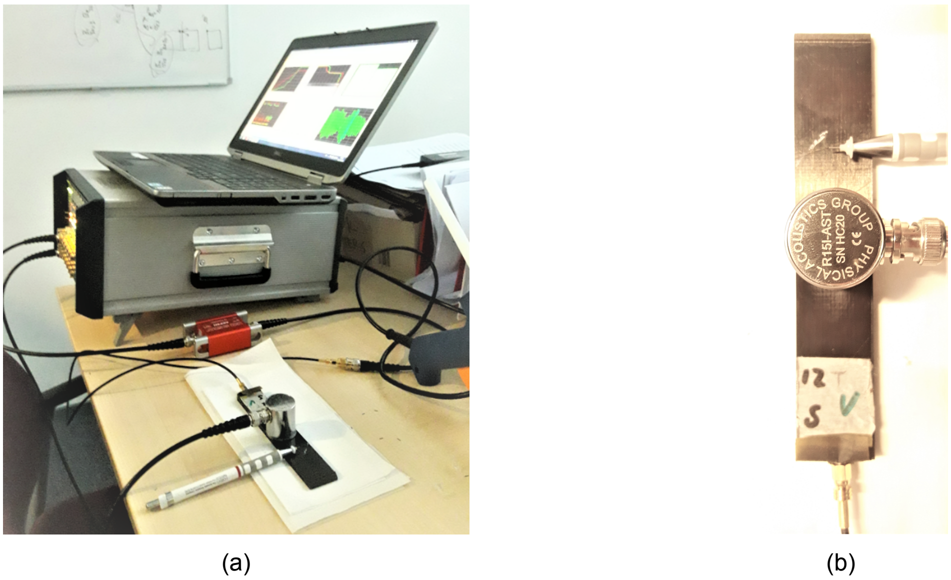
(a) (b)

Figure 3.6: Performing pencil lead breaks, second phase. (a) gives the general arrangement, with the AEP5H preamplifier in red and the AMSY6 data acquisition system in grey. (b) shows the specimen set up, with the mechanical pencil with Nielsen shoe on the top, commercial R15I-AST sensor in the middle and the SMC connector for the embedded piezoelectric sensor on the bottom of the figure.

## 3.4. Electrical impedance

It is expected that the embedding procedure results in a change in the resonance behavior of the sensor when compared to a freely vibrating sensor. This is due to the host material constraining sensor motion as well as altering mass characteristics. This experiment is complementary to research-subquestion:

> *How does embedding a sensor affect its electromechanical resonant behaviour compared to a non-embedded sensor?*

To quantify the effect of embedding on electromechanical resonance, impedance measurements are performed [14, 21, 26, 63, 66, 68]. The measurements are compared to an analytical model of the impedance. Two Large and two small piezoelectric sensors where examined, two of each embedded and at two of each virtually unconstrained. The latter is pictured in fig. 3.7a.

As explained in section 2.3.4 the experiment involves exciting the piezoelectric sensor electrically with a constant amplitude and varying frequency voltage. In the meantime system impedance is monitored. Electromechanical resonance is associated, next to an increase in deformation, with an increase in current. Through $Z = \frac{U}{I}$, impedance $Z$ is affected. Next to this, at resonance, current and displacement velocity are in phase with voltage, meaning phase angle $\theta$ is shifted from -90°to 90°[73].

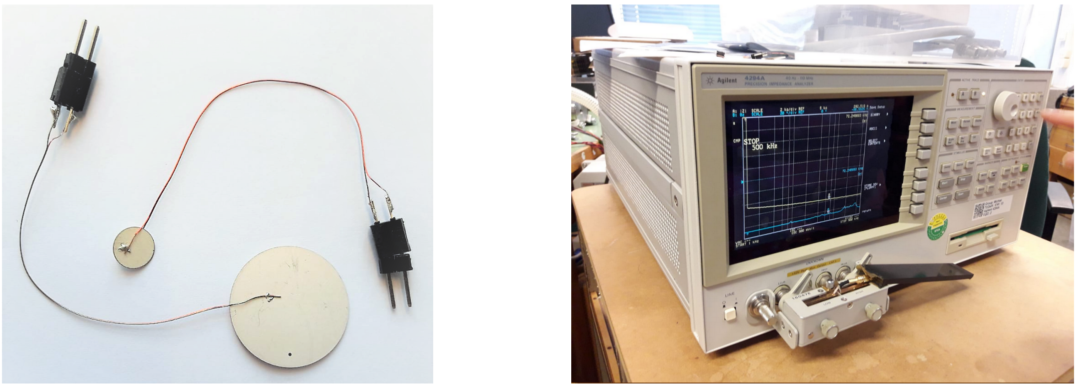

(a) (b)

Figure 3.7: Impedance measurements. (a) Virtually freely vibrating sensors. (b) Agilent 4292A network analyzer measuring embedded sensor impedance.

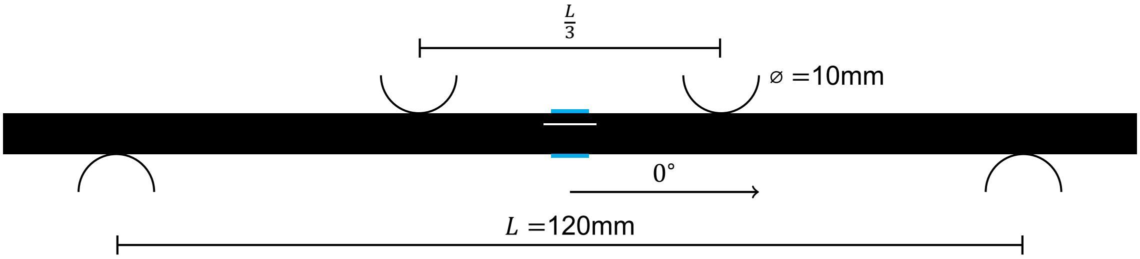

Figure 3.8: Bending test experimental set-up. The colours black, white and blue relate to the host material, piezoelectric sensor and strain gauge placement.

To prevent wiring inductance and capacitance to possibly disturb measurement results, wiring is kept as short as possible. The system used is an Agilent 4292A precision impedance analyzer, exciting the sensor with a 1V voltage amplitude. Impedance magnitude $|Z|$ and phase angle $\theta$ are first monitored over a domain of 1000Hz to 10MHz to determine the domain of interest, which receives a second sweep. Increments of the frequency are logarithmic by default, resulting in a better resolution at low frequencies compared to higher frequencies. A view of the measurement of an embedded sensor is given in fig. 3.7b.

## 3.5. Bending tests setup

In the following subsections, sections 3.5.1 to 3.5.3, three experiments are described. The material and methods of those experiments were similar. In this section a general description of the set up is given. The tests revolve around four point bending of the beam-shaped specimens.

It was opted to adhere as much as possible to the applicable standard, being ASTM D6272 [10]. The machine used was a computer controlled Zwick/Roell 1455 universal testing machine with a maximum load of 20kN. The machine has an integrated system for monitoring the load (with a load cell) and the displacement. The specimens were placed, as displayed in fig. 3.8, between steel load pins and support pins with a diameter of 10mm.

To complement the load cell and to get a more accurate description of the longitudinal strains experienced by the specimen in bending, strain gauges were placed on the top and bottom sides of the specimen at the middle of the length and width. These were of type KFGS-5-120-C1-11 and had a gauge length of 5mm and a resistance of 120.2Ω[32]. A cyanoacrylate adhesive was used to attach the strain gauges to the composite material.

During testing, the strain gauges were attached to individual inlets of a Peekel Picas amplifier system, resulting in the two strain gauges both working in a quarter wheatstone bridge. Via a NI-USB 6229 data

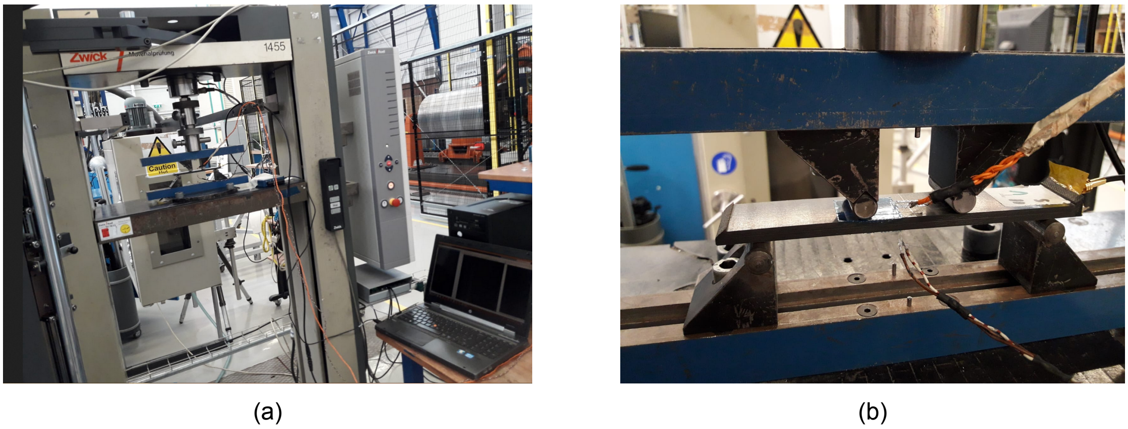

(a) (b)

Figure 3.9: Low-frequency bending. (a) gives the general arrangement. (b) shows the real-life placement of the specimen.

acquisition system, the amplified signal was stored in the machine computer. Pictures of the bending tests are given in fig. 5.1.

### 3.5.1. Low-frequency excitation

Bending tests were performed to evaluate the piezoelectric sensor response at controllable low frequencies. Also, the experiment provided insight in the minimal frequency that can be measured by the piezoelectric sensors. The measurement results of this experiment are presented in section 4.4 and used in chapter section 5.2 to validate the electromechanical model presented in sections 2.3.1 and 2.3.3. Four subquestions are related to this experiment:

> *To what extent do piezoelectric sensors survive embedding procedure?*
>
> *How is the agreement between modelled and measured sensor responses?*
>
> *What is the variation of responses between measurements and between piezoelectric sensors?*
>
> *Given the measurement set-up, what is the minimum frequency the piezoelectric sensor can measure strain accurately?*

The testing machine (from section 3.5) was configured to perform a cyclic motion with a predetermined vertical head velocity $v_m$. The displacement was load governed, with a minimum and maximum downward load of $F_{LC,min}$ =0.5N and $F_{LC,max}$ =20N respectively. The stroke was based on a presumed piezoelectric sensor response amplitude, which may not be over 10V to spare the data acquisition system [53].

The specimens with embedded piezoelectric sensors were tested. The specimens were placed such that piezoelectric sensors were on the compressive side of the beam, for the piezoelectric sensor material has a larger strength in compression than in tension [51, 65]. Per specimen at least three tests were performed, one for each head velocity $v_m$=10mm/min, 1mm/min and 0.1mm/min. The velocity relates to frequency through $f_m \approx 0.18 v_m$Hz. Accordingly, excited frequencies were $f_m \approx$ 0.018Hz, 0.18Hz and 1.8Hz.

For head velocities $v_m$=10 and 1mm/min the specimens were subjected to 20 cycles. This amount of cycles derives from the machine showing slight deviations during the first cycles. At $v_m$ = 0.1mm/min, only 5 cycles were performed, due to the large amount of time needed per cycle.

As pre-qualification, first each specimen was tested at the $v_m$ = 10mm/min excitation. If no signal or only noise was recorded, the piezoelectric sensor was considered faulty and the lower velocity tests were not executed. Before each test, strain gauges were calibrated. Also, during all tests, the load cell response was monitored to check for machine nonuniformity or lagging[8]. Tests were redone when this

---

[8] In this case, the sudden and unexpected temporary stopping of the machine before finishinig the loading sequence.

| Specimen type | piezoelectric sensor loading | Number of specimens |
|---|---|---|
| no piezoelectric sensor (N) | - | 4 |
| small piezoelectric sensor (S) | compression | 2 |
| small piezoelectric sensor (S) | tension (T) | 2 |
| large piezoelectric sensor (L) | compression | 2 |

Table 3.1: Number and types of specimens tested for stiffness and failure.

was encountered.

The setup as described in section 3.5, is supplemented by two NI-USB 6002 data acquisition systems. One handles the piezoelectric sensor response, while the other was connected to the machine load cell. Having separate systems prevents cross talking between the piezoelectric sensor and the load cell[9]. These data acquisition systems were connected to a PC, allowing direct assessment of the results. The load cell data, which was also recorded by the test machine computer, was used to correct for time lags between measurements of the strain gauges and the piezoelectric sensor.

### 3.5.2. Specimen flexural properties

To retrieve flexural mechanical properties of specimens with embedded piezoelectric sensors compared to pristine specimens, monotonic destructive bending tests were performed. Topics researched were failure modes, flexural stiffness, maximum strain, maximum load, and toughness. This section discusses research question:

> *To what extent are flexural mechanical properties of the composite host material influenced by embedding a piezoelectric sensor?*

The experiment, for each specimen, was divided into two parts. In the first part, the aim was to determine stiffness characteristics, the specimen was placed in the machine as per section 3.5. A force of 200N was exerted by the machine monotonically at $v_m$ =1mm/min. Afterwards, the specimen was relieved of the force. In the second part, failure of the specimens was examined. AL6082 alloy tabs were placed on the support and loading pins to prevent compressive failure as calculated per Young et al. [75] and Hexcel corporation [24]. The tabs had a width and thickness of 15mm and 3mm respectively. Three piezoelectric sensors were used in the test, the embedded piezoelectric sensor, and two commercial piezoelectric sensors. The aim of these piezoelectric sensors was to acquire ultrasonic elastic waves related to damage growth and specimen failure. More on this is given in section 3.5.3. The specimens were loaded, again at $v_m$ =1mm/min. The test stopped once the force needed to continue monotonic deflection dropped to less than half the maximum force exerted in the test. Due to time constraints, less specimens were tested than the recommended 5 per type by ASTM-D6272 [10]. Specifics of the tested specimens are given in table 3.1.

### 3.5.3. Specimen failure and elastic wave emissions

Destructive bending tests present an opportunity for the piezoelectric sensors to capture real life damage related elastic wave emissions. Furthermore, they provide the means to identify to what strain levels the piezoelectric sensors can pick up guided wave signals. Also, general performance of the embedded piezoelectric sensors to real-life damage emissions was compared to commercial piezoelectric sensor performance. This is linked to research subquestion:

> *To what extent in terms of signal quality and maximum strain is the embedded piezoelectric sensor able to measure damage-related guided elastic wave emissions?*

As mentioned in section 3.5.2, during failure testing, the embedded piezoelectric sensor and two commercial piezoelectric sensors were connected to the AMSY-6 data acquisition system. Similar to section 3.3, the embedded piezoelectric sensor was amplified 40dB with a AEP-5H preamplifier. The two commercial piezoelectric sensors were placed 32.5mm away from the specimen centreline (centre to centre) on the bottom side of the specimen. In order to reduce noise capture, thresholds of 70dB and 35dB were set for the embedded and commercial piezoelectric sensors respectively. A band pass filter was applied, filtering anything outside 20 to 960kHz. Pretrigger time was 200$\mu$s. Total length of the measurement varied depending on the signal. The AMSY-6 system has an upper limit of 94dB. Higher responses were clipped. Results of the test described are given in section 4.6.

---

[9] That effect was experienced during trial measurements.

# 4

# Experimental results and discussion

## 4.1. Introduction

Following the conduct of the experiments, described in chapter 3, results are presented and discussed in this chapter.

Among the results first the survival of the embedded piezoelectric sensors inside the CFRP host material is assessed. This is followed by the results and discussions related to the nondestructive elastic wave measurements, electrical impedance tests, low-frequency excitation, specimen failure and elastic wave emissions during specimen failure.

## 4.2. Sensor survival

During different experiments, it appeared a reasonable number of sensors were functional. For low-frequency flexural excitation experiments, nondestructive elastic wave excitations and the flexural failure tests, the functionality of the sensors is mapped, given in table 4.1. The specific results of the nondestructive elastic wave excitations per sensor are given in appendix A.

| Specimen nr. | 1S | 2S | 3S | 4S | 5S | 6S | 7S | 8S | 9S | 10S | 11S | 12S | 1L | 2L | 3L | 4L | 5L | 6L |
|---|---|---|---|---|---|---|---|---|---|---|---|---|---|---|---|---|---|---|
| Low-frequency excitation | x | v | x | x | v | v | x | v | v | x | v | v | x | v | v | x | v | x |
| Elastic wave emissions | x | v | v | v | v | v | x | v | v | x | v | v | x | v | v | x | v | x |
| Specimen failure |  | x |  | x | x |  |  |  | x |  |  |  |  | x | v |  |  |  |

Table 4.1: Functioning sensors per test. a x represents malfunctioning, v properly functioning.

Sensors that do not collect any data coincide with completely short-circuited systems, having a resistance in the order of 1Ωto 10Ω. Sensors not able to capture pencil breaks but collecting noise-like data relate to zero capacitance measurements. This may be an indication for broken wiring.

The effect of sensors functioning at high frequency but not at low frequency can be due to a limited short-circuit. Resistances in the order of 1000Ωhave been measured[1], far lower than a pristine embedded sensor would have, but higher than complete short-circuit. As explained in chapter section 2.3.3, this resistance shifts the low-frequency limit of the system, resulting in high-frequency guided waves being detectable only.

During the failure tests, 5 out of 6 previously working sensors did capture noise before commence of the testing to such extend it interfered with the measurements of commercial sensors. Possibly this is due to either prior breakage of the sensor or wiring or the connection from the specimen to the pre-amplifier was malfunctioning, causing the assembly to work as an amplified antenna. However, this phenomenon could not be reproduced afterwards with remaining unbroken embedded piezoelectric sensors using the same cabling as used during the failure test. The source of this malfunctioning will be the subject of future investigations.

---

[1] Using a Fluke 117 multimeter.

As an answer to research subquestion:

> *To what extent does the embedded piezoelectric sensor design survive the manufacturing process?*

The piezoelectric sensors used in the design were able to survive the manufacturing process and record data. Out of 12 small sensors, 7 did record low-frequency cyclic bending. In the case of large sensors, this number is 3 out of 6. Nondestructive elastic wave emissions were detected by 9 out of 12 small sensors, and 3 out 6 large sensors.

## 4.3. Electrical impedance

Electrical impedance measurements were performed as described in section 3.4. Results are given in figs. 4.1 and 4.2 for impedance magnitude $|Z|$ and phase angle $\theta$.

The values are compared to an analytical method given by Giurgiutiu (2007)[21] and Qing et al. (2006)[63]. Impedance characteristics are retrieved using a similar procedure as followed in section 2.3.1, except for current $I \neq 0$ due to the external electric excitation. Axisymmetric in-plane vibrational modes were considered. Variations over the thickness are disregarded. At the circumferential edge of the sensor, boundary conditions are applied, being zero radial stress for unconstrained vibration. A damping term of $0.01 \cdot j \cdot s_{11}^{E}$ is added for the sake of stability.

For the freely vibrating sensors, it is clear that, during electromechanical resonance, impedance reaches a minimum, whereas, during electromechanical antiresonance, impedance goes to a maximum. Accompanying to this, a distinct phase shift for resonance and antiresonance is visible. For lower modes, there is a good correspondence between the measured and the analytical resonance frequencies. The experimental results show more modes in the same frequency region. Possibly this is due to solder affecting stiffness differently over the piezoelectric sensor. For higher modes, visible in the large piezoelectric sensor, there is a slight shift in resonance and antiresonance with respect to frequency. This may be attributed either to the solder, or to the modelling assumption of invariant excitation over the sensor thickness.

For the embedded piezoelectric sensors, the resonance behaviour is different from the freely vibrating piezoelectric sensors. For the small piezoelectric sensor, the behaviour seems to be strongly weakened, as noticed likewise by Dziendzikowski et al. (2016)[14]. Given phase angle $\theta$, it appears there is a movement in the resonance-antiresonance region from 250-350kHZ to 400-500kHz. This shift is echoed by the results of Qing et al. (2006)[63] and Schulze et al. (2014)[68] and can be related to the stiffness of the host material[2]. For the large embedded piezoelectric sensors, both the weakening effect as well as the phase shift effect are less pronounced compared to the small piezoelectric sensors for the fundamental mode.

As a response to:

> *How does embedding a sensor affect its electromechanical resonant behaviour compared to a non-embedded sensor?*

When the sensors were embedded, electromechanical resonant behaviour was observed at frequencies higher than for freely vibrating sensors. Also, the effect of resonance on the electrical impedance of the sensor was strongly weakened as compared to freely vibrating sensors.

## 4.4. Low-frequency excitation

Low-frequency bending tests have been performed as specified in section 3.5.1. First, the variation of responses between measurements and between piezoelectric sensors is discussed, followed by the

---

[2] Relative to host density.

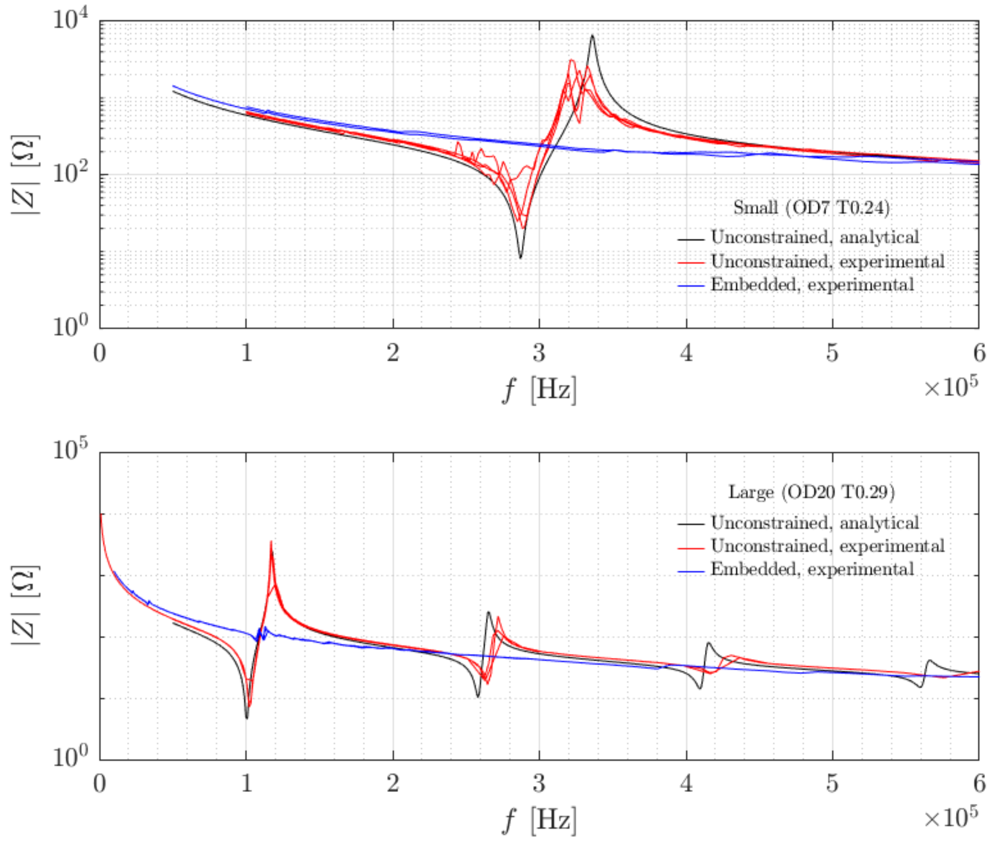

Figure 4.1: Electrical impedance absolute value $|Z|$ over excitation frequency.

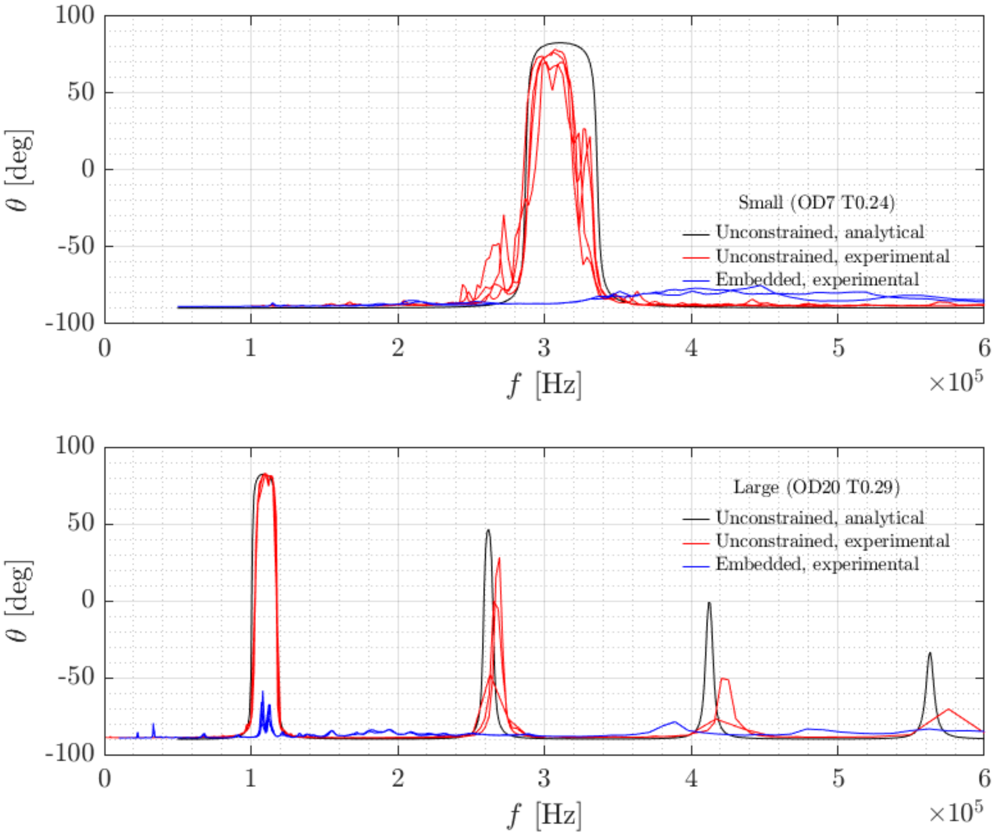

Figure 4.2: Electrical impedance phase angle $\theta$ over excitation frequency.

minimum frequency that can be measured by the set up. The comparison of data to modelling is made in section 5.2.

Examples of acquired data is given in fig. 4.3 for specimen 3L.

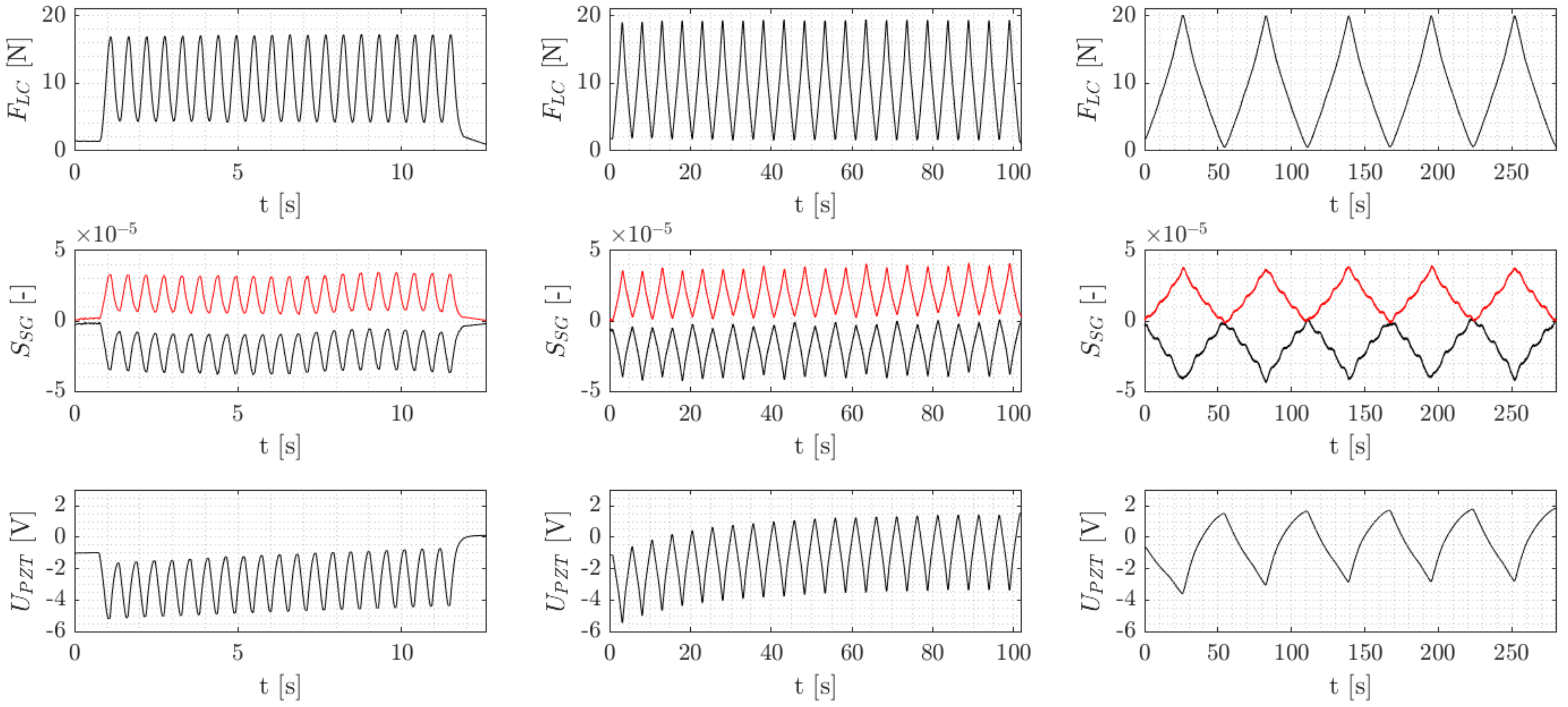

(a)

(b)

(c)

Figure 4.3: Load cell force $F_{LC}$, strain gauge strain $S_{SG}$ and piezoelectric sensor voltage $U_{PZT}$ of specimen 3L at $v_m = \{10, 1.0, 0.1\}$mm/min for (a), (b), (c), over time $t$. The black strain gauge output corresponds to the top strain gauge. The red strain gauge strain coincides with the bottom strain gauge.

From the plots, a few observations are made. All the data show an offset on the vertical axis. This is due to loading configuration, which may be seen as a superposition of a static load of and a dynamic load. For the higher velocity $v_m$=10mm/min, the machine load does not necessarily have the precise minimum and maximum as imposed beforehand. This implies the other data needs to be compensated for the varying load. Also, at lower velocities $v_m$=1 and 0.1mm/min, the strain gauge result seems to become unstable compared to the other outputs. Possibly this is due to the quarter bridge configuration[61]. Hence, values of the piezoelectric response are compared to load cell response and not not to strain gauge response as in [39, 69]. A linear relationship between applied force and strain is assumed.

With regard to the piezoelectric sensor response, three anomalies are noticed. First of all, the earlier described offset decreases over time. Secondly, for the lower velocities, the response is distorted to an asymmetric saw tooth shape. At last, for the bulk of the sensors, the response amplitude at $v_m$ =0.1mm/min, tends to be significantly lower than for the higher velocities. The above are all phenomena related to the finite resistance of the system. Following from modelling (section 2.3.3), the voltage drop due to discharge follows an exponential function over time, explaining the decreasing offset and the odd shape. As discharge is a continuous process, it hampers the total build up of voltage during a cycle, leading to a lower overall voltage amplitude.

To compare sensor responses, ratio $\frac{U_{PZT,a}}{F_{LC,a}}$ in V/N is introduced. This corrects for deviations of the load applied. Only peak-to-peak amplitudes are considered, as direct comparison of the full signals would give a biased view due to the distortion of the signal at the lower velocities. The values of $\frac{U_{PZT,a}}{F_{LC,a}}$ are recovered by means of a peak finding function.

Evolution of the ratio $\frac{U_{PZT,a}}{F_{LC,a}}$ in V/N is shown in the boxplot of fig. 4.4 for different head velocities and sensor number. The box describes the lower to upper quartile while whiskers extend to 1.5 times the inter quartile range as suggested in [12]. Remaining values are known as outliers, given in black dots. From the graphs, it becomes clear there is small variation in the sensor response over different cycles. The lowest velocity measurements are more prone to variation. Assuming a normal distribution, the coefficient of variation[3] is less than 7%, 6% and 14% at $v_m$ =10mm/min, 1.0mm/min, 0.1mm/min respectively for each sensor. Between sensors however there is more fluctuation. The coefficient of variation of all sensors of one type collectively is 25%, 21%, 42% for small sensors and 14%, 14%, 19% for large sensors. This variation can be attributed to sensor placement in the host material. The sensor can be located somewhat higher or lower in the thickness direction. Tilting of the sensor is possible as well. Furthermore, the glass-epoxy insulation has a slight variation of shape over different sensors. By improvement of manufacturing quality, the effect of these causes can be limited. Also, resistances can vary due to slight differences in manufacture.

### 4.4.1. Conclusion

Measurement results with embedded piezoelectric sensors for low frequency excitation were presented.

Two research subquestions can be addressed:

> *Given the measurement set-up, what is the minimum frequency the piezoelectric sensor can measure strain accurately?*

The sensor captured loads having a frequency as low as $\approx 0.018$Hz. Below ≈1.8Hz, the result became distorted due to electrical discharge. Using a different set-up with higher impedance materials can lead to an improvement in this aspect.

> *What is the variation of responses between measurements and between sensors?*

In the conducted low-frequency bending experiments, the variation of responses between cycli is lower than 7%, 6% and 14% at $v_m$ = 1.8Hz, 0.18Hz and 0.018Hz for each sensor. Between different sensors the coefficient of variation turned out to be 25%, 21%, 42% for small sensors and 14%, 14%, 19%

---

[3] This measure allows for comparison between different sensor types.

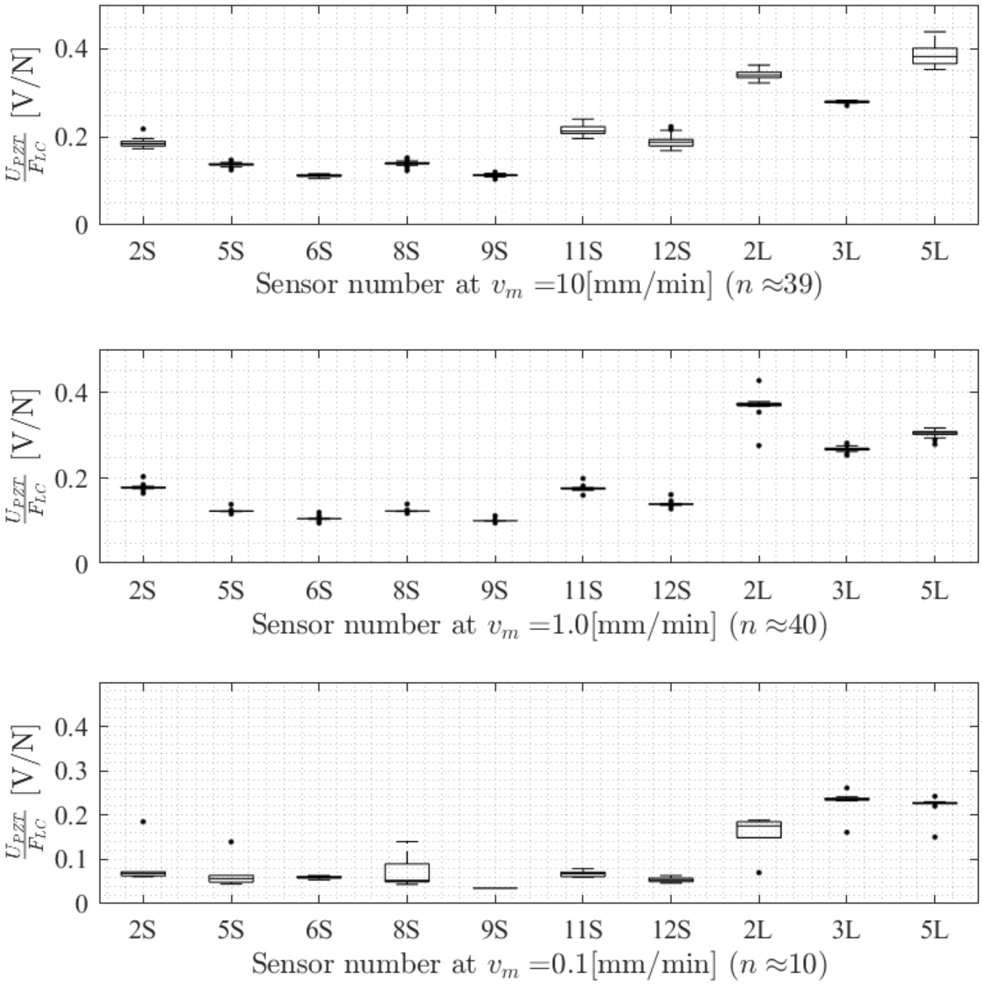

Figure 4.4: Box plot of $\frac{U_{PZT,a}}{F_{LC,a}}$ for all functional small ('S') and large ('L') sensors. $n$ stands for the number of data points for each sensor, and is slightly different per sensor.

for large sensors. It is considered that by improving the embedding process these variations can be lowered.

## 4.5. Specimen flexural properties

Specimen flexural strength tests are carried out through section 3.5.2. Regarding the results, first a dilatation is given on the found failure modes. This is followed by the force-displacement results and by values derived from force-displacement, such as flexural stiffness, maximum strain, maximum load and fracture toughness.

### 4.5.1. Failure mechanisms

During the failure tests, a few phenomena related to specimen damage and failure were captured. First, between $F_{LC}$ = 6000N and 7000N, parts of the upper lamina failed in compression. This manifested itself through fibre matrix debonding and fibre fracture near the tabs. In the mentioned load range, this did not lead directly to gross failure.

Above $F_{LC}$ =7000N, in specimens without sensors (N), the compressive failure gradually extended to approximately the upper four laminae and lead to gross failure in one specimen. In these specimens, the location of compressive rupture was near the load tabs. For three out of four specimens, sudden gross tensile failure occurred (fig. 4.5). Tensile rupture was between 8mm and 21mm from the centreline.

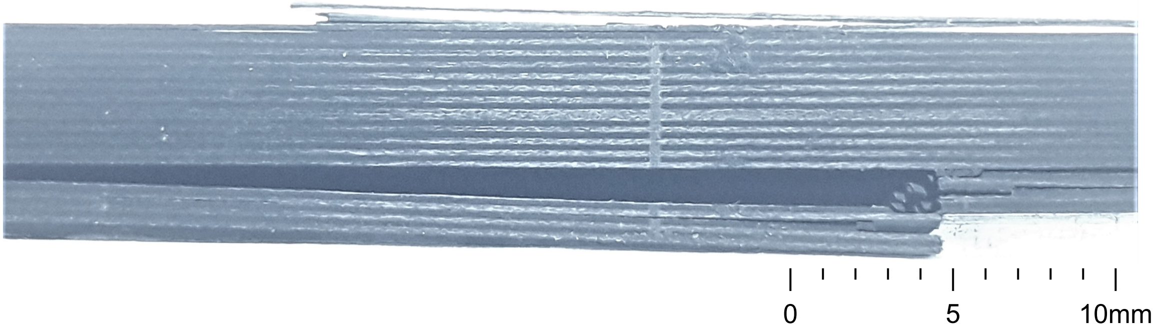

Figure 4.5: Thickness view of specimen 4N. On the top side of the specimen, superficial compressive failure is visible. Tensile rupture can be seen on the bottom of the specimen. The centreline of the specimen is indicated by the light-coloured vertical line.

For the specimens with sensors on the compression side (S and L), the superficial compressive failure extended to the laminae that had a cut-out for the sensor. In three out of four specimens with sensors in compression, the location of rupture was near the interface between the sensor and glass fibre, as given in fig. 4.6. In the fourth case, the rupture was about in the middle of the specimen.

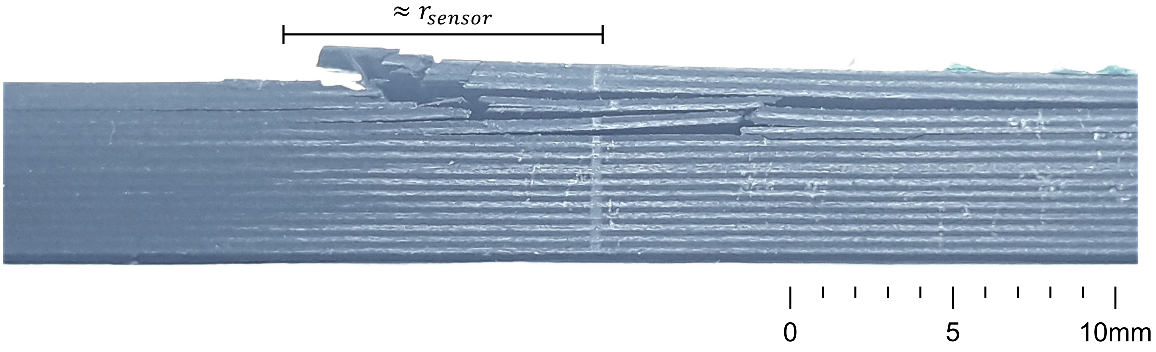

Figure 4.6: Thickness view of specimen 2L. On the top side of the specimen, extensive compressive failure is visible.

The observed local compressive failure did not develop beyond the upper two laminae for the specimens with sensors on the tension side (S (T)). In these specimens, abrupt gross failure on the tension side occurred, as can be seen in fig. 4.7. The rupture was 4.5mm to 8mm away from the centreline. This corresponds to the location of glass fibre insulation.

Given the above descriptions, it is clear the type of failure that occurs is determined by the sensor embedment details, either through rupture at the sensor, or at the glass-epoxy insulation. In the next sections, ultimate load, ultimate strain and fracture toughness are derived from failure. It is considered that any deviation in the value of these parameters from baseline (N) specimens is due to the specific type of failure and not due to inherent variation in host material properties.

### 4.5.2. Force-displacement

A force-displacement plot of the described failure tests is given in fig. 4.8.

In the plot, the force is load cell output $F_{LC}$ and the displacement $w_m$ refers to the motion of the machine

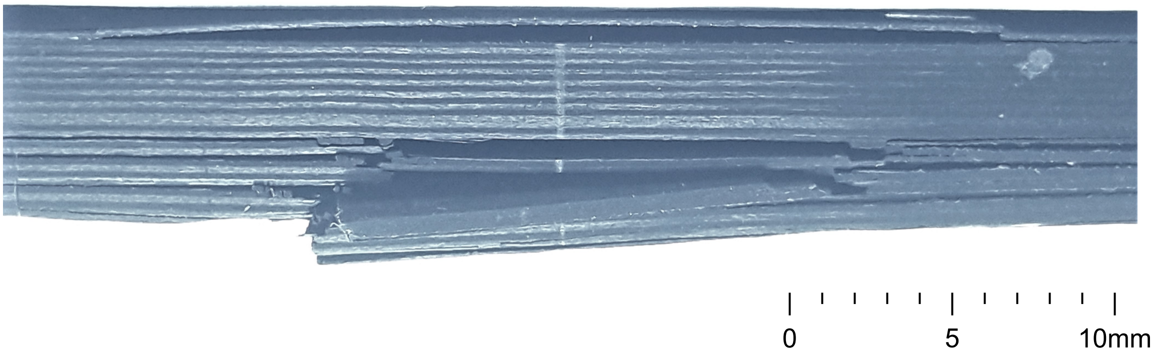

Figure 4.7: Thickness view of specimen 5S. On the top of the specimen, superficial compressive failure is visible. Tensile rupture can be seen on the bottom of the specimen.

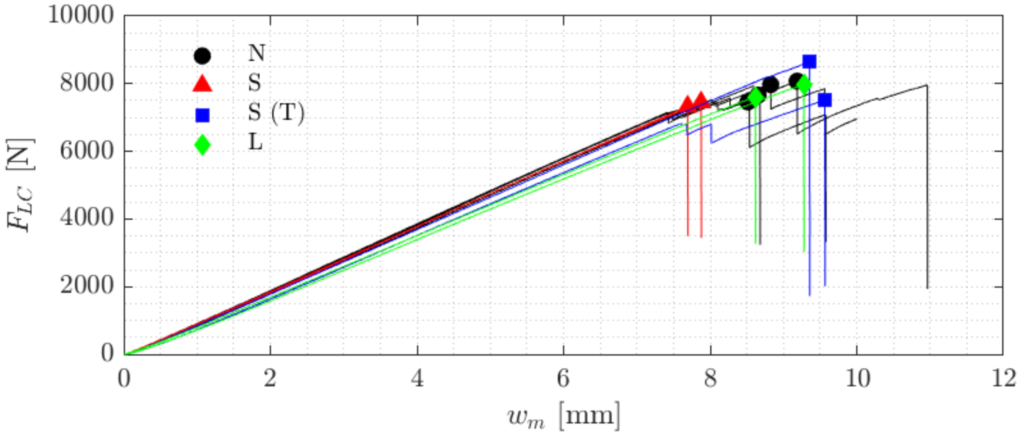

Figure 4.8: Force-displacement graph of tested specimens. Markers indicate the maximum applied force per specimen.

crosshead. The jagged lines in fig. 4.8 show a stiffness drop due to local compressive failure, which was not severe enough to be considered gross or final failure. It appears that baseline N specimens, without sensor, and S (T) specimens, with sensors on the tension side, can take a large amount of these local strength drops, compared to S and L sensors, that tend to show little recovery after local compressive failure. It is interesting to note the L specimens can take a larger deflection compared to the S specimens. From above plot, ultimate strain, ultimate load, toughness, as well as flexural stiffness can be determined[4].

### 4.5.3. Flexural Stiffness

Flexural stiffness $E$ is determined for each tested specimen with two methods, (i) using load cell and crosshead displacement according to ASTM-D6272[10], and (ii) using load cell and strain gauge measurements. The former method makes use of:

$$E_{CH} = 0.21 L^3 \frac{m}{bd^3}. \tag{4.1}$$

The flexural stiffness is given by $E_{CH}$, $L$ denotes the support span in mm, $b$ specimen width in mm and $d$ specimen thickness in mm. Here, force-displacement slope $m$ is determined through a least squares approach. The latter method makes use of Euler-Bernoulli beam theory[5], resulting in

---

[4] Both mean values and actual values per specimen are given. Standard deviation is only calculated for N specimens, due to the relatively low sample size of the other types, id est four samples for N specimens, and two for the other types.

$$E_{SG} = \frac{1}{12}\frac{Ld}{I}\frac{1}{n}\sum_{i=1}^{n}\frac{F_{LC_i}}{\overline{S_{SG_i}}}. \tag{4.2}$$

In this equation, strain gauge response $\overline{S_{SG}}$ is averaged over the absolute value of the top and bottom strain gauge strains. $I$ equals the applicable moment of inertia, whereas $n$ is the number of data points used. The flexural stiffness is representative for the global beam, not for individual laminae. Stiffness $E$ instead of flexural rigidity $EI$ is compared to account for thickness variations between specimens. The initial data with a load range of 0 to 200 N was not used due to a toe region. The values used are based on the $F_{LC}$ =1000N to 5000N region of the failure test. Note that the aluminium tabs can influence the data. However, it is assumed the influence of this is similar over the specimens. The results for $E_{CH}$ and $E_{LC}$ are given in terms of mean $\mu$ and standard deviation $\sigma$ in tables 4.2 and 4.6.

| Specimen type | $E_{CH}$ [×10$^9$N/m$^2$] | | $E_{SG}$ [×10$^9$N/m$^2$] | |
|---|---|---|---|---|
| | $\mu$ | $\sigma$ | $\mu$ | $\sigma$ |
| Analytical | 79.3 | | | |
| N | 82.6 | 4.03 | 80.1 | 0.630 |
| S | 77.2 | | 79.2 | |
| S (T) | 77.2 | | 75.6 | |
| L | 73.4 | | 78.1 | |

Table 4.2: Mean $\mu$ and standard deviation $\sigma$ of corrected flexural stiffness $E_{CH}$ and $E_{SG}$, from the method described in [10] and the strain gauge response respectively.

In the table, an analytical value for the stiffness, based on prepreg material data [24], is given for reference. Through either method, it is clear baseline N specimens tend to have a somewhat higher stiffness (3 to 8% on average) compared to embedded specimens. A decrease in flexural stiffness is expected through the lower elastic modulus of glass-epoxy and PZT. Given the variation in data, a part of the discrepancy may also be attributed to the small sample size.

### 4.5.4. Ultimate strain

Strain can be determined in accordance with ASTM-D6272[10]:

$$S_{CH} = 4.70 w_{L/2}\frac{d}{L^2}. \tag{4.3}$$

Deflection at the centre $w_{L/2}$ is estimated to be $w_{L/2} = 1.15 w_m$. Also, strains measured by the strain gauges can be taken into account. The results for the ultimate strain are given in tables 4.3 and 4.6.

| Specimen type | $S_{CH}$ [×10$^{-2}$] | | $S_{SG,max}$ [×10$^{-2}$] | |
|---|---|---|---|---|
| | $\mu$ | $\sigma$ | $\mu$ | $\sigma$ |
| Analytical | 1.58 | | | |
| N | 2.03 | 0.205 | 1.58 | 0.146 |
| S | 1.60 | | 1.46 | |
| S (T) | 1.94 | | 1.68 | |
| L | 1.82 | | 1.62 | |

Table 4.3: Mean $\mu$ and standard deviation $\sigma$ of maximum strain $S_{CH}$ and $S_{SG}$, from the method described in [10] and the strain gauge response respectively.

The analytical value given in the table is based on outer fibre 0°tensile failure. Maximum strain $S_{SG,max}$ is the maximum absolute value retrieved from both top and bottom strain gauges, to circumvent the issue of broken strain gauges due to local specimen damage. In both methods, the trend is similar,

---

[5] This is considered applicable, given the beams' aspect ratio and material shear stiffness.

N, S (T), and L specimens have a relatively high value compared to S specimens. The strain drop calculated for S specimens compared to N specimens is between 8 and 21%. It is interesting to note, when comparing L to S specimens, having a larger sensor embedded does not seem to imply a lower maximum strain can be achieved. This effect is contradictory to [47], who placed the sensors on the neutral axis. Possibly, the discrepancy is due to the sensor being fully in compression in this research. The compression strength is large compared to tension strength in PZT[65]. Also the larger sensor might inhibit local fibre buckling and stress concentrations at material interfaces are spread over a larger distance compared to a small sensor. A strain drop between 0 and 10% is measured when comparing L specimens with N specimens. The maximum strain of S (T) specimens comes nearer to the pristine (N) value. Having a sensor on the tension side results in a failure type which more resembles pristine failure. This is due to the lack of disturbances on the compressive side of the specimen.

### 4.5.5. Maximum corrected load

Load $F_{LC}$ is corrected to an equivalent stress[6] using eq. (4.4), to account for thickness variations between specimens. Obtained results for the maximum value are given in tables 4.4 and 4.6. From the table, it appears that maximum loads are more or less similar throughout the specimen types, with a slight dip for the S-specimens, accounting for a 5% decline. This can be correlated to the maximum strain, which is also slightly less than with the other specimens.

$$T_{LC} = \frac{F_{LC}L}{bd^2} \tag{4.4}$$

| Specimen type | $T_{LC}$ [×10$^9$ N/m$^2$] | |
|---|---|---|
| | $\mu$ | $\sigma$ |
| Analytical | 1.25 | |
| N | 1.14 | 0.0401 |
| S | 1.09 | |
| S (T) | 1.20 | |
| L | 1.18 | |

Table 4.4: Mean $\mu$ and standard deviation $\sigma$ of maximum corrected load $T_{LC}$.

### 4.5.6. Toughness

Integrating equivalent stress $T_{LC}$ over strain $S_{CH}$, it is possible to retrieve a toughness $W_{LC}$ for the specimens. Resulting data may be seen in tables 4.5 and 4.6.

A relatively large (34%) reduction in toughness can be seen comparing S specimens to N specimens. A decrease is visible as well for the L (19%) and S (T) (8%) specimens, albeit less profound.

### 4.5.7. Conclusions

Based on above data, conclusions with regard to the research-subquestion can be drawn:

> *To what extend are flexural mechanical properties of the composite host material influenced by embedding a piezoelectric sensor?*

Given the presented results in this section, preliminary conclusions can be made. The stiffness of specimens with sensors embedded tends to be, depending on the method, on average 3 to 8% lower than baseline specimens. In S specimens there is a noticeable decrease in maximum strain (8 to 21%), load (5%) and fracture toughness (34%). This decrease is less pronounced or invisible for L specimens, being 0 to 10% in ultimate strain, 4% in ultimate load and 19% in toughness on average. In S (T) specimens, with the sensor on the tension side, ultimate strain compared to baseline N specimens

---

[6] This stress is not representative for the actual stress experienced by the laminae.

| Specimen type | $W_{LC}$ [×$10^6$ N/m$^2$] | |
|---|---|---|
| | $\mu$ | $\sigma$ |
| N | 13.2 | 2.14 |
| S | 8.72 | |
| S (T) | 12.1 | |
| L | 10.7 | |

Table 4.5: Mean $\mu$ and standard deviation $\sigma$ of $W_{LC}$.

| Specimen nr. | 1N | 2N | 4N | 7N | 2S | 9S | 4S(T) | 5S(T) | 2L | 3L |
|---|---|---|---|---|---|---|---|---|---|---|
| $E_{CH}$ [×$10^9$N/m$^2$] | 84.7 | 78.2 | 80.5 | 87.1 | 76.1 | 78.2 | 74.0 | 80.5 | 74.8 | 72.1 |
| $E_{SG}$ [×$10^9$N/m$^2$] | 80.7 | 80.1 | 80.5 | 79.3 | 77.8 | 80.5 | 76.8 | 74.4 | 76.6 | 79.6 |
| $S_{CH,max}$ [×$10^{-2}$] | 2.05 | 2.29 | 1.80 | 1.98 | 1.63 | 1.58 | 1.92 | 1.96 | 1.75 | 1.89 |
| $S_{SG,max}$ [×$10^{-2}$] | 1.61 | 1.77 | 1.43 | 1.52 | 1.49 | 1.44 | 1.71 | 1.65 | 1.54 | 1.69 |
| $T_{LC}$ [×$10^9$N/m$^2$] | 1.19 | 1.16 | 1.12 | 1.10 | 1.10 | 1.09 | 1.28 | 1.12 | 1.16 | 1.21 |
| $W_{LC}$ [×$10^6$N/m$^2$] | 13.7 | 15.9 | 10.8 | 12.5 | 8.92 | 8.52 | 12.4 | 11.9 | 10.1 | 11.3 |

Table 4.6: Stiffness, ultimate strain, ultimate load and toughness results per specimen.

had, depending on the method an average, a drop less than 4%. Ultimate load and toughness on average had a maximum drop of 8%.

## 4.6. Specimen failure and elastic waves

Following the description of the test in section 3.5.3 and the assessment of section 4.2, results can be presented and analysed for specimen 3L. To discriminate between noise and failure-related guided waves, a signal is regarded the latter when it is captured by at least two sensors within 10$\mu$s arrival time difference. For specimen 3L, 82 emission signals are identified by embedded sensor 3L and commercial sensor R15I-AST 1, 93 by 3L and R15I-AST 2, and 830 by R15I-AST 1 and R15I-AST 2. Signals that are captured by 3L and R15I-AST 1 and R15I-AST 2 are 71 in number. Note, in total during loading and until failure of the specimen, 3L and the commercial sensors caught 4150, 3657 and 5900 individual signals.

First individual signals are discussed. This is followed by an assessment of the maximum amplitude and hit rate of the signals. Based on the acquired signals, a signal-to-noise ratio is defined.

Signals that are captured by all three sensors, at different times during the loading of specimen 3L, are given in figs. 4.9 to 4.12. The time in the plot is relative to the earliest measurement of the hit. The signals are corrected for their received pre-amplification. Also, signals from embedded sensor 3L and commercial sensor R15I-AST 1 are offset for the sake of visibility. It can be seen both the embedded and the commercial sensors capture hits clearly throughout the loading up to failure, hinting there is no gross degradation of the embedded sensor up to the failure strain of 8.45 to 9.45m$\varepsilon$. Also, the embedded sensor responses show a wider variety in frequencies compared to the commercial sensor. The latter figure, fig. 4.12, gives a signal that is clipped by the AMSY6 system.

To gain knowledge on temporal variations of the emissions and the sensor response, maximum amplitudes of signals can be retrieved and plotted over time. In fig. 4.13, amplitudes in dB[7] are given for the signals detected by the embedded sensor (3L) and at least either one of the commercial sensors. For reference, the loading sequence $F_{LC}$ is given as well. In general, the response of the embedded sensor tends to be higher than the related response of the commercial sensor. Also, between $t$= 550s and 670s, a number of signals have reached the upper threshold of the system. No clear relationship between amplitude and load is observed. This may be attributed to aforementioned clipping. Amplitudes of signals that are captured by at least both commercial sensors are given in fig. 4.14. The data suggests a linear relation between maximum amplitude measured and the loading of the specimen.

---

[7] Relative to 1$\mu$V, the standard of the AMSY6 data acquisition machine.

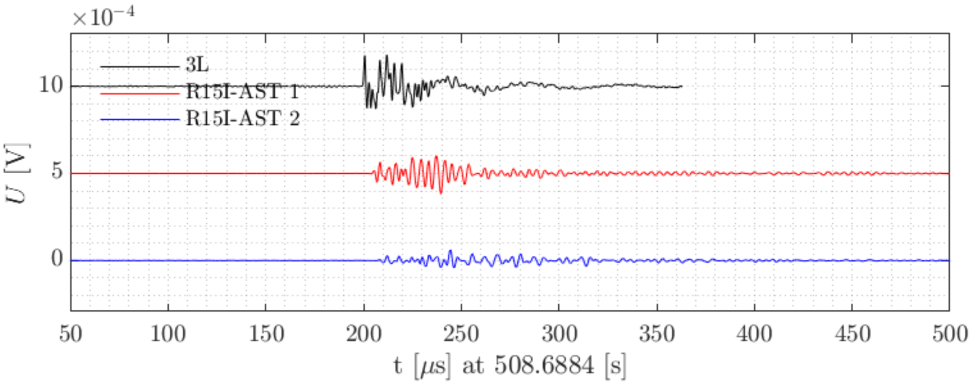

Figure 4.9: Signal captured by all three sensors at time $t$= 509s.

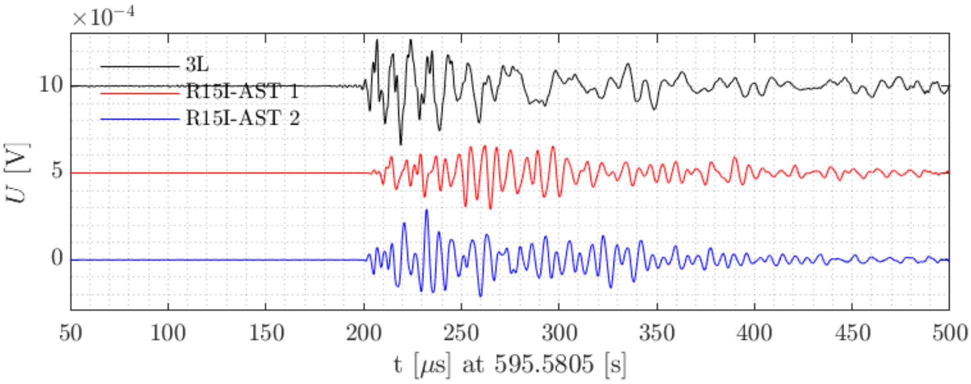

Figure 4.10: Signal captured by all three sensors at time $t$= 596s.

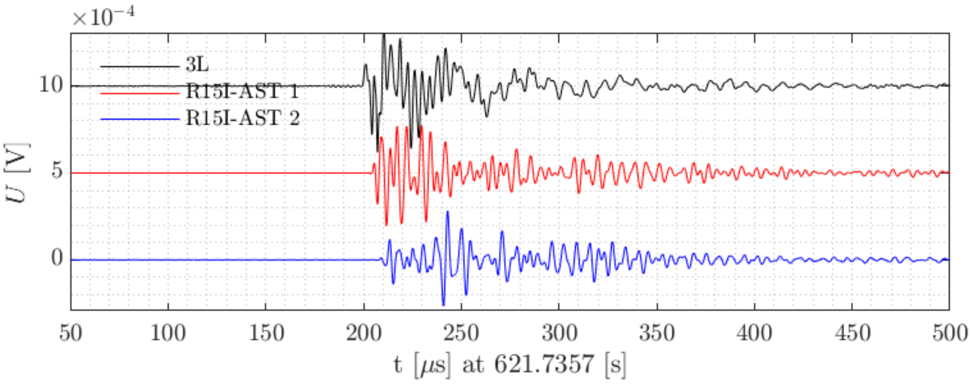

Figure 4.11: Signal captured by all three sensors at time $t$= 622s.

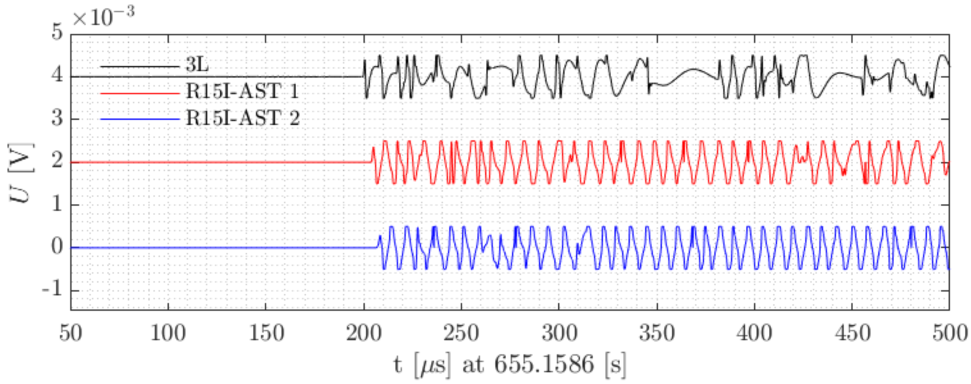

Figure 4.12: Signal captured by all three sensors at time $t$= 655s. Note the different scale on the vertical axis.

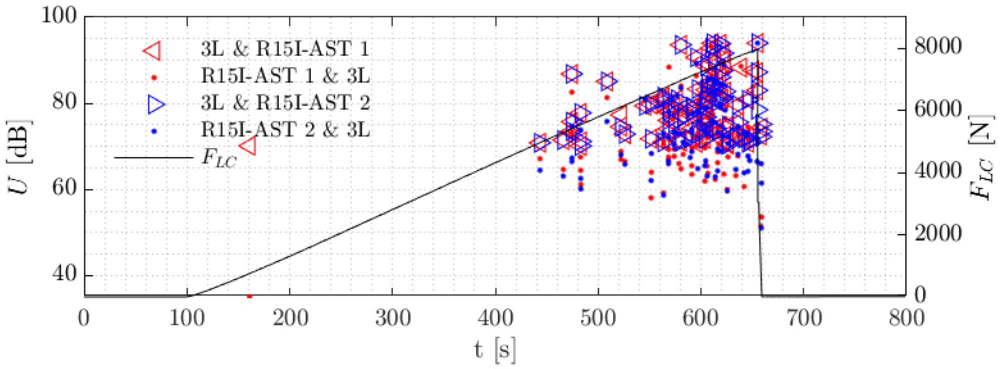

Figure 4.13: Maximum amplitude in dB of a signal captured by both the embedded sensor (3L) and either one of the commercial sensors (R15I-AST). Triangular data represent the signal captured by the embedded sensor, whereas dots refer to the corresponding signal of either one of the commercial sensors. Machine load $F_{LC}$ over time is given for reference.

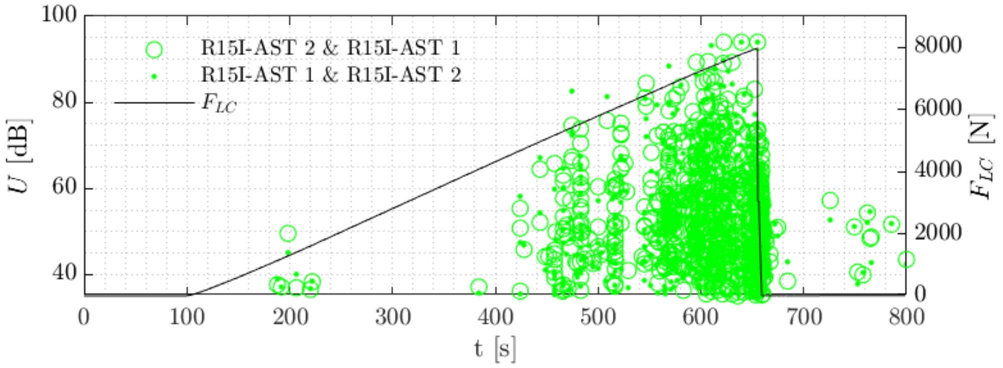

Figure 4.14: Maximum amplitude of a signal captured by both of the commercial sensors (R15I-AST). Machine load $F_{LC}$ over time is given for reference.

From figs. 4.13 and 4.14, certain points in time show a higher density of hits than other times. To further investigate this, the data is processed to a hit-rate plot. Given the number of signals (hits) captured, a hit rate can be formed. Using a moving window for every second the amount of hits from 5 seconds before to 5 seconds after is accumulated for calculation of the hitrate, resulting in the plots given in figs. 4.15 and 4.16.

The trend of signals detected by the embedded sensor closely matches the trend of signals captured by the commercial sensors upto around $F_{LC}$ = 7500N. After that, the commercial sensor hit rate increase is not followed by the embedded sensor hit rate. This possibly indicates depolarisation or partial failure of the sensor.

When observing the transient responses of figs. 4.9 to 4.12, it is noticeable that at the first 200$\mu$s, the pretrigger time, a slighlty varying amount of noise is visible. This can be quantified by defining a signal to noise ratio (SNR).

$$SNR = 10\log_{10}\frac{P_{signal}}{P_{pretrigger}} = 10\log_{10}\frac{\sum_{t=n+1}^{o} U_t^2}{\sum_{t=m}^{n} U_t^2}. \tag{4.5}$$

Here $P_{signal}$ and $P_{pretrigger}$ represent powers associated with the measured signal (after the pretrigger time) and the pretrigger (noisy) measurement. In practice, these powers are retrieved by summing the squared of the signal over discrete nondimensional time steps $t$=m to $n$ for the pretrigger signal and $t$=$n+1$ to $o$ for the signal of interest [49]. The first 200$\mu$s correspond to the pretrigger time. Where possible, an equal amount of time, from 200 to 400$\mu$s, is used to represent the signal. If the recorded signal turned out to be smaller, the pretrigger period was decreased likewise.

To investigate the effect of the load on the SNR, a plot is made showing the SNR's over time, divided

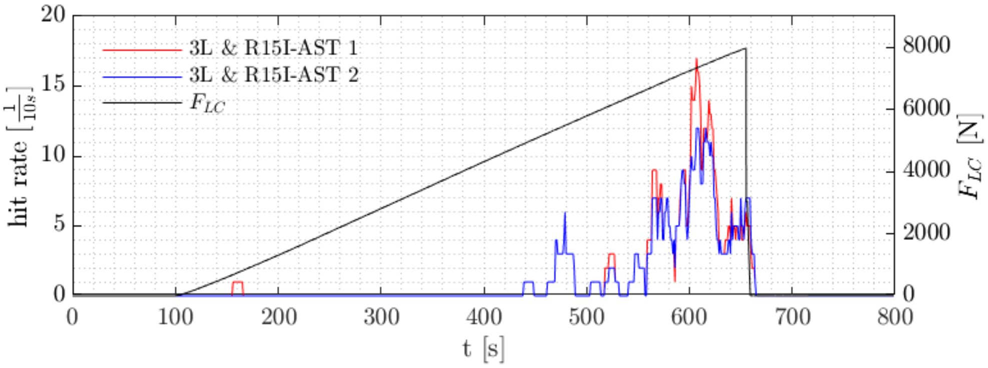

Figure 4.15: Hit rate over time for signals that were captured by both the embedded sensor (3L) and one of the commercial sensors (R15I-AST). Machine load $F_{LC}$ over time is given for reference.

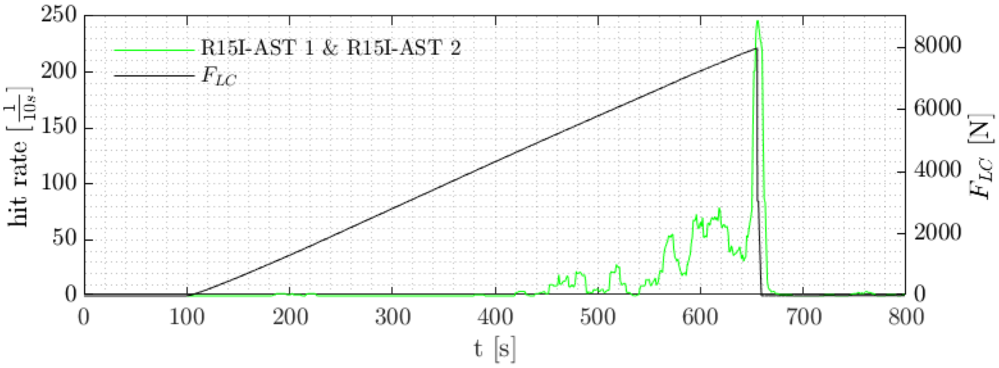

Figure 4.16: Hit rate over time for signals that were captured by both commercial sensors (R15I-AST). Machine load $F_{LC}$ over time is given for reference.

over different sensors. This leads to figs. 4.17 and 4.18.

No clear drop in SNR of the embedded sensors over time as observed in hit rate (fig. 4.15) is noticed, indicating that possible partial sensor failure might not significantly impede signal quality. The data in the figures can be related to figs. 4.13 and 4.14, assuming a constant noise amplitude. It is interesting to note that when comparing fig. 4.17 to fig. 4.13 the embedded sensor response has, relative to the commercial sensor response, a high amplitude but a low signal-to-noise-ratio. This can be attributed to the relatively long wiring between the sensor and the preamplifier, and the large gain in the preamplifier.

A boxplot (fig. 4.19) shows the overall SNR of the signals captured. The boxplot confirms earlier statements, with medians of embedded sensor responses being around 17dB and corresponding commercial sensor responses at 42dB. Responses that are captured by both commercial sensors have a lower median, 22dB. The latter may be due to the difference in threshold, 35dB for commercial sensors versus 70dB for the embedded sensor. In other words, signals with a low SNR are likely to have a low amplitude, leading that they are not captured by the embedded sensor, because of this lower threshold. Another reasoning would be the choice in wiring the embedded sensor, bifilar instead of coaxial, which possibly increases noise. In future research, by improving the manufacturing procedure, an improvement in SNR may be expected.

### 4.6.1. Conclusion

The data evaluated above may be used to generate a conclusion regarding research subquestion:

> *To what extent in terms of signal quality and maximum strain is the embedded sensor able to measure damage-related guided elastic waves?*

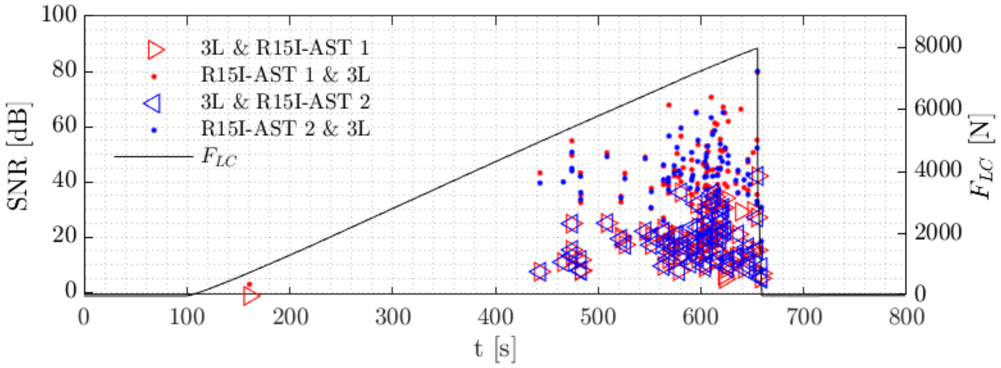

Figure 4.17: Signal to noise ratio SNR over time for signals that were captured by both the embedded sensor (3L, triangles) and one of the commercial sensors (R15I-AST, dots). Machine load $F_{LC}$ over time is given for reference.

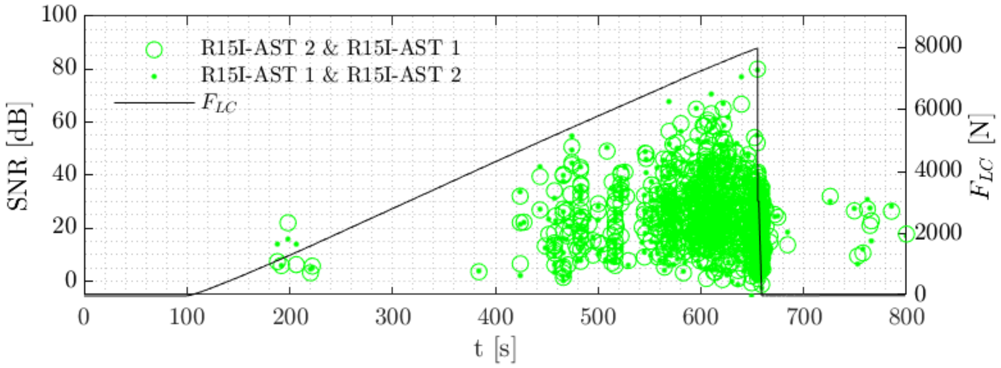

Figure 4.18: Signal to noise ratio SNR over time for signals that were captured by both commercial sensors (R15I-AST). Machine load $F_{LC}$ over time is given for reference.

From sensor 3L, signals emitted by damage growth were obtained up to the point of failure, with a local compressive strain of $S_{CH}$ ≈8.45 to 9.45m$\varepsilon$. Signal quality is assessed by means of a signal-to-noise ratio, showing a median value of 17dB. This turned out to be sufficient for identifying damage-related emissions.

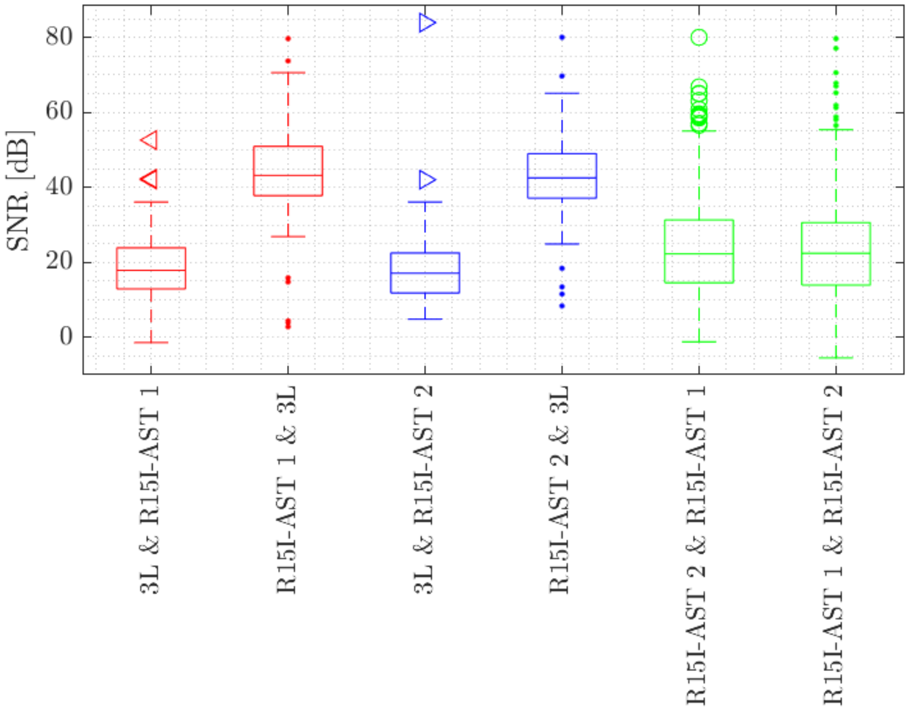

Figure 4.19: Boxplot of SNR in dB. Measurements are compared between embedded sensor 3L and commercial sensors R15I-AST 1 and R15I-AST 2.

# 5

# Simulation

## 5.1. Introduction

Following the modelling method given in chapter 2 and the experimental results from section 4.4, a validation study is performed. The modelling allows a parametric study on the sensitivity of the embedded sensors in measuring elastic wave emissions.

> *How is the agreement between modelled and measured sensor responses?*
>
> *How does the location and size of the sensor influence elastic wave measurements?*

First, a validation of the electromechanical modelling is given by means of modelling the cyclic bending test and comparing results from the modelling to those of the experiment. Secondly, based on electromechanical as well as elastic wave modelling, a parametric study is performed.

## 5.2. Validation of electromechanical transfer function

### 5.2.1. Introduction

In chapter 2 a verified formulation is presented for determining sensor voltage output from an imposed strain field. In chapter 4 measured data is acquired, which allows validation of this method. First the mechanical strain field experienced by the sensor is retrieved. The strain field retrieved then serves as input for the transfer to voltage. The voltages retrieved include effects regarding the resistance of the system.

### 5.2.2. Retrieving sensor strain field

The data to be considered is based on the cyclic four point bending tests (maximum load $F_{LC}$=20N) as discussed in section 2.3.1. A strain field containing the full strain tensor is retrieved through a mechanical finite element model[1] (FEM) of which the results are given in figs. 5.1a and 5.1b. In this model a quarter of the full specimen is generated with three-dimensional solid elements. Each lamina of the composite is represented by an individual layer of elements. Glass-fibre insulation surrounding the sensor as well neat resin between the insulation and the carbon fibre laminae are modelled. Material parameters are given by Hexcel corporation [24], Huntsman [25] and Meggit [50]. For strains in longitudinal direction averaged over the sensor electrode area, values are given in section 5.2.2. The values are based on the strain gauge results and the thickness location of the piezoelectric sensor, an Euler-Bernoulli beam model, and from the described finite element model. From the table, it is apparent that values from the finite element strain field are lower than measurement results. This can be attributed to the glass-epoxy and epoxy surrounding the sensor. These materials have a low stiffness compared

---

[1] Created in ANSYS by mr. X. Zhang MSc.

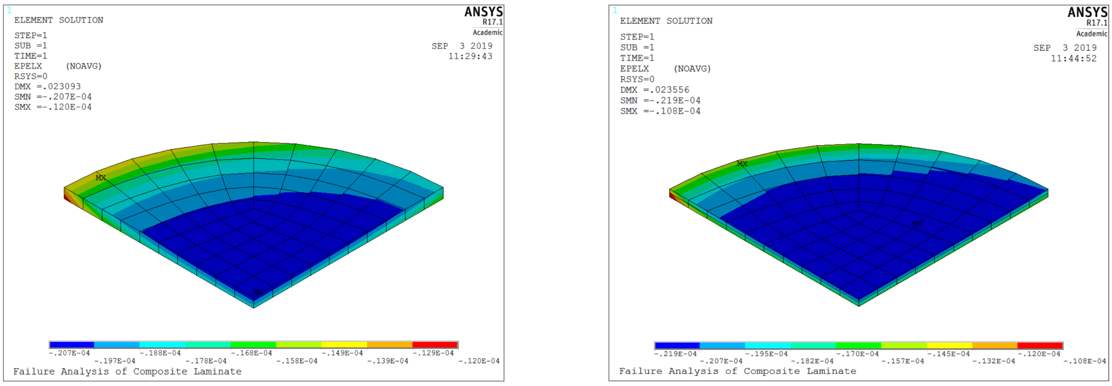

(a) (b)

Figure 5.1: Sensor strain distribution $S_{11}$ as determined through finite element modelling during low-frequency bending. (a) and (b) give the result for the small and large sensor respectively.

to sensor and host material, leading to a relieve of the sensor. Visually, the distribution of strain can be compared to Shin et al. [69]. In further calculations, it is assumed strains scale linearly with machine load $F_{LC}$.

| | strain gauges | Euler-Bernoulli | FEM large sensor | FEM small sensor |
|---|---|---|---|---|
| $S_{11,AV}$ [$\times 10^{-6}$] | $\approx 20$ | 19.5 | 16.72 | 16.52 |

Table 5.1: Averaged strain in longitudinal direction $S_{11,AV}$, measured in the experiments and calculated through beam theory and FE.

### 5.2.3. Strain to voltage transfer

To calculate voltages, eq. (2.20) is evaluated numerically in the time domain. Electrical resistances that occur in the specimen design are based on table 5.2. Contents of the piezoelectric matrices are given by Rupitsch (2019)[66] and individual piezoelectric constants by Ferroperm (2017)[50].

### 5.2.4. Results

In figs. 5.2 and 5.3 is a comparison of the measured voltage and calculated voltage, based on a similar loading. The resistance of $R_m = 3\times 10^9 \Omega$is used as an example. The simulation captures the effects of sensor discharge, visible in the decreasing bias, and the lower amplitude and deformation at the low 0.1mm/min velocity. It is noted that the amplitude of the simulated voltage response is 40 per cent lower than the measured response for the small sensor. For the larger sensors, that value is 65%. This is possibly due to variations material properties, such as sensor thickness or piezoelectric constants[6] and details of the surroundings of the sensor in the experiments.

To get a grasp of the effect at different frequencies for different resistances, figs. 5.4 and 5.5 compares experimental data in the boxplots with simulated results assuming resistances from $10^8 \Omega$to $10^{10} \Omega$. Given the figures it is clear the voltage amplitude drop in the simulation for higher frequencies cannot be attributed to the assumed resistance.

---

[2] Based on volume resistivity and geometry.

[3] See footnote 2.

[4] See footnote 2.

[5] Values for the resistivity of polyurethane are widely varying, and the resulting resistance might be as high as $10^{12}$ $\Omega$.

[6] The latter was not observed during verification, possibly due to the sparseness of the piezoelectric matrices in the reference material. However, in this example, more terms are used, resulting in fuller matrices.

| system | type | resistance [$\Omega$] |
|---|---|---|
| sensor | PZ27[2] | $> 10^9$ [51] |
| surrounding material | glass fiber-epoxy | $> 10^{12}$ [19] |
| | kapton tape[3] | $> 10^{15}$ [13] |
| wiring insulation | polyurethane[4] [5] | $> 10^8$ [18], [62], [17] |
| | PTFE (teflon) | $> 10^{15}$ [19] |
| measurement system | NI usb 6002 | $> 10^9$ [53] |
| | NI 6229 | $> 10^{10}$ [54] |
| | AEP5H | $5 \times 10^7$ [72] |

Table 5.2: Resistances encountered in the experiments.

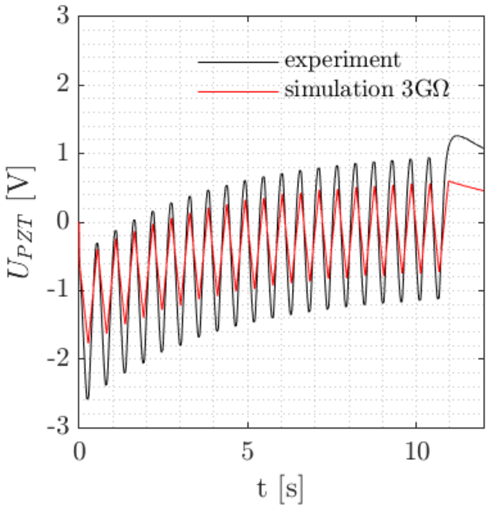

Figure 5.2: Response of sensor 11S on excitation with a $v_m$ =10mm/min. The simulated response is given in red.

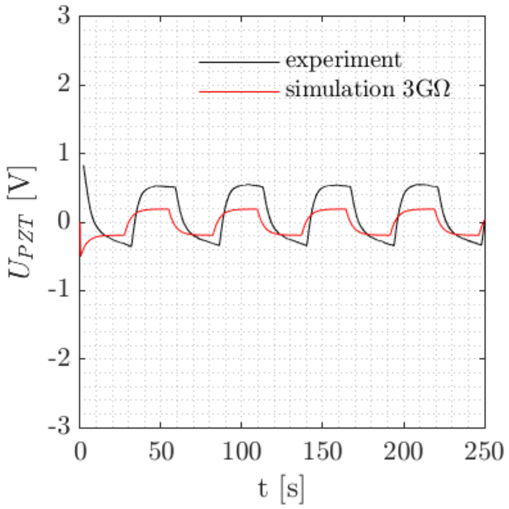

Figure 5.3: Response of sensor 11S on excitation with a $v_m$ =0.1mm/min. The simulated response is given in red.

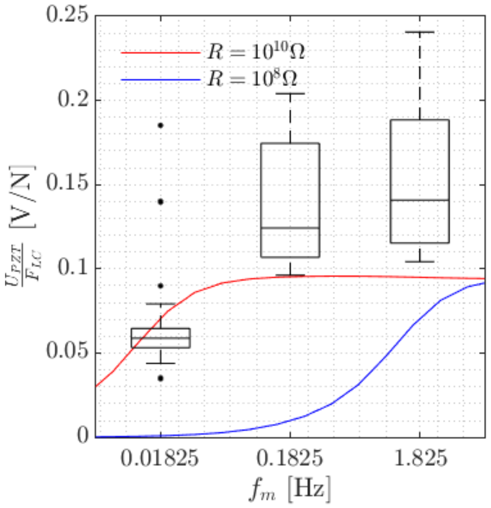

Figure 5.4: Box plot of measured $\frac{U_{PZT,a}}{F_{LC,a}}$ for small sensors in combination with the simulated results at $R_m$=$10^8\Omega$and $10^{10}\Omega$.

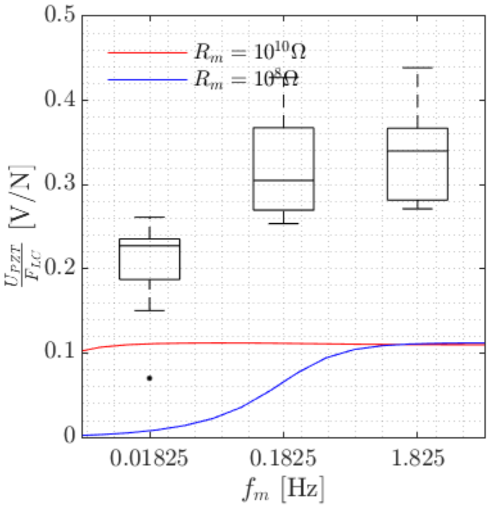

Figure 5.5: Box plot of measured $\frac{U_{PZT,a}}{F_{LC,a}}$ for large sensors in combination with the simulated results at $R_m$=$10^8\Omega$and $10^{10}\Omega$.

### 5.2.5. Conclusions

A study regarding the validation of the electromechanical modelling provided in chapter 2 is carried out. Measurement results from a low-frequency flexural excitation are compared to their simulated counterpart using finite element modelling results and electromechanical modelling. The research is affiliated with research subquestion:

> *To what extend does modelling cover real sensor measurements?*

It has been shown that the performed modelling captures the effects related to sensor discharge at low frequencies. However modelled response amplitudes are 40% to 65% lower than measured response amplitudes for small (7mm diameter) and large sensors (20mm diameter) respectively.

## 5.3. Modelling of guided elastic waves and related sensor response

### 5.3.1. Introduction

Next to the low-frequency cyclic bending tests that are modelled in section 5.2, it is of interest to model a situation similar to the pencil lead break experiments of section 3.3. First a description of the used model is given, followed by a mesh convergence study. At last, an analysis is made with regard to sensor placement and sensor dimensions.

### 5.3.2. Model description

The spectral element method described in chapter 2 is used for this simulation. The mesh is structured in a two dimensional grid, given in fig. 5.6. A through-thickness plane is modelled, with the specimen thickness in y-direction (30 laminae of 0.18mm each) and the specimen length in x-direction (150mm). It is acknowledged elastic waves resulting from point emissions, such as in the case of pencil lead breaks, is a three-dimensional phenomenon[7]. When described by two-dimensional modelling plain strain conditions are assumed. Despite this incongruity, the insight gained with respect to sensor is considered representative for elastic wave emission simulations. As an excitation $F_{plb}$, a Hann-windowed four-period pulse with a centre frequency of 130kHz is applied at an outer vertical edge of the modelled composite plate. A timeframe of 100$\mu$s is simulated.

Material parameters may be found in table 5.3. Zero load initial condition is imposed[8]. No essential boundary conditions are applied. Damping is not included in the model[9].

Within this structure, the sensor is placed in the middle of the specimen length. The sensor is covered in 0.36mm of glass-epoxy material on the top and bottom sides and 2mm at the front and end sides. The sensor is modelled as a thin bar[10]. Voltages are obtained through averaging nodal strains over the piezoelectric sensor thickness, which are subsequently integrated over the electrode area. Note, at the high frequencies typical for elastic wave emissions, resistance effects can be neglected. This results in a simplified formulation of eq. (2.20), which is the same as formed by Gopalakrishnan (2011)[22].

| material | $E_1$ [$\times 10^9$N/m$^2$] | $E_3$ [$\times 10^9$N/m$^2$] | $\nu_{13}$ [-] | $\rho$ [kg/m$^3$] | sources |
|---|---|---|---|---|---|
| AS4/8552 | 141 | 10 | 0.3 | 1600 | [24] |
| glass/epoxy | 20 | 3.3 | 0.3 | 2010 | [25] |
| PZ27 | 66 | 59 | 0.37 | 7700 | |
| [50] | | | | | |

Table 5.3: Material parameters used in the analysis.

---

[7] Given the specimen geometry from the experiments, the emission would create a guided wave pattern both through-thickness and in planar direction.

[8] This is required given the explicit time integration.

[9] As given in section 4.3, electromechanical resonance is highly subject to mechanical damping. Thus, omitting damping is expected to result in noticeable resonant behaviour.

[10] Inherently, mechanical resonance, if present, is included in the structural modelling. Regarding the sensor (electrode) as a thin bar relates mechanical resonance to electromechanical resonance.

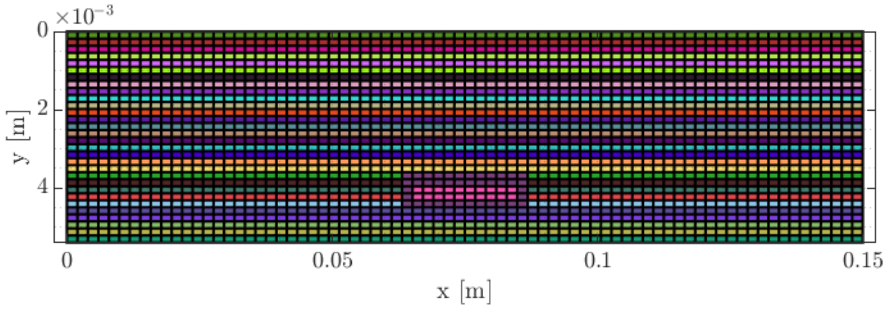

Figure 5.6: Discretisation of the composite plate through thickness. Colours indicate different material. Note the figure is not to scale for improved visibility.

### 5.3.3. Mesh convergence

To determine suitable element size and shape function order, a mesh convergence study is performed. A vertical ($y$-direction) excitation is applied. Element height $dy$ and corresponding bass function order $N_j$ are kept constant at 0.18mm (one ply thickness) and 1 respectively. Examined element sizes $dx$ were 0.5mm, 1mm and 2mm. Orders $N_i$ ranged from 1 to 10. For numerical stability of the Newmark explicit time integration, time steps are decreased accordingly from 10ns for $dx$ is 2mm and $N_j$ is low to 2.5ns for $dx$ is 0.5mm and $N_j$ is high. Due to computational constraints, not all combinations are assessed. The objective under evaluation is the sensor response voltage over time. The sensor response of the different meshes is compared by means of cross-correlation to the sensor response of one of the finest meshes, being $dx$ =1mm and $N_i$ =8. The result of the cross-correlation is a value from 0 for non-correlating data to 1 for identical data. A figure with results from the study is given in fig. 5.7. As it appears, both element size as well as shape function order contribute to convergence. From the figure, it is decided $dx$ =1mm and $N_i$ =4 is sufficient for future simulations.

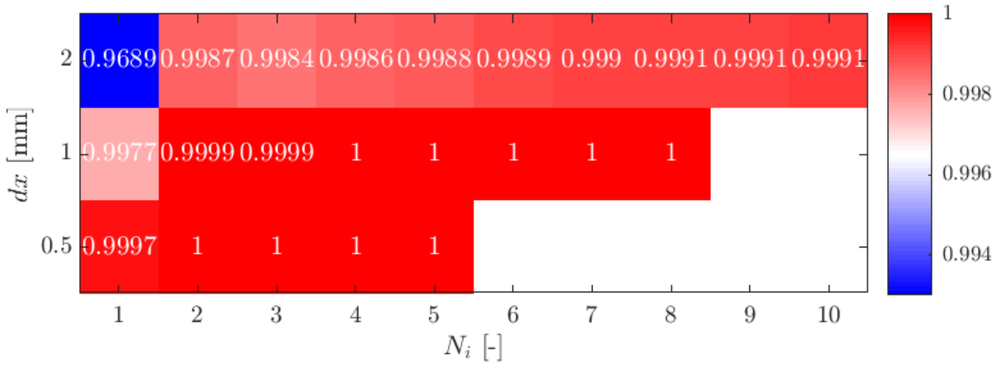

Figure 5.7: Convergence study with longitudinal element size $dx$ and shape function order $N_i$ as variables. The cross-correlation values are rounded to the fourth decimal.

### 5.3.4. Parametric study

As explained in section 2.4 in the frequency range of interest guided waves exist in two fundamental propagating mode types; symmetric $S$ and antisymmetric $A$ modes. From a damage characterization perspective it can be interesting to know to which extent the sensor can measure either mode [41]. To excite symmetric wave modes, the pulse described in section 5.3.3 is directed horizontally ($x$-direction, parallel to the laminae stack), whereas for antisymmetric wave modes, the pulse is directed vertically ($y$-direction, parallel to the thickness, perpendicular to the laminae stack). Sensor sensitivity to either mode type is dependent on sensor geometry and height location within the laminate. Therefore a parametric study is performed, varying piezoelectric sensor length $L_{PZT}$ and height location. Selected sensor lengths are 2mm, 10mm, 20mm, 40mm and 60mm. Height locations evaluated are at the first, the 6th, the 11th and the 16th lamina (from the outer layer to near the neutral axis of the laminate). Sensor responses are given in figs. 5.8 and 5.9 for the symmetric and antisymmetric modes respectively.

From the results in fig. 5.8 it can be seen that the reception of the symmetric guided wave is virtually independent on the sensor height location. Also, for sensor lengths $L_{PZT}$= 2mm, 10mm and 20mm, the response is similar, showing the incoming signal from 10$\mu$s to 35$\mu$s and its reflections[11] from 35$\mu$s to 60$\mu$s and 60$\mu$s to 85$\mu$s. At 130kHz, the wavelength of the fundamental symmetric mode equals around 13.8mm. Given the four-period burst and the reflections, the result is that for larger sensors, $L_{PZT}$= 40mm and 60mm, at the same time both incoming waves and reflections[12] are picked up b y the sensor. The result is a complicated signal. Note: according to Lizé et al. (2018)[41] sensor size should be smaller than half the wavelength of the excitation for an accurate signal.

The antisymmetric guided wave is governed by a bending motion[13] and as such, sensor height location is of importance. As the piezoelectric sensor approaches the neutral axis, output voltage diminishes. The antisymmetric guided wave has a relatively low propagation velocity and shows no reflections in the chosen timeframe. Increasing the sensor size results in a larger portion of the guided wave being covered at a certain time. During these times the voltage output decreases since the spatial integral[14] of the evaluated excitation strain decreases. Due to the lack of reflections, this effect is more clearly visible in antisymmetric excitations than in symmetric excitations.

To assess the sensitivity of the sensors on different frequency components of the excited signal, Fourier transformations are applied. Results are given in figs. 5.10 and 5.11. The smaller sensors (2mm, 10mm, 20mm) tend to capture the general characteristic of the antisymmetric guided wave. For the symmetric guided wave however, the smaller sensors show a trough at the centre frequency of 130kHz, whereas the excited signal shows a bulge. Possibly, this can be related to the size of the surrounding insulation, being 2mm in longitudinal direction and only 0.36mm in thickness direction. The larger sensors give larger deviations. This can be related to the phenomena described above. To investigate the effect of sensor electromechanic resonance on the sensor response, impedances based on one-dimensional axial vibration of the sensor are determined. The method is based on the work of Giurgiutiu (2007)[21]. Both a freely vibrating sensor and a constrained sensor are considered. The constrainment includes the geometry and stiffness of the glass-epoxy material compared to the geometry and stiffness of the piezoelectric material. Electromechanical resonance occurs where $|Z| \approx 0$. As can be seen in the plot, dimples and heights in the plots do not seem to distinctively relate to one-dimensional axial electromechanical resonances. However, it is visible the resonance effect for constrained $|Z_{con}|$ is notably smaller than in the free case, leading to the assumption that electromechanical resonance is of less significance in embedded piezoelectric sensors compared to freely vibrating counterparts.

### 5.3.5. Conclusion

Using a spectral element model with two-dimensional solid elements, a symmetric and an antisymmetric guided elastic wave travelling through a composite laminate with embedded piezoelectric sensor is simulated. Through post-processing sensor voltage output is retrieved. After a mesh convergence study, length of the sensor and and its height location in the composite is varied to examine their effect the sensor response. This is in line with research question:

> *How does the location and size of the sensor influence guided wave sensor responses?*

It is found the sensor response to symmetric guided waves is virtually independent from the sensors' height location in the simulation. In antisymmetric excitation, the height location strongly effects sensor output amplitude. Large sensors 40mm and 60mm do not accurately respresent the excited wave. For smaller sensors the response corresponds better to the excited signal. Antisymmetric guided waves are better captured than symmetric guided waves.

---

[11] The reflections are coming from the outer edge opposite to the excited edge, which are reflected as well by the former excited edge.

[12] Or two reflections.

[13] However, the antisymmetric mode is not exclusively a bending motion (chapter 2), hence small variations in shape between different height locations of sensors.

[14] Id est, the working principle of the piezoelectric sensor.

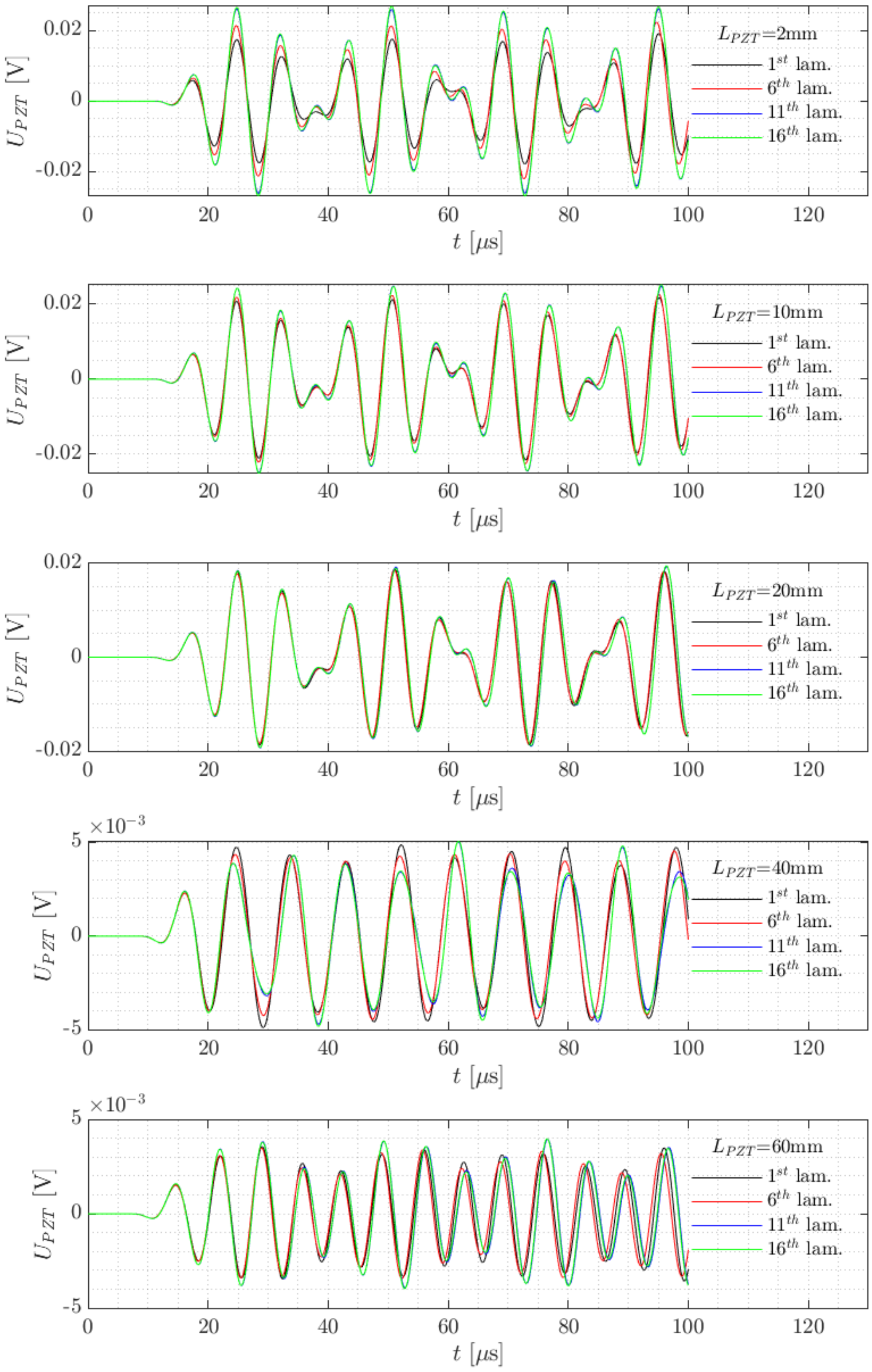

Figure 5.8: The response of a symmetric guided elastic wave for sensors with different lengths at different locations in the plate height.

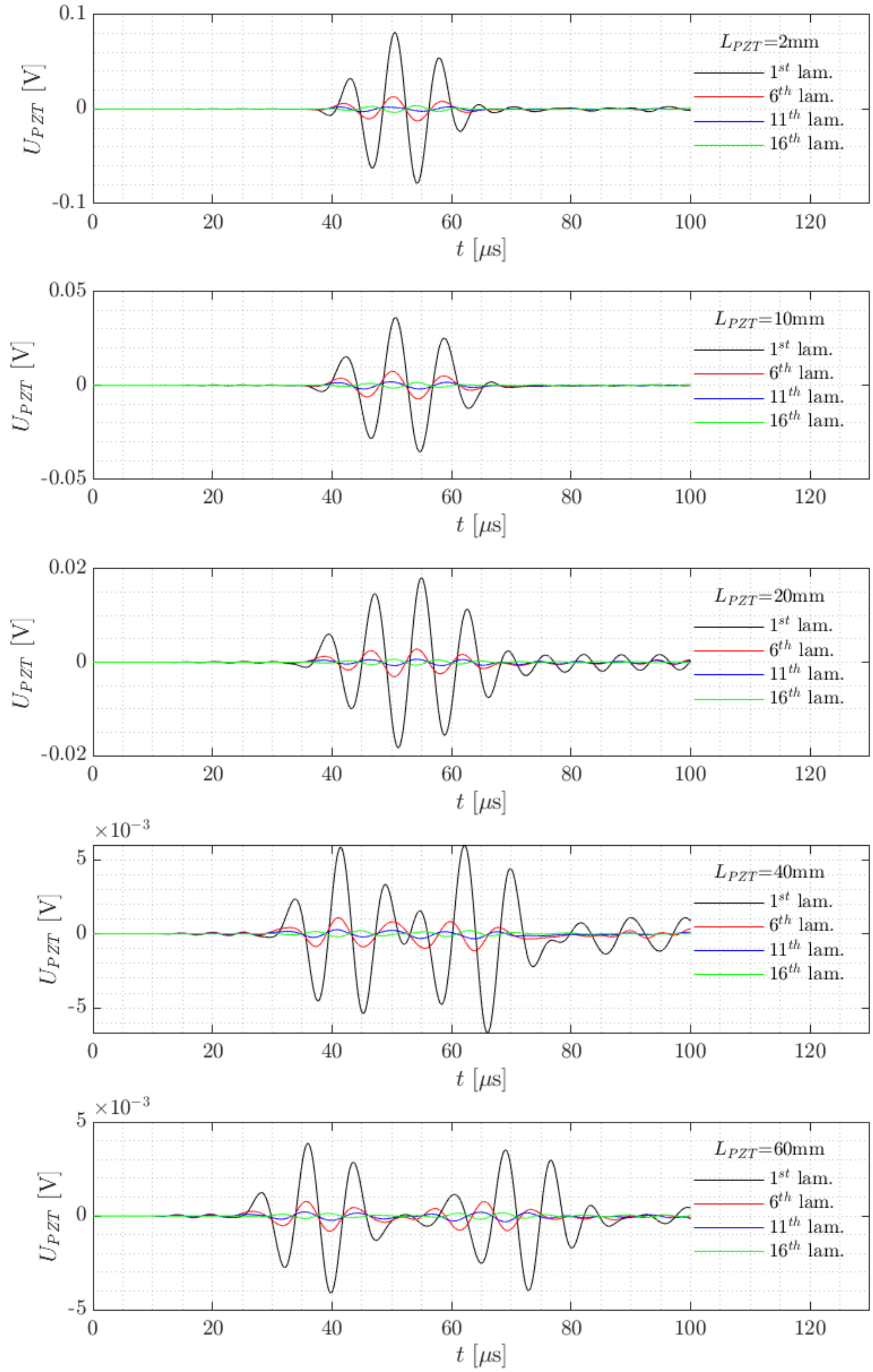

Figure 5.9: The response of an antisymmetric guided elastic wave for sensors with different lengths at different locations in the plate height.

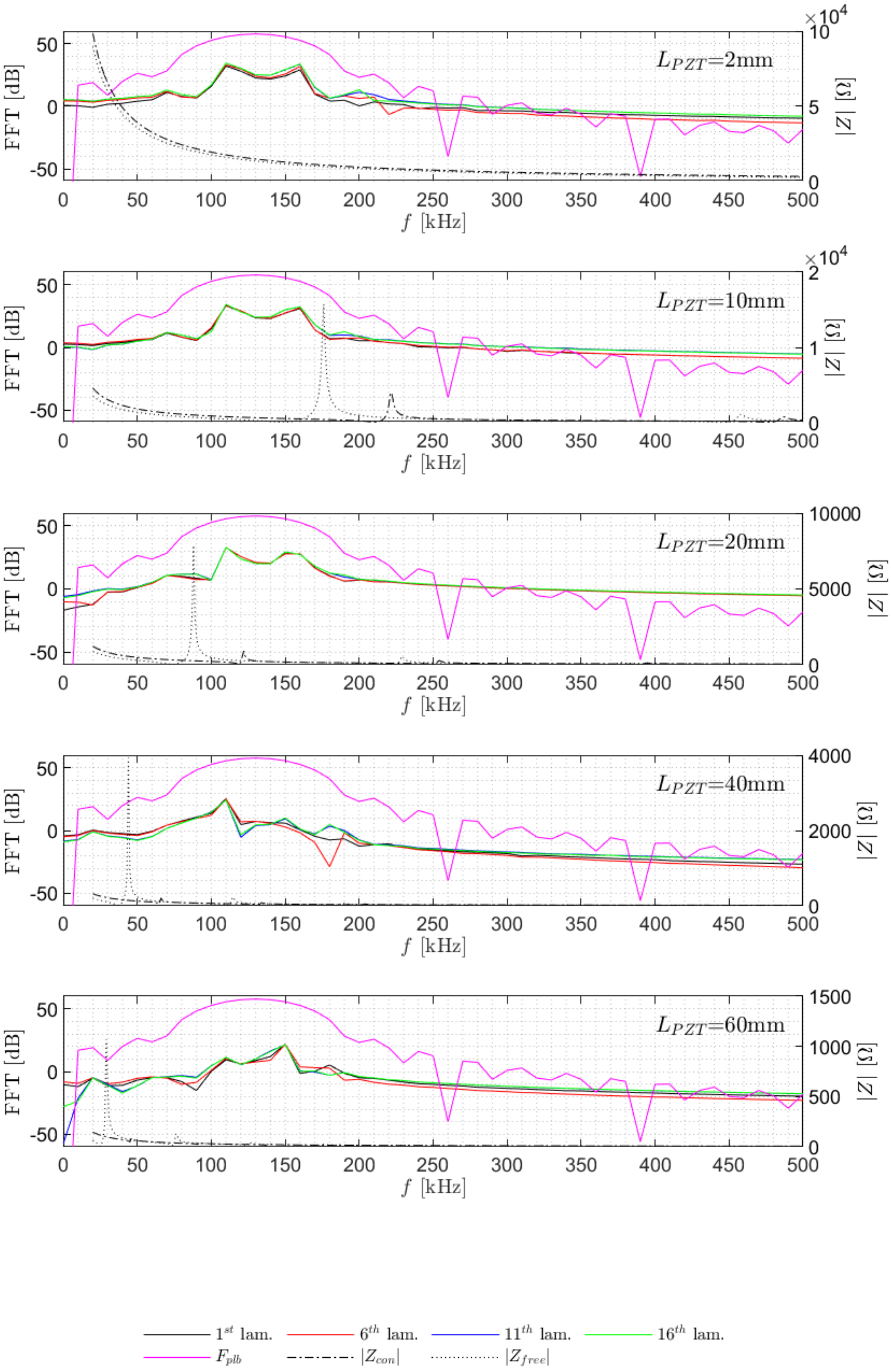

Figure 5.10: Fourier transform of the sensor response based on and overlaid with the Fourier transform of the excited symmetric guided elastic wave. The impedance is given for the a freely vibrating and constrained 1D sensor.

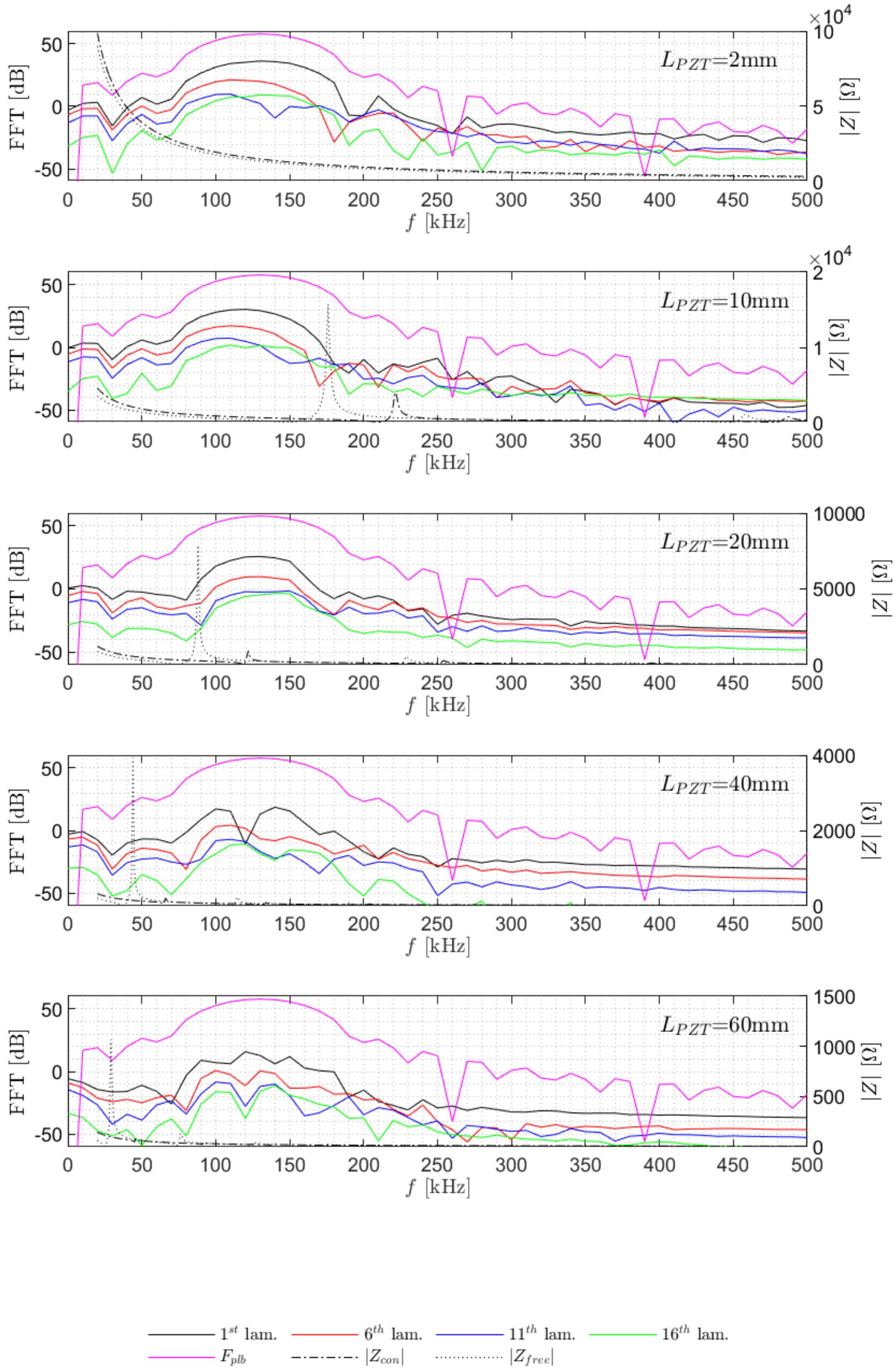

Figure 5.11: Fourier transform of the sensor response based on and overlaid with the Fourier transform of the excited antisymmetric guided elastic wave. The impedance is given for the a freely vibrating and constrained 1D sensor.

# 6
# Conclusion

To answer the research question:

> *Under what conditions is it feasible to measure loads and damage growth in composites using embedded piezoelectric sensors without compromising the structural performance?*

a summary is given on the conclusions with regard to the research subquestions.

## 6.1. Theoretical working principle

> *What are the governing physics of piezoelectricity and how can they be modelled in piezoelectric sensor applications?*

The piezoelectric effect is a small scale crystal deformation, altering electric polarity. This is captured in electromechanical constitutive equations. In piezoelectric sensor measurements, additional effects regarding parallel resistance and reactance are to be accounted for. Assuming one-way coupling, piezoelectric sensor response is retrieved by solving differential equation eq. (2.20).

> *What are elastic waves and how can they be modelled in composites for analysis of elastic wave emissions?*

Guided elastic waves are high-frequency elastic deformations that propagate across a plate due to the interaction with a boundary of the material. The phenomenon adheres to the theory of linear elasticity. For computational efficiency, a spectral element method is used in this thesis.

## 6.2. Sensor design and accuracy

*How can a piezoelectric sensor be embedded in a composite structure?*

> A design is presented in section 3.2.
>
> > *To what extent does the embedded piezoelectric sensor design survive the manufacturing process?*
>
> The piezoelectric sensors used in the design were able to survive the manufacturing process and record data. Out of 12 small sensors, 7 did record low-frequency cyclic bending. In the case of large sensors, this number is 3 out of 6. Nondestructive elastic wave emissions were detected by 9 out of 12 small sensors, and 3 out 6 large sensors.

*How does embedding a sensor affect its electromechanical resonant behaviour compared to a non-embedded sensor?*

> When the sensors were embedded, electromechanical resonant behaviour was observed at frequencies higher than for freely vibrating sensors. Also, the effect of resonance on the

electrical impedance of the sensor was strongly weakened as compared to freely vibrating sensors.

*What is the variation of responses between measurements and between piezoelectric sensors?*

In the conducted low-frequency bending experiments, the variation of responses between cycli is lower than 7%, 6% and 14% at $v_m$ = 1.8Hz, 0.18Hz and 0.018Hz for each sensor. Between different sensors the coefficient of variation turned out to be 25%, 21%, 42% for small sensors and 14%, 14%, 19% for large sensors. It is considered that by improving the embedding process these variations can be lowered.

*To what extent in terms of signal quality and maximum strain is the embedded piezoelectric sensor able to measure damage-related elastic wave emission?*

From sensor 3L, signals emitted by damage growth were obtained up to the point of failure, with a local compressive strain of $S_{CH}$ ≈8.45 to 9.45m$\varepsilon$. Signal quality is assessed by means of a signal-to-noise ratio, showing a median value of 17dB. This turned out to be sufficient for identifying damage-related emissions.

*Given the measurement set-up, what is the minimum frequency the piezoelectric sensor can measure strain accurately?*

The sensor captured loads having a frequency as low as $\approx 0.018$Hz. Below ≈1.8Hz, the result became distorted due to electrical discharge. Using a different set-up with higher impedance materials can lead to an improvement in this aspect.

*How does the location and size of the sensor influence elastic wave sensor responses?*

It is found the sensor response to symmetric guided waves is virtually independent from the sensors' height location in the simulation. In antisymmetric excitation, the height location strongly effects sensor output amplitude. Large sensors 40mm and 60mm do not accurately respresent the excited wave. For smaller sensors the response corresponds better to the excited signal. Antisymmetric guided waves are better captured than symmetric guided waves.

## 6.3. Host material mechanical properties

*To what extent are flexural mechanical properties of the composite host material influenced by embedding a piezoelectric sensor?*

In the monotonic bending experiment, the stiffness of specimens with sensors embedded turned out to be, depending on the method, on average 3 to 8 % lower than baseline specimens. In S specimens there was a noticeable decrease in maximum strain (8 to 21 %), load (5 %) and fracture toughness (34 %). This decrease is less pronounced or invisible for L specimens, being 0 to 10% in ultimate strain, 4% in ultimate load and 19% in toughness on average. In S (T) specimens, with the sensor on the tension side, ultimate strain compared to baseline N specimens had on average a drop less than 4%. Ultimate load and toughness on average had a maximum drop of 8%.

## 6.4. Comparison between experimental results and modelling

*How is the agreement between modelled and measured sensor responses?*

It has been shown that the performed modelling captures the effects related to sensor discharge at low frequencies. However modelled response amplitudes are 40% to 65% lower than measured response amplitudes for small (7mm diameter) and large sensors (20mm diameter) respectively.

# 7

# Recommendations

The following recommendations for future research are made with respect to the experimental data gathered, modelling and future applications.

## 7.1. Experiment data

The nondestructive elastic wave emission tests were performed at different distances from the sensor. Differences in results might be used to determine damping parameters that are usable for modelling and material characterisation. Also the effect of dispersion can be quantified.

During the mechanical failure of the specimens, for each specimen two commercial guided wave sensors were attached and recording. The data from these recordings can allow localisation of occurring damage events. This could then be linked to the effect on structural integrity of embedding a sensor in the composite laminate.

Also, redoing or continuing failure tests can be fruitful, since in this thesis only two or four per type are tested.

## 7.2. Modelling

In the report, only one-way coupling, from strain to voltage, is modelled. It would be appropriate to quantify the effect of two-way coupling. Coupled field finite element models like those that are being developed by the research group at the moment could provide this two-way coupling.

In the modelling of elastic wave emissions and the subsequent guided wave, a two-dimensional model is used. Also the sensor was considered uniform across the third dimension. In many situations, however, elastic waves follow a three-dimensional pattern, which would be reflected in the sensor response. Three-dimensional modelling[1] could then be accurately compared to the measurement data of appendix A.

Once such modelling method would be sufficiently validated, it could be adapted to perform inverse analysis, for example for a direct translation from sensor voltage to a certain load distribution.

## 7.3. Application

Fundamental and practical insight is gained in the development of embedded sensor design. This could be helpful in developing more elaborate structures with embedded sensors and for a wider range of applications such as hydrodynamic load measurements.

---

[1] In combination with an appropriate mapping matrix.

# 8

# Acknowledgement

This thesis has been sponsored by Defensie Materieel Organisatie (DMO). For this I am grateful towards Andre Vaders.

# Bibliography

[1] Ewoud Aaij. Lamb wave propagation in sandwich composite structures for the detection of impact damage. 2016.

[2] Hafiz Qasim Ali, Isa Emami Tabrizi, Raja Muhammad Awais Khan, Ali Tufani, and Mehmet Yildiz. Microscopic analysis of failure in woven carbon fabric laminates coupled with digital image correlation and acoustic emission. *Composite Structures*, 230:111515, 2019. ISSN 0263-8223. doi: https://doi.org/10.1016/j.compstruct.2019.111515. URL `http://www.sciencedirect.com/science/article/pii/S0263822319323414`.

[3] C. Andreades, P. Mahmoodi, and F. Ciampa. Characterisation of smart cfrp composites with embedded pzt transducers for nonlinear ultrasonic applications. *Composite Structures*, 206: 456–466, 2018. doi: 10.1016/j.compstruct.2018.08.083. URL `https://www.scopus.com/inward/record.uri?eid=2-s2.0-85052663801&doi=10.1016%2fj.compstruct.2018.08.083&partnerID=40&md5=71cdf14da3821bffb5ac166e50741bf1`.

[4] A ASTM. standard guide for determining the reproducability of acoustic emission sensor responce, 1994. In *American society for testing and materials*.

[5] Arthur Ballato. Equivalent circuits for resonators and transducers driven piezoelectrically. Report, US army laboratory command, 1990.

[6] Shaoluo Butler, Mark Gurvich, Anindya Ghoshal, Gregory Welsh, Paul Attridge, Howard Winston, Michael Urban, and Nathaniel Bordick. Effect of embedded sensors on interlaminar damage in composite structures. *Journal of Intelligent Material Systems and Structures*, 22(16):1857–1868, August 2011. doi: 10.1177/1045389x11414225. URL `https://doi.org/10.1177/1045389x11414225`.

[7] James S Chilles, Anthony Croxford, and Ian P Bond. Design of an embedded sensor, for improved structural performance. *Smart Materials and Structures*, 24(11):115014, October 2015. doi: 10.1088/0964-1726/24/11/115014. URL `https://doi.org/10.1088/0964-1726/24/11/115014`.

[8] Klas Levin Christophe A. Paget. Structural integrity of composites with embedded piezoelectric ceramic transducers, 1999. URL `https://doi.org/10.1117/12.350710`.

[9] Wikimedia Commons. File:gudin théodore - trait de dévouement du capitaine desse, de bordeaux, envers le colombus, navire hollandais.jpg — wikimedia commons, the free media repository, 2019. URL `https://commons.wikimedia.org/w/index.php?title=File:Gudin_Th%C3%A9odore_-_Trait_de_d%C3%A9vouement_du_capitaine_Desse,_de_Bordeaux,_envers_Le_Colombus,_navire_hollandais.jpg&oldid=342907790`. [Online; accessed 30-October-2019].

[10] ASTM D6272−17. Standard test method for flexural properties of unreinforced and reinforced plastics and electrical insulating materials by four-point bending. Technical report, ASTM, 2017. URL `https://compass.astm.org/download/D6272.22166.pdf`.

[11] R.S. Dahiya and M. Valle. *Robotic Tactile Sensing: Technologies and System*. Springer Netherlands, 2012. ISBN 9789400705791. URL `https://books.google.nl/books?id=V7NJSe7bvL0C`.

[12] F.M. Dekking, C. Kraaikamp, H.P. Lopuhaä, and L.E. Meester. *A Modern Introduction to Probability and Statistics: Understanding Why and How (Springer Texts in Statistics)*. Springer, 2007. ISBN 1852338962.

[13] DuPont. Dupont kapton summary of properties, 2017. URL `https://www.dupont.com/content/dam/dupont/products-and-services/membranes-and-films/polyimde-films/documents/DEC-Kapton-summary-of-properties.pdf`.

[14] M. Dziendzikowski, A. Kurnyta, K. Dragan, S. Klysz, and A. Leski. In situ barely visible impact damage detection and localization for composite structures using surface mounted and embedded pzt transducers: A comparative study. *Mechanical Systems and Signal Processing*, 78:91–106, 2016. doi: 10.1016/j.ymssp.2015.09.021. URL `https://www.scopus.com/inward/record.uri?eid=2-s2.0-84948798947&doi=10.1016%2fj.ymssp.2015.09.021&partnerID=40&md5=e9acf3c371bd3fa1e14641d9bd2be595`.

[15] J. Erhart, P. Pulpan, and M. Pustka. *Piezoelectric Ceramic Resonators*. Springer International Publishing, 2016. ISBN 9783319424811. URL `https://books.google.nl/books?id=6v1RDQAAQBAJ`.

[16] A. Erturk and D.J. Inman. *Piezoelectric Energy Harvesting*. Wiley, 2011. ISBN 9781119991359. URL `https://books.google.nl/books?id=mHaHzh_B8oQC`.

[17] Farnell. Solderable enamelled copper wire38swg, 0.15mm, 2015. URL `http://www.farnell.com/datasheets/1957992.pdf`.

[18] Gallagher Corp. Electrical polyurethane properties, 2017. URL `https://gallaghercorp.com/wp-content/uploads/2016/08/WP-116-ELECTRICAL-POLYURETHANE-PROPERTIES.1.pdf`.

[19] G. Gautschi. *Piezoelectric Sensorics: Force Strain Pressure Acceleration and Acoustic Emission Sensors Materials and Amplifiers*. Springer Berlin Heidelberg, 2006. ISBN 9783540422594. URL `https://books.google.nl/books?id=-nYFSLcmc-cC`.

[20] Mehrdad N. Ghasemi-Nejhad, Richard Russ, and Saeid Pourjalali. Manufacturing and testing of active composite panels with embedded piezoelectric sensors and actuators. *Journal of Intelligent Material Systems and Structures*, 16(4):319–333, April 2005. doi: 10.1177/1045389x05050103. URL `https://doi.org/10.1177/1045389x05050103`.

[21] V. Giurgiutiu. *Structural Health Monitoring with Piezoelectric Wafer Active Sensors*. Academic Press, 2008. ISBN 9780120887606. URL `https://books.google.nl/books?id=CdPcXwAACAAJ`.

[22] Srinivasan Gopalakrishnan, Massimo Ruzzene, and Sathyanarayana Hanagud. Fundamentals concepts in elasticity, mechanics and wave propagation. In *Springer Series in Reliability Engineering*, pages 41–95. Springer London, 2011. doi: 10.1007/978-0-85729-284-1_2. URL `https://doi.org/10.1007/978-0-85729-284-1_2`.

[23] Sung-Kyu Ha, Charles Keilers, and Fu-Kuo Chang. Analysis of laminated composites containing distributed piezoelectric ceramics. *Journal of intelligent material systems and structures*, 2(1): 59–71, 1991.

[24] Hexcel corporation. Hexply 8552 epoxy matrix (180°c/356°f curing matrix), 2016. URL `https://www.hexcel.com/user_area/content_media/raw/HexPly_8552_eu_DataSheet.pdf`.

[25] Huntsman. Araldite ly 5052 / aradur 5052 cold curing epoxy systems, 2012. URL `https://samaro.fr/pdf/FT/Araldite_FT_LY_5052_Aradur_5052_EN.pdf`.

[26] American National Standards Institute, Ferroelectrics IEEE Ultrasonics, Frequency Control Society. Standards Committee, Institute of Electrical, and Electronics Engineers. *An American National Standard: IEEE Standard on Piezoelectricity Standard*. IEEE, 1988. URL `https://books.google.co.uk/books?id=YCs5nQEACAAJ`.

[27] Mary Lou Jay. Ship Propeller Shows Promise, January 2019. URL `http://compositesmanufacturingmagazine.com/2019/01/ship-propeller-shows-promise/`.

[28] Diethelm Johannsmann. Studies of viscoelasticity with the qcm. *Springer Series on Chemical Sensors and Biosensors*, 5, 2007.

[29] E. Kirkby, R. de Oliveira, V. Michaud, and J. A. Månson. Impact localisation with fbg for a self-healing carbon fibre composite structure. *Composite Structures*, 94(1):8–14, 2011. doi: 10.1016/j.compstruct.2011.07.030. URL `https://www.scopus.com/inward/record.uri?eid=2-s2.0-80053051906&doi=10.1016%2fj.compstruct.2011.07.030&partnerID=40&md5=e709ef98abc93a3cb00671b1b907e956`.

[30] Dimitri Komatitsch and Jeroen Tromp. Introduction to the spectral element method for three-dimensional seismic wave propagation. *Geophysical journal international*, 139(3):806–822, 1999.

[31] Hari P Konka, M A Wahab, and K Lian. The effects of embedded piezoelectric fiber composite sensors on the structural integrity of glass-fiber–epoxy composite laminate. *Smart Materials and Structures*, 21(1):015016, December 2011. doi: 10.1088/0964-1726/21/1/015016. URL `https://doi.org/10.1088/0964-1726/21/1/015016`.

[32] *Kyowa Strain Gages KFGS-5-120-C1-11*. Kyowa electronic instruments Co.,LTD, 2014.

[33] K. Y. Lam, X. Q. Peng, G. R. Liu, and J. N. Reddy. A finite-element model for piezoelectric composite laminates. *Smart Materials and Structures*, 6(5):583–591, 1997. doi: 10.1088/0964-1726/6/5/009. URL `https://www.scopus.com/inward/record.uri?eid=2-s2.0-0031245171&doi=10.1088%2f0964-1726%2f6%2f5%2f009&partnerID=40&md5=815ac1a8b93a90fb197e512a13758358`.

[34] L. Lampani, F. Sarasini, J. Tirillò, and P. Gaudenzi. Analysis of damage in composite laminates with embedded piezoelectric patches subjected to bending action. *Composite Structures*, 202: 935–942, 2018. doi: 10.1016/j.compstruct.2018.04.073. URL `https://www.scopus.com/inward/record.uri?eid=2-s2.0-85047079569&doi=10.1016%2fj.compstruct.2018.04.073&partnerID=40&md5=c5670f91253c274d6b6259ea4a3eb0a3`.

[35] Luca Lampani and Paolo Gaudenzi. Innovative composite material component with embedded self-powered wireless sensor device for structural monitoring. *Composite Structures*, 202:136–141, October 2018. doi: 10.1016/j.compstruct.2018.01.011. URL `https://doi.org/10.1016/j.compstruct.2018.01.011`.

[36] Cara A.C. Leckey, Kevin R. Wheeler, Vasyl N. Hafiychuk, Halyna Hafiychuk, and Doğan A. Timuçin. Simulation of guided-wave ultrasound propagation in composite laminates: Benchmark comparisons of numerical codes and experiment. *Ultrasonics*, 84:187–200, March 2018. doi: 10.1016/j.ultras.2017.11.002. URL `https://doi.org/10.1016/j.ultras.2017.11.002`.

[37] Brian Michael Lempriere. *Ultrasound and Elastic Waves: Frequently Asked Questions*. Academic Press, may 2002. ISBN 9780124433458. URL `https://www.xarg.org/ref/a/0124433456/`.

[38] C.K. Liew and M. Veidt. Review of integrated piezoceramic transducers in smart materials and structures. *Piezoelectric Materials: Structure, Properties and Applications*, pages 109–132, 01 2010.

[39] B. Lin and V. Giurgiutiu. Modeling and testing of pzt and pvdf piezoelectric wafer active sensors. *Smart Materials and Structures*, 15(4):1085–1093, 2006. doi: 10.1088/0964-1726/15/4/022. URL `https://www.scopus.com/inward/record.uri?eid=2-s2.0-33746310584&doi=10.1088%2f0964-1726%2f15%2f4%2f022&partnerID=40&md5=c1b7b45ec39c603f9527553327838d6f`.

[40] M. Lin and F.-K. Chang. The manufacture of composite structures with a built-in network of piezoceramics. *Composites Science and Technology*, 62(7-8):919–939, 2002. doi: 10.1016/S0266-3538(02)00007-6. URL `https://www.scopus.com/inward/record.uri?eid=2-s2.0-0036601788&doi=10.1016%2fS0266-3538%2802%2900007-6&partnerID=40&md5=5c8fd200ff9084fe7fff967138dade98`. cited By 155.

[41] Emmanuel Lizé, Marc Rébillat, Nazih MECHBAL, and Christian BOLZMACHER. Dual pzt sizing for mode decomposition on an anisotropic composite plate. In *9th European Workshop on Structural Health Monitoring, EWSHM*, volume 225, 2016.

[42] P.J. Maljaars. *Hydro-elastic analysis of flexible marine propellers*. PhD thesis, 2019. URL `http://resolver.tudelft.nl/uuid:19c9610b-9a72-42a6-8340-2ba01ec78cc6`.

[43] S. Mall. Integrity of graphite/epoxy laminate embedded with piezoelectric sensor/actuator under monotonic and fatigue loads. *Smart Materials and Structures*, 11(4):527–533, 2002. doi: 10.1088/0964-1726/11/4/307. URL `https://www.scopus.com/inward/record.uri?eid=2-s2.0-0036671066&doi=10.1088%2f0964-1726%2f11%2f4%2f307&partnerID=40&md5=13f3d267d67a23904241e52c4f806060`. cited By 49.

[44] S. Mall and J.M. Coleman. Monotonic and fatigue loading behavior of quasi-isotropic graphite/epoxy laminate embedded with piezoelectric sensor. *Smart Materials and Structures*, 7(6):822–832, 1998. doi: 10.1088/0964-1726/7/6/010. URL `https://www.scopus.com/inward/record.uri?eid=2-s2.0-0032307860&doi=10.1088%2f0964-1726%2f7%2f6%2f010&partnerID=40&md5=6fdcf676f0d4d81769360bebaef1aa70`. cited By 73.

[45] S. Mall, S.B. Dosedel, and M.W. Holl. The performance of graphite-epoxy composite with embedded optical fibers under compression. *Smart Materials and Structures*, 5(2):209–215, 1996. doi: 10.1088/0964-1726/5/2/009. URL `https://www2.scopus.com/inward/record.uri?eid=2-s2.0-0030121706&doi=10.1088%2f0964-1726%2f5%2f2%2f009&partnerID=40&md5=dd649ae48ddc3a1ccaf023fd3e1e1497`. cited By 26.

[46] S. Masmoudi, A. El Mahi, and S. Turki. Fatigue behaviour and structural health monitoring by acoustic emission of e-glass/epoxy laminates with piezoelectric implant. *Applied Acoustics*, 108:50–58, 2016. doi: 10.1016/j.apacoust.2015.10.024. URL `https://www.scopus.com/inward/record.uri?eid=2-s2.0-84949495738&doi=10.1016%2fj.apacoust.2015.10.024&partnerID=40&md5=2d1f0faab8f22116ebec749eb3678850`.

[47] Sahir Masmoudi, Abderrahim El Mahi, Said TURKI, and Rachid El Guerjouma. Structural Health Monitoring of Smart Composite Material by Acoustic Emission. In Société Française d'Acoustique, editor, *Acoustics 2012*, Nantes, France, April 2012. URL `https://hal.archives-ouvertes.fr/hal-00810878`.

[48] W.P. Mason. *Electromechanical transducers and wave filters*. Bell Telephone Laboratories series. D. Van Nostrand Co., 1948. URL `https://books.google.nl/books?id=eKBRAAAAMAAJ`.

[49] MathWorks. snr signal-to-noise ratio. `https://nl.mathworks.com/help/signal/ref/snr.html#bt2g_cb-2`. Accessed: 2019-09-30.

[50] Meggit. *Data for modelling*, 2017. URL `https://www.meggittferroperm.com/resources/data-for-modelling/`.

[51] Meggit, 2019,Electronic correspondence with Karl Elkjaer.

[52] S.O.R. Moheimani and A.J. Fleming. *Piezoelectric Transducers for Vibration Control and Damping*. Springer London, 2006. ISBN 9781846283321. URL `https://books.google.nl/books?id=ZR9KAAAAQBAJ`.

[53] National Instruments. 2014. URL `http://www.ni.com/pdf/manuals/374371a.pdf`.

[54] National Instruments. *DEVICE SPECIFICATIONS NI 6229*, 2016. URL `http://www.ni.com/pdf/manuals/375204c.pdf`.

[55] A.H. Nayfeh. *Wave Propagation in Layered Anisotropic Media: with Application to Composites*. North-Holland Series in Applied Mathematics and Mechanics. Elsevier Science, 1995. ISBN 9780080543734. URL `https://books.google.nl/books?id=iHfQjWR3QzAC`.

[56] Noliac. The mason model, definition and identification of the dynamic parameters, 2019. URL http://www.noliac.com/tutorials/dynamic-actuators/the-mason-model-definition-and-identification-of-the-dynamic-parameters/.

[57] Pedro Ochoa, Roger M. Groves, and Rinze Benedictus. Systematic multiparameter design methodology for an ultrasonic health monitoring system for full-scale composite aircraft primary structures. *Structural Control and Health Monitoring*, 26(5):e2340, 2019. doi: 10.1002/stc.2340. URL https://onlinelibrary.wiley.com/doi/abs/10.1002/stc.2340. e2340 STC-18-0310.R1.

[58] Daniel L. Osmont, Marc Dupont, Remi Gouyon, Michel B. Lemistre, and Daniel L. Balageas. Piezoelectric transducer network for dual-mode (active/passive) detection, localization, and evaluation of impact damages in carbon/epoxy composite plates. In Pierre F. Gobin and Clifford M. Friend, editors, *Fifth European Conference on Smart Structures and Materials*. SPIE, August 2000. doi: 10.1117/12.396391. URL https://doi.org/10.1117/12.396391.

[59] C. A. Paget and K. Levin. Structural integrity of composites with embedded piezoelectric ceramic transducer. *Proceedings of SPIE - The International Society for Optical Engineering*, 3668(I):306–313, 1999. URL https://www.scopus.com/inward/record.uri?eid=2-s2.0-0032633773&partnerID=40&md5=c56370a90f152f5f2615bc1dbc151ff2.

[60] L Pahlavan. Wave propagation in thin-walled composite structures: Application to structural health monitoring, 2012.

[61] *User manual PICAS*. PEEKEL INSTRUMENTS B.V, INDUSTRIEWEG 161, ROTTERDAM.

[62] Prospector. Polyurethane (pur) typical properties generic pur, unspecified.

[63] Xinlin P. Qing, Shawn J. Beard, Amrita Kumar, Teng K. Ooi, and Fu-Kuo Chang. Built-in sensor network for structural health monitoring of composite structure. *Journal of Intelligent Material Systems and Structures*, 18(1):39–49, October 2006. doi: 10.1177/1045389x06064353. URL https://doi.org/10.1177/1045389x06064353.

[64] JN Reddy. On laminated composite plates with integrated sensors and actuators. *Engineering Structures*, 21(7):568–593, 1999.

[65] Erling Ringgaard. The metal-ceramic interface in multilayer piezoceramic components, 1999.

[66] S.J. Rupitsch. *Piezoelectric Sensors and Actuators: Fundamentals and Applications*. Springer Berlin Heidelberg, 2018. ISBN 9783662575345. URL https://books.google.nl/books?id=2JdmDwAAQBAJ.

[67] Giuseppe Sala, M Olivier, Paolo Bettini, and D Sciacovelli. Embedded piezoelectric sensors and actuators for control of active composite structures. *Mechanical and Thermal Engineering Department, Carlo Gavazzi Space ESTEC, European Space Agency*, 2004.

[68] R. Schulze, P. Streit, T. Fischer, A. Tsapkolenko, M. Heinrich, M. Sborikas, L. Kroll, T. Gessner, and M. Wegener. Fiber-reinforced composite structures with embedded piezoelectric sensors. In *Proceedings of IEEE Sensors*, volume 2014-December, pages 1563–1566. doi: 10.1109/ICSENS.2014.6985315. URL https://www.scopus.com/inward/record.uri?eid=2-s2.0-84931057225&doi=10.1109%2fICSENS.2014.6985315&partnerID=40&md5=6c4b01c46207229a12ad5059a83169a9.

[69] S. Shin, B. Zamorano, and N. Elvin. Comparison of the electromechanical properties of embedded and surface-mounted piezoelectric transducers. *Journal of Intelligent Material Systems and Structures*, 27(20):2837–2850, 2016. doi: 10.1177/1045389X16642299. URL https://www.scopus.com/inward/record.uri?eid=2-s2.0-85002498876&doi=10.%2f1045389X16642299&partnerID=40&md5=2475c71ff1bad568465ab5f0b99df840.

[70] D.R. Shukla and A.J. Vizzini. Interlacing for improved performance of laminates with embedded devices. *Smart Materials and Structures*, 5(2):225–229, 1996. doi: 10.1088/0964-1726/5/2/011. URL `https://www.scopus.com/inward/record.uri?eid=2-s2.0-0030125472&doi=10.1088%2f0964-1726%2f5%2f2%2f011&partnerID=40&md5=7dc3cf26c6dd80c14ab190e35f695a12`. cited By 29.

[71] Hong-Yue Tang, Charles Winkelmann, Wahyu Lestari, and Valeria La Saponara. Composite structural health monitoring through use of embedded PZT sensors. *Journal of Intelligent Material Systems and Structures*, 22(8):739–755, May 2011. doi: 10.1177/1045389x11406303. URL `https://doi.org/10.1177/1045389x11406303`.

[72] Vallen Systeme. *AE–Preamplifier Data Sheet*. URL `http://www.vallen.de/fileadmin/user_upload/Datasheet_AEP5_1602.pdf`.

[73] K. S. Van Dyke. The piezo-electric resonator and its equivalent network. *New York Institute*, 1928.

[74] Bin Yang, Fu-Zhen Xuan, Pengcheng Jin, Chaojie Hu, Biao Xiao, Dan Li, Yanxun Xiang, and Hongshuai Lei. Damage localization in composite laminates by building in PZT wafer transducers: A comparative study with surface-bonded PZT strategy. *Advanced Engineering Materials*, 21(3): 1801040, December 2018. doi: 10.1002/adem.201801040. URL `https://doi.org/10.1002/adem.201801040`.

[75] Warren C. Young, Richard G Budynas, and Ali M. Sadegh. *Roark's Formulas for Stress and Strain, 8th Edition*. McGraw-Hill Education, 2011. ISBN 0071742476. URL `https://www.amazon.com/Roarks-Formulas-Stress-Strain-8th/dp/0071742476?SubscriptionId=AKIAIOBINVZYXZQZ2U3A&tag=chimbori05-20&linkCode=xm2&camp=2025&creative=165953&creativeASIN=0071742476`.

[76] B. Zamorano-Senderos and N. Elvin. High-speed impact location detection on anisotropic composite panels using embedded piezoelectric sensors. *Journal of Intelligent Material Systems and Structures*, 25(15):1921–1936, 2014. doi: 10.1177/1045389X13512188. URL `https://www.scopus.com/inward/record.uri?eid=2-s2.0-84907224563&doi=10.1177%2f1045389X13512188&partnerID=40&md5=831757ec7313ae98b8507e3ab8471cbb`. cited By 6.

# A

# Nondestructive elastic wave emissions

As described per section 3.3, results are given for the first phase measurements with the full uncut plates. Second phase results are not discussed. The results accompany section 4.2 and as such, the results serve as illustration of the elastic wave emissions captured. For sensor 3L, a response $U_{PZT}$ to pencil lead breaks at given distances is shown in fig. A.1. The signal is corrected for the 40dB preamplifier. From the figure it becomes clear the response varies over excitation distance as well as that there are only slight differences per pencil lead break.

To examine how different piezoelectric sensors vary in their ability to capture guided waves, a so-called B-scan is given in fig. A.2. Here the responses, like those in fig. A.1, are set side by side. This figure shows that variation of pencil lead breaks for a single sensor is smaller than variation over sensors. In the case of sensor 8S, the overall amplitude is lower. Note, some sensors show flipped polarity due to inconsistent wiring, as can be seen when comparing responses of 9S with 11S and 12S and 3L compared to 2L and 5L.

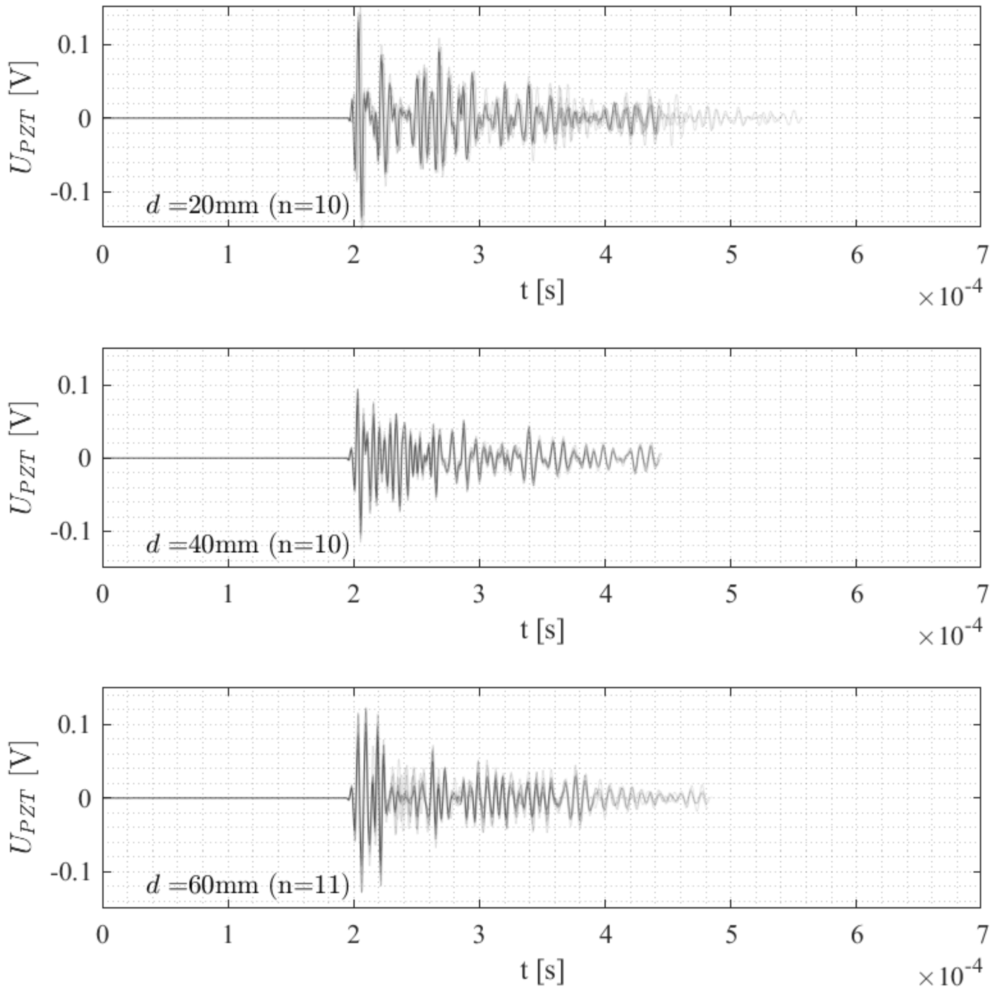

Figure A.1: Response $U_{PZT}$ of pencil breaks at distance $d$ over time of sensor 3L. $n$ denotes the number of pencil breaks in the plot. The lines have been made semi-transparent, to enhance visibility of overlapping responses.

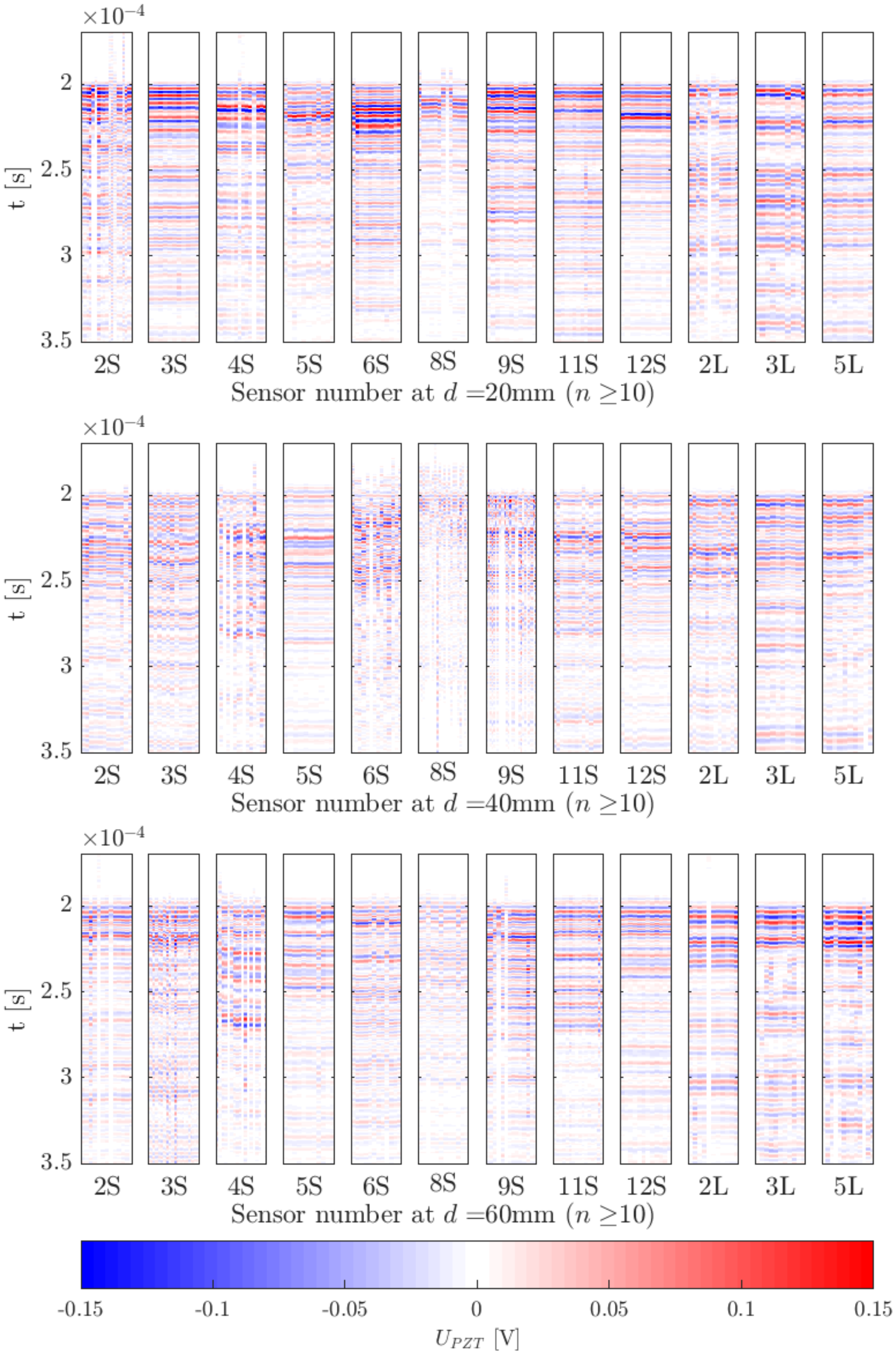

Figure A.2: B-scan visualisation of $U_{PZT}$ at distance $d$ over time. $n$ denotes the number of pencil breaks in the plot.